THE HONG KONG POLYTECHNIC UNIVERSITY

THE DEPARTMENT OF APPLIED PHYSICS

FABRICATION AND CHARACTERIZATION OF ALL OXIDE P-N JUNCTION DIODES

ZHUANG LIN

A THESIS SUBMITTED IN PARTIAL FULFILMENT
OF THE REQUIREMENTS FOR THE DEGREE OF
DOCTOR OF PHILOSOPHY

AUGUST 2006

CERTIFICATE OF ORIGINALITY

I hereby declare that this thesis is my own work and that, to the best of my knowledge and belief, it reproduces no material previously published or written nor material which has been accepted for the award of any other degree or diploma, except where due acknowledgement has been made in the text.

______________________________(Signed)

_________ZHUANG LIN_________(Name of student)

ABSTRACT

We have grown ZnO and MgO mixed oxide thin films by pulsed laser deposition. Most other similar work reported in the open literature so far involved preparing wurtzite structured $Mg_xZn_{1-x}O$ (w-MZO) films on sapphire substrates with $x<0.4$. We argue that the cubic form of ZnO, including cubic $Mg_xZn_{1-x}O$ (c-MZO) could be useful as transparent conducting oxide (TCO), n-type or p-type doped semiconducting oxide, wide bandgap UV detector and dilute magnetic semiconductor (DMS) that can be matched with and grown on many other cubic oxides and perovskites to form interesting devices. By the use of single crystal substrate of matched cubic structures, such as MgO and $LaAlO_3$ (LAO), we have demonstrated that cubic $Mg_xZn_{1-x}O$ thin films even with $x=0.57$, representing maximum reported solubility of Zn in MgO, can be stabilized under normal ambient. High quality homoepitaxially and heteroepitaxially grown c-MZO films on MgO and LAO respectively have also been obtained.

MZO is a wide bandgap material. Its absorption band edge shifts deep into UV with increased MgO content. Indium doped c-MZO (In-MZO) thin films show typical n-type semiconducting properties. Electrical conductivity at room temperature as high as 10^2 S cm^{-1} has been achieved for samples with In 8 at.% doping. Yet they remain optically transparent over the whole visible spectrum. Thus they become desirable n-type TCO.

Li-doped NiO ($Li_{0.15}Ni_{0.85}O$, LNO), on the other hand, is a p-type conductor with good optical transmittance. We have fabricated a number of optical transparent all-oxide p-n junctions based on p-LNO/n-Nb doped SrTiO3 single crystal substrate, p-LNO/n-ZnO(wurtzite) and p-LNO/n-In-MZO. Their structural qualities have been studied and excellent heteroepitaxial relationships have been demonstrated.

The results of our present investigation provide affirmative evidence for using all-oxide to develop p-n diode junction devices. In particular the advantages of utilizing the diversified properties of oxide such as wide bandgap, good visible/UV transmittance, potential DMS and stability at high temperature can be realized in these junction diodes. We have also illustrated that c-MZO is a very good base material for fabricating all-oxide p-n junction diodes.

ACKNOWLEDGEMENTS

I would like to express my appreciation to my supervisor Dr. K. H. Wong for his guidance, continuous support and encouragement in the whole period of my study. He provide clear research direction and experimental and characterization techniques throughout. I am also impressed by his personality as well as the attitude toward research works.

I also give my appreciation for the help and assistance from the colleagues in our group, namely Mr. W. L. Sin, Ms. C. Y. Lam and Mr. C. H. Lau.

I would like to thank Dr. G. K. H. Pang for his invaluable assistance and comments on the TEM characterization.

I would also like to thank all the members of my family, my teachers and my friends, whose support, encouragement and understanding are invaluable.

I gratefully acknowledge the financial support from the Research Grants Council (RGC) of the Hong Kong Special Administrative Region (code PolyU 5294/02 P) and technical support provided by Materials Research Centre (MRC) of the Hong Kong Polytechnic University. I am grateful for the award of a research studentship by the Hong Kong Polytechnic University.

LIST OF FIGURE CAPTIONS

LIST OF TABLE CAPTIONS

TABLE OF CONTENTS

CHAPTER 1

CHAPTER 3

CHAPTER 4

CHAPTER 6

CHAPTER 1

INTRODUCTION AND LITERATURE REVIEW

1.1 Introduction

Oxides are known to possess multitudinous properties, such as ferroelectricity, high permittivity, piezoelectricity, photoelectricity, superconductivity and magnetoresistance, to name but a few. Many oxides are intrinsic semiconductors or can become good semiconductors by proper doping or having variation in their composition contents. Indeed, by considering the abundant species of oxides available and the multitude of possible dopants, one would have no difficulties of envisaging the formation of an all-oxide rectifying p-n junction diode, which is the fundamental unit of electronic devices. The large bandgap of oxide semiconductors also allows the all-oxide diode to be thermally stable. They are expected to run at high temperature and even at high current density. Furthermore, the intrinsic functionalities of the oxides could be incorporated in the p-n junctions to form a host of exotic and useful devices.

ZnO is a well known wide bandgap n-type semiconductor oxide with high excitonic energy and hexagonal wurtzite structure. It is widely recognized as an ideal material for fabricating practical ZnO-film-based optoelectronic devices. In recent years mixing ZnO with other oxides to form binary or ternary oxides is a common strategy to change the electrical and magnetic properties, to tune the energy bandgap and to achieve p-type doping of ZnO based semiconductor.

The unusual rocksalt cubic ZnO phase, which is reported to exist at a pressure of ~100kbar only, has rarely been studied. In view of the fact that many oxides, in particular, functional perovskites, are either of cubic or pseudo-cubic structure, cubic ZnO will be more desirable for forming heterojunction devices. Besides, if ever ZnO based semiconductors are used to make UV diode laser, the parallel pair of crystal planes in cubic ZnO will be ideal for forming a natural optical resonator. In the present work we seek to use simple cubic rock salt structured oxide (MgO) to mix with ZnO. We deposited the mixed oxide by pulsed laser deposition (PLD) method on lattice matched cubic oxide single crystal substrates. The results are that we have forced the (Zn, Mg)O to grow on cubic form. Therefore, efficient hetero-p-n junctions based on ZnO and other cubic oxides can be easily realized.

In this project, we first mixed ZnO (E_{gap}=3.3eV) with MgO (E_{gap}=7.5eV) in order to tune the bandgap and to stabilize ZnO cubic phase in the $Mg_xZn_{1-x}O$ (MZO) binary systems. Solid targets with different x values were fabricated and films were deposited by Pulsed Laser Deposition technique on cubic LAO (100) and MgO (100) substrates, and hexagonal Al_2O_3 (0001) substrates. Microstructure and surface morphology of these films were investigated by X-ray diffraction (XRD), atomic force microscopy (AFM), scanning electronic microscopy (SEM), transmission electron microscopy (TEM), and high resolution TEM (HRTEM). It was demonstrated that excellent single phase cubic MZO (c-MZO) crystalline films with heteroepitaxial relationships of $(100)_{c-MZO}||(100)_{LAO}$ (out-of-plane) and $(011)_{c-MZO}||(010)_{LAO}$ (in-plane), $(100)_{c-MZO}||(100)_{MgO}$ (out-of-plane and in-plane) and $(111)_{c-MZO}||(1000)_{Al2O3}$ were obtained. All the epitaxial c-MZO films show a cubic lattice constant that varies with x in broad agreement with Vegard's law. The surface of the MZO films grown in vacuum atmosphere is reasonably smooth except for some particulates caused by the PLD fabrication process. Transmission throughout the whole visible range is close to 80%, which is measured by a UV-visible transmission spectroscopy at room temperature. Resistivity against temperature range from 150K to 350K is obtained by four-point and two-point electrode methods.

Al_2O_3 and In_2O_3 oxides were doped to the $Mg_xZn_{1-x}O$ system to increase its conductivity. Typical n-type semiconducting thin film characteristics are obtained. Different doping concentration and deposition parameters were attempted. The corresponding thin film microstructure and the temperature dependent electrical resistivity were studied.

NiO is a well-known transparent p-type semiconductor with a band gap of about 3.7eV. Li^+ doping could significantly boost the p-type conductivity. We choose $Li_{0.15}Ni_{0.85}O$ as our p-type material to fabricate all oxide p-n junctions. Based on ZnO material, three different heterostructures, p-$Li_{0.15}Ni_{0.85}O$/n-Nb-STO, p-$Li_{0.15}Ni_{0.85}O$/n-ZnO and p-$Li_{0.15}Ni_{0.85}$/n-$Mg_xZn_{1-x}O$, were fabricated by PLD. Pt electrodes deposited by PLD were used as the electrical leads. Optical transmittance spectrum and I-V rectifying characteristics were measured. The heterojunctions exhibit excellent optical transparency and highly asymmetric electrical rectification, which suggest thepossibility for developing inexpensive, transparent electronics for a wide variety of applications.

1.2 Oxide semiconductors

1.2.1 Introduction

Although most oxides are good insulators, some, such as ZnO and Cu_2O, are well-known semiconductors. In general, oxide semiconductors are not well understood, so they have limited potential for applications at present. The main reason why oxide semiconductor properties are not well understood is the occurrence of ionic bonds in the oxide molecules; the mechanism of transport of current carriers in these materials is hence more complex than in elemental semiconductors or in the compounds with covalent bonds. Along with some examples, drawings of some important oxides structures are shown in Figure 1.1[1-1, 1-2].

1.2.2 Conduction mechanism in oxide semiconductors

In contrast to charge transportation mechanism in conventional semiconductor or metal, conduction in oxides is not only induced by electronic carrier (electron and hole) but often achieved by ionic carrier as well. Although the mobility of ion is always several orders of magnitude lower than that of electron, ionic conduction nevertheless helps to create the n- or p-type conduction in oxides. The n-type conduction oxides are obtained by slight reduction, substitutional doping of higher oxidation state element to replace the lower oxidation state component in the oxide and insertion of electronegative element etc. In all cases negative carrier are introduced into the oxides. Similarly, p-type conduction oxides are achieved by electron removal via oxidation or introduction of positive carriers via doping of lower oxidation state element to replace the higher oxidation state component in the oxide. The mixed-valency has, in fact, rendered some complex transitional metal oxides to possess both n- and p-type conducting properties according to their composition ratio. For example, $Co_{3-x}Fe_xO_3$ is one of the well known transition metal oxide. With $x \geq 2$ it is a n-type conductor and when $x<2$ it has p-type conduction [1-4, 1-5].

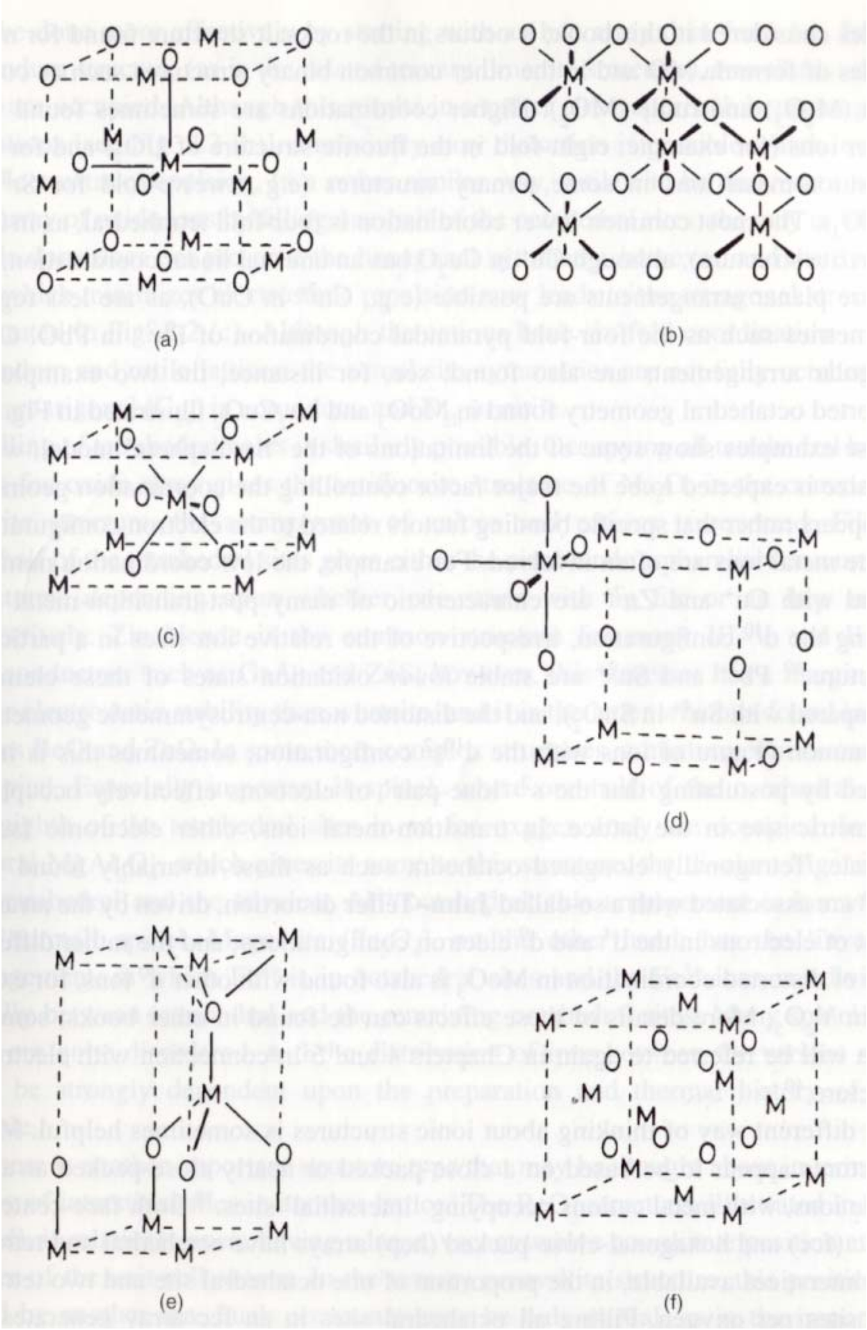

Figure 1.1 Some important binary oxide structures [1-1, 1-2]. (a) Rocksalt, MO; (b) corundum, M_2O_3; (c) rutile, MO_2; (d) ReO_3; (e) wurtzite, MO; and (f) fluorite, MO_2. Crystallographic unit cells are shown except for (b).

1.3 Introduction to oxide doping

The relevant semiconducting properties of oxides originate from the presence of the lattice defects and of foreign atoms (impurities or admixtures). Impurities determine the semiconductive properties of materials and allow us to vary the conductivity from the semi-insulating via the semi-conductive to the semi-metallic range of the conductivity spectrum. The species and concentration of impurities determine the conductivity type and the free carrier concentration of semiconductors. For p-type and n-type impurities the electronic conduction occurs predominantly in the valence and conduction band, respectively. Free carriers must be injected or extracted in all optoelectronic devices. Thus, impurities providing free carriers form the basis of light-emitting diodes, current-injection lasers, photodetectors, and solar cells [1-6, 1-7].

Impurities incorporated into a semiconductor lattice predominantly occupy substitutional lattice sites. In compound semiconductors, the lattice site can be either a cation or an anion site. Which of the two sites is preferred by an impurity depends on a number of factors, including the valence electron correlation between impurity and host, the bond strength between the impurity atom and the surrounding host lattice, and the size of the impurity (strain effect). In practice, the characteristics of impurities are more complex than the simple coulombic substitutional center. An impurity can occupy sites other than substitutional sites, e.g. interstitial sites. Moreover, an impurity may form complexes with lattice atoms, other impurities, and native defects. Electrically, an impurity can be inactive, or compensating, which affects the efficiency of the dopant.

The saturation of the electrical activity at high doping concentrations, and the amphoteric nature of some impurity species determine the properties of doped semiconductors as well. Furthermore, the characteristics of doped semiconductors change quite drastically at high doping concentrations. Effects associated with high doping concentrations are the Mott transition, the Burstein-Moss shift, band tail formation, impurity band formation, and bandgap shrinkage.

During this time, doping has emerged as an entire discipline of semiconductor research and development. This discipline has many facets which are of great importance for further development and for production of photonic and electronic components and integrated microsystems.

1.4 Thin films

1.4.1 Advantages compared with traditional bulk materials

The basic properties of film, such as film composition, crystal phase and orientation, film thickness, and microstructure, are controlled by the deposition conditions. Thin films exhibit unique properties that cannot be observed in the bulk materials [1-8]:

1. Unique material properties resulting from the atomic growth process.

2. Size effects, including quantum size effects, characterized by the thickness, crystalline orientation, and multilayer aspects.

In thin films, deviations from the properties of the corresponding bulk materials arise because of their small thickness, large surface-to-volume ratio, and unique physical structure which is a direct consequence of the growth process. Some of the phenomena arising as a natural consequence of small thickness are optical interference, electronic tunneling through an insulating layer, high resistivity and low temperature coefficient of resistance, increase in critical magnetic field and critical temperature of a superconductor, the Josephson effect, and planar magnetization. The high surface-to-volume ratio of thin films due to their small thickness and microstructure can influence a number of phenomena such as gas adsorption, diffusion, and catalytic activity.

1.4.2 Thin film growth mode

The growth of thin films can be categorized into three different modes[1-9]（see Figure 1.2）, which was first introduced by Ernst Bauer in 1958. Island (Volmer-Weber) growth results in the formation of isolated islands on the surface. This occurs when the cohesive energy of the atoms within the film is greater than the cohesive energy between the film and atoms on the surface. Layer-by-Layer (Frank-Van der Merwe) growth involves a deposition of one monolayer at the time and results in a very smooth epitaxial film. Growth mode arises when the atoms of the deposit material are more strongly attracted to the substrate than they are to themselves. The cohesive energy will decrease monotonically as each film layer is added. Mixed growth mode (Stranski-Krastanov) involves growth of islands after the first monolayer has been formed successfully. This occurs when the monotonic decrease in binding energy is energetically over-ridden by other factors such as strain due to lattice mismatch, with the result that island formation becomes more favorable. PLD is known to have very high deposition rate. The process therefore favors Frank-Van der Merwe mode growth.

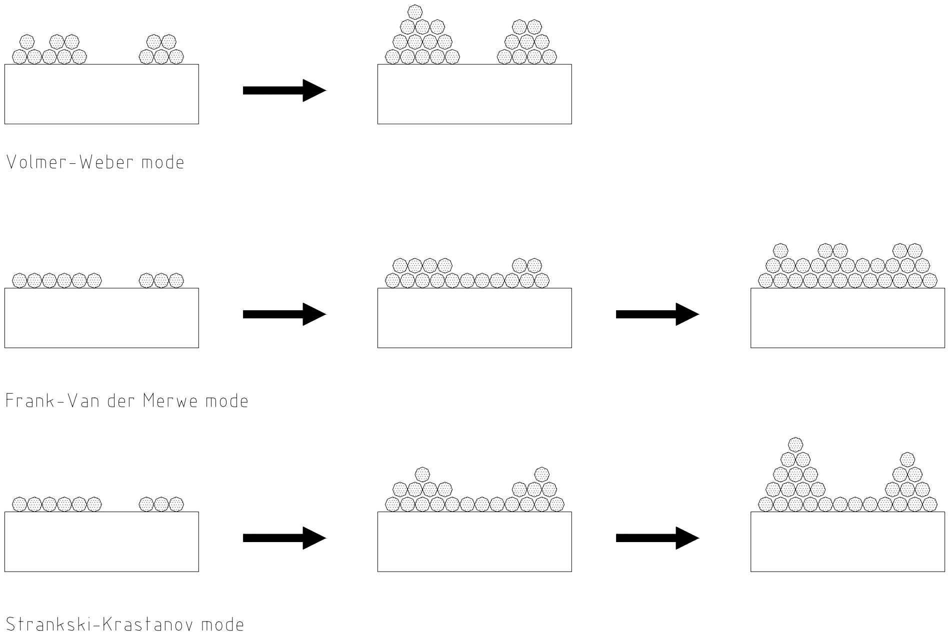

Figure 1.2 The common modes of film growth (i) Island (Volmer-Weber) mode, (ii) Layer-by-Layer (Frank-Van der Merwe) mode and (iii) Mixed (Stranski-Krastanov) mode.

1.4.3 Epitaxial growth definition

“Epitaxy” is in fact derived from the Greek-term meaning “equal” and “in ordered manner”. It refers to the film growth phenomenon where a well defined and simple relation between the structure of the film and the substrate exists. In particular it commonly denotes a single crystalline layer grown on a single crystal surface. If the single crystalline film and the single crystal substrate are of the same material, we call the growth homoepitaxy. If they are different materials, we call the growth heteroepitaxy. In epitaxial growth of thin film, the crystal structure of the substrate serves as a template for the arrangement of the atoms in the growing layer. Many layers can be stacked on top of each other to form multilayered samples with atomically sharp junctions, and all of the grown layers adopt a definite crystalline relationship to the substrate. In order to verify the quality of the crystalline structure of films, it is essential to consider several important factors.

A primary consideration in forming epitaxial layers on any type of substrate is the chemical reaction, including chemical bonding and chemical diffusion. To illustrate this point we may take, for example, epitaxial growth of metal oxides on silicon. It is essential to oxidize the metal species rather than the silicon substrate, since the formation of even a thin amorphous silicon oxide layer before epitaxy is established would prevent epitaxy altogether.

A secondary consideration is the structural similarity of the deposited layer and the substrate. Since the materials of the films and the substrate may not be the same, their crystal structure and lattice parameter are normally different. The difference in lattice parameter between the film and the substrate is called "lattice mismatch". The lattice mismatch (f) is defined as:

$$f = \frac{\left| a_s - a_f \right|}{a_s}$$

Where a_s and a_f are the lattice constant for substrate and film, respectively. In the conventional approach, the lattice mismatch should be small enough so that there is a smooth transition in atomic arrangement from one material to another. Otherwise, the bonding between atoms across the interface of the components will be irregular and weak. As a result, the films can peel off, crack, or contain a large density of crystalline defects.

Another consideration in forming an epitaxial film on a substrate is their compatibility in thermal expansion coefficient. The total strain in the film is a combination of multiple sources such as the intrinsic strain incurred during growth, transformation strain, and strain induced by the mismatch in thermal expansion coefficient. Frequently, the latter effect dominates; the stress built up in the film can be defined as:

$$\sigma_{th} = \frac{E_f}{1-\nu_f}\varepsilon_{th} = \frac{E_f}{1-\nu_f}\int_{T_o}^{T}(\alpha_f - \alpha_s)dT$$

Where E_f is the film Young's modulus, ν_f is the Poisson ratio, α is the thermal expansion coefficient and T represents the temperature.

When the thermal strains exceed the elastic limit of the film, they are relaxed by various mechanisms such as dislocation glide. As the relaxation processes are inherently accompanied by simultaneous changes of the film morphology they are often detrimental for the stability and performance of thin-film devices, which are not operated at their deposition temperature.

1.4.4 Different growth method of films

There are three categories of thin film process: physical vapor deposition (PVD), chemical vapor deposition (CVD), and wet chemical methods [1-8]. Figure 1.3 illustrates the classification of the different deposition processes.

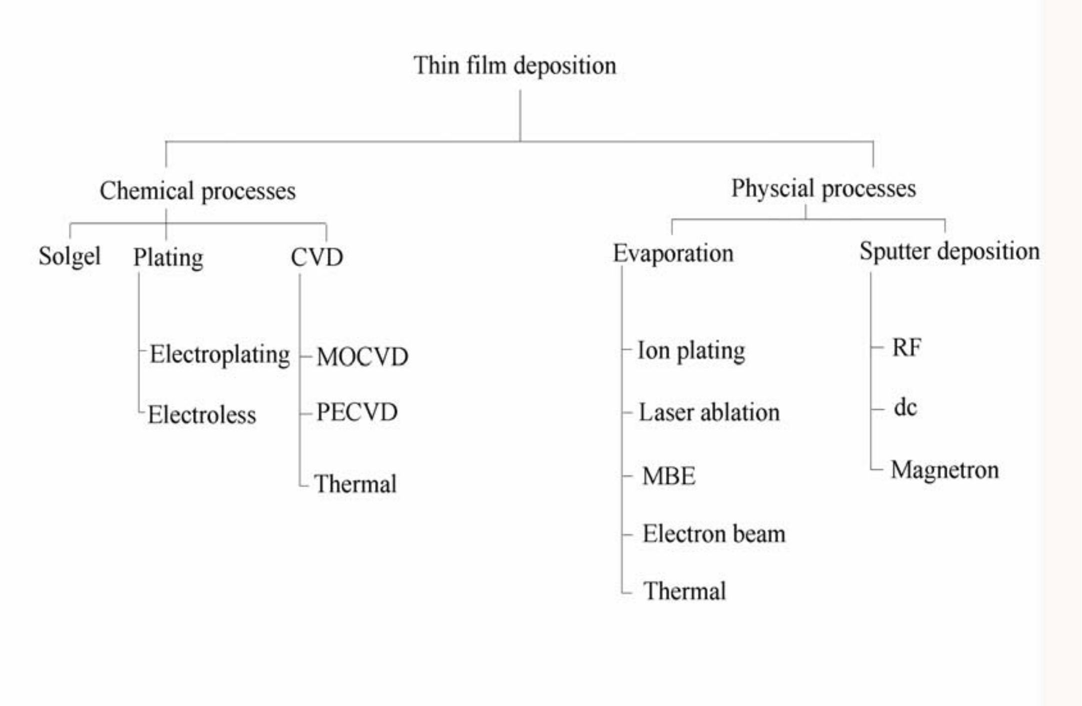

Figure 1.3 Classification of the most common deposition processes [1-8].

1.4.4.1 Evaporation

Perhaps the simplest film deposition technology, vacuum evaporation is a versatile technique that can be used to deposit most materials. This is a PVD process and has the advantage of high deposition rates, simplicity, and relative ease of use. Vacuum evaporation is used for deposition of conductor materials in electronic circuits and devices, for the application of dielectric and optical coatings, and for developing technologies, such as high-temperature superconductors.

Vacuum evaporation is used by heating a source material under vacuum until it evaporates or sublimes. This evaporant is then deposited or condensed onto a substrate surface to form a film. The source material melts into a liquid and subsequently evaporates into a gaseous vapor or sublimes directly into a gaseous state.

1.4.4.2 Molecular beam epitaxy

Molecular beam epitaxy (MBE) is a highly developed technique used to perform a wide variety of epitaxial depositions, from Ⅲ-Ⅴ semiconductors to high-temperature superconductors. The basic film growth concept is essentially a refinement of vacuum evaporation, in which thermal or electron beam sources are used to generate and deposit a beam or flux of atomic or molecular species. There are several sources with varying flux rates that can be used to grow complex compounds with precise elemental compositions. MBE sources are focused on a substrate, which is heated to provide a high degree of surface mobility for incident species. The resulting condensation of molecular or atomic flux results in the formation of a crystalline film, one monolayer at a time. Unlike the majority of thin film deposition techniques, MBE is performed in an ultra-high vacuum environment that is often greater than 6×10^{-9}Pa (5×10^{-11} torr). This allows the deposition of contaminant-free films.

1.4.4.3 Sputter deposition

Sputtering is a PVD process involving the removal of material from a solid cathode. This is accomplished by bombarding the cathode with positive ions emitted from a rare gas discharge. When ions with high kinetic energy are incident on the cathode, the subsequent collisions knock loose, or sputter, atoms from the material. The process of transferring momentum from impacting ions to surface atoms forms the basis of sputter coating. Sputtering was originally developed to deposit refractory metals, which could not be deposited using the thermal evaporation techniques of that time. Today, sputtering has developed into a versatile deposition technique that is able to deposit most materials.

1.4.4.4 Chemical vapor deposition (CVD)

CVD relies on reactive carrier gases to transport precursors of the desired material to the substrate surface. Here they react with other gases or decompose to produce stable reaction products, which are deposited on the substrate. CVD methods are among the most versatile deposition techniques because a wide range of chemical reactants and reactions can be used to deposit a large number of different types of films for a wide range of applications. Some of the more common CVD techniques include: metalorganic CVD(MOCVD), which uses a thermally heated reaction chamber and sources that are organometallic in nature; plasma-enhanced CVD(PECVD), which uses a plasma discharge to provide the excitation necessary for chemical reaction to occur; and atmospheric pressure CVD(APCVD), which does not require a vacuum, and can be performed in a continuous process with a belt transporting a continuous flow of substrates in and out of the deposition chamber.

1.4.4.5 Laser ablation [1-8]

Laser ablation uses a high-power pulse to vaporize a small area of target material. Figure 1.4 illustrates a laser ablation system in action and the schematic layout of the ablation system. The cloud of the target material generated is then deposited onto a nearby substrate. This type of process is usually performed in a high-vacuum chamber, which provides a window for the laser pulse from an external laser source. Ultraviolet excimer lasers delivering 0.1 to 1 Joule (J) pulses of 15 to 45 nanoseconds (ns) duration are commonly used. With laser running at 1 to 100 hertz (Hz), material deposition rate of 0.1 to 100 nanometers per second (nm/s) are achieved [1-10]. By scanning the laser beam across the target and rotating the substrate, the target is consumed in a uniform manner and a uniform film can be produced. Detailed introduction will be given in section 1.7.

1.4.4.6 Plating

The basic process of plating involves the deposition of a metal film using a chemical reaction. There are two types of plating: electroplating and electroless plating. The difference between these techniques, as the names suggest, is that electroplating requires an applied electrical voltage and electroless plating does not. Electroplating can only be performed on conductive substrate or films, but can be used to produce films with thickness up to tens of micrometers (μm). Under proper conditions, electroplating can provide high aspect ratios, dense packing and accurate pattern reproduction. In contrast, electroless plating can be performed on dielectrics and conductors; however, it is usually used for thin protective coatings. Plating is used for a wide range of applications including anticorrosion coatings, interconnect metallization formation, via formation in electronic circuits and devices, and Au and Ni coatings for wire bonding.

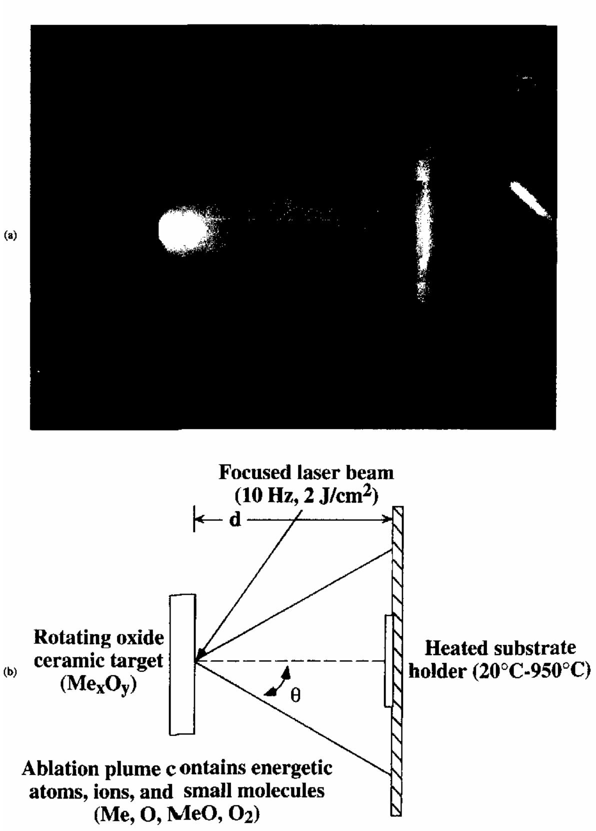

Figure 1.4 (a) A laser ablation system in action, illustrating a laser beam striking a target and a plume of material being deposited on an adjacent substrate. (b) Schematic layout of a laser ablation system used to deposit metal oxides [1-8].

1.4.4.7 Sol-gel coatings

Sol-gel films result from spin coating, dipping, or spraying a chemical solution onto a substrate. The solution is a stable mixture of suspended precursor particles known as a sol-gel. Once applied to a substrate, a transition or destabilization of the sol occurs. This is marked by a significant increase in the viscosity of the coating, resulting in the formation of a tacky gel. The gel is hardened to form a film by drying, typically in air, at 100°C to 125°C. Although the films are deposited at room temperature, a high temperature heat treatment is usually required to create a dense adherent film. Sintering temperatures are typically in excess of 300°C. The advantages of this process include high purity and a very-high degree of homogeneity over large areas. The primary disadvantages are the high cost of the materials and the narrow range of materials that can be deposited with this technique. A number of applications have been demonstrated for this process. These include sensors, optical coatings, and transparent conductors [1-11].

1.5 Substrates for thin film deposition

The function of the substrate is to provide the base onto which thin film circuits are fabricated and various thin film multilayers are deposited. In addition, the substrate provides the necessary mechanical support and rigidity needed for a reliable circuit, and it has adequate thermal management ability to ensure proper temperature operation and proper electrical insulation to withstand high voltages without breakdown. Dielectric strength, dielectric constant value, dissipation factor, electrical conductivity, thermal conductivity, and flexural or mechanical strength are important substrate properties that are affected by their microstructure, composition, and processing. Commonly used substrate materials for thin film circuits include alumina, glass, beryllia or beryllium oxide-based ceramic, aluminum nitride, silicon (Si), and metals. Ceramic materials are often used for thin film applications because ceramics have high thermal conductivity, good chemical stability, and are also resistant to thermal and mechanical shocks.

The properties of the substrates used to grow defect-free films include:

- good surface smoothness (surface finish can vary from about 50 μm/in for 96% aluminum oxide content to 20μm/in for 99.5% aluminum oxide content)
- coefficient of thermal expansion (CTE) matched
- good mechanical strength (>350 MPa)
- high thermal conductivity
- inertness, or chemical stability
- low cost
- high electrical resistance (>$10^{14}\Omega\cdot$cm)
- good uniformity

1.6 Related research work on ZnO and MgO thin films

1.6.1 Properties, advantages and applications of ZnO

In the class of optoelectronic materials, ZnO is emerging as a potential candidate due to its direct and wide band gap and its ability to tailor electronic, magnetic, and optical properties through doping, alloying, quantum wells and heterostructures, and nano-engineering [1-12, 1-13, 1-14]. Tailored materials and heterostructures are necessary to build many technologically important devices like laser diodes, visible and solar blind detectrors, transparent electronics based on thin film field effect transistors, and spintronic devices. ZnO crystallizes stably in wurtzitic hexagonal crystal structure (space group $P6_3mc$), as shown in Figure 1.5, in which Zn and O planes are alternately stacked along the c-axis direction. For cubic ZnO, the coordinations of Zn^{+2} and O^{-2} are both four-fold. Like Mg^{+2} and O^{-2} in MgO, they lead to cubic ZnO phase system.

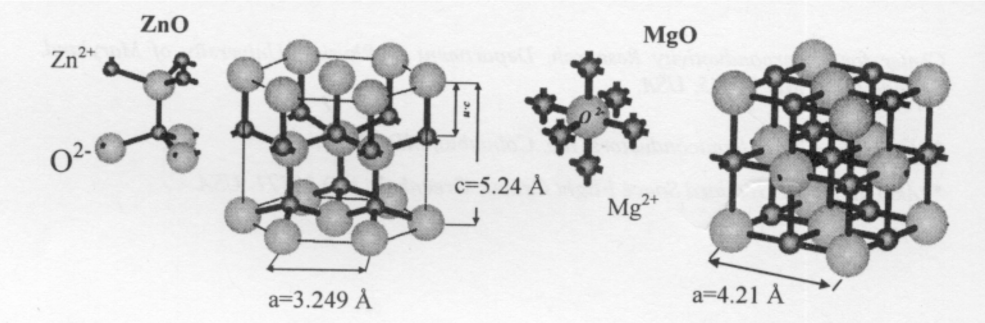

Figure 1.5 Crystal structures of ZnO and MgO.

ZnO films deposited by Webb et al.[1-15] using r.f. magnetron sputtering in an Ar-H_2 mixture at $T_s \approx 75°C$ had a typical as-deposited resistivity of about $2 \times 10^{-3} \Omega cm$ ($N \approx 10^{20} cm^{-3}$; $\mu \approx 8 cm^2 V^{-1} s^{-1}$) and an optical transmittance in the visible spectrum T≈90%. It has a direct bandgap of 3.3eV at room temperature with the energy band parameters, such as electron and hole effective masses, as well as optical and electrical properties that are quite comparable to that of GaN, a material that is well established for blue LED and semiconductor laser diode. In fact, ZnO is a much more intense and efficient UV emitter (at least 4 to 5 times more intense) at its band edge than GaN, owing to the fact that it has a higher free exciton binding energy (~60meV) that is more than twice than that of GaN (~25meV) [1-16, 1-17]. The radiative recombination in ZnO is mediated by excitons. This should lead to narrow emission linwidths, whereas it is band-to-band transition in GaN system yielding broad bandwidths. Based on these properties, it is envisioned that ZnO system has a niche for a wide range of devices such as blue and UV light emitting diodes, heterojunction diode lasers[1-18, 1-19], visible and solar blind ultra-violet light detectors[1-20, 1-21], optical waveguides, spintronic devices based on dilute magnetic semiconductors[1-22, 1-23, 1-24, 1-25], piezoelectric devices, surface acoustic wave-based photodetector devices[1-26], and resonant tunneling devices[1-27]，as well as transparent thin film transistors for displays[1-28].

There are many advantages of ZnO based heterostructures for processing. It is believed that ZnO wafer production process will scale at a faster rate than that of GaN, or other common non-oxide wafer candidates for ultraviolet applications because of the differences in the wafer growth processes [1-29]. Sapphire is also known to be a most common substrate for heteroepitaxy despite large lattice mismatch (~17%) with ZnO. Additionally, ZnO lattice matches with GaN (within 2%), making epi-GaN/sapphire as an ideal substrate for heterostructure junction with minimal bandgap distortion from lattice strain that could facilitate hybrid device technologies. Moreover, ZnO can be deposited at low-deposition temperatures by low-cost deposition techniques, such as RF sputtering, pulsed laser deposition (PLD), and chemical vapor deposition (CVD). Another interesting feature of ZnO is its ionic nature that lends itself to ease in the microfabrication process using both wet [1-30] and dry etch [1-31] techniques.

1.6.2 $Mg_xZn_{1-x}O$ alloy heterostructures

Band gap tailoring refers to the ability to tune the band structure of a semiconductor which is useful for tailoring the performance of optoelectronic devices. Band gap tailoring of semiconductors can be typically achieved by:

- Alloying two or more semiconductors.
- Use of heterostrucutures to cause quantum confinement or formation of superlattices.
- Use of strained epitaxy.

Band gap engineering of ZnO is possible and it can be achieved easily in thin film heterostructures. Three major substitutional elements have emerged as candidates for bandgap tailoring: Mg [1-32, 1-33, 1-34], V [1-35] and Cd [1-36]. Mg and V are known to broaden the bandgap, whereas Cd is known to narrow it. Out of these dopants Mg has following advantages: First, the ionic radius of Mg^{2+} is comparable to that of Zn^{2+}: 0.57Å and 0.60Å, respectively. Second, it is possible to widen band gap of the alloy in the same way that band gap widening has been shown in Ⅲ-Ⅴ compounds. In principal, the band gap of $Mg_xZn_{1-x}O$ alloy can be tuned from 3.3 up to 7.8eV by tuning the Mg content from 0-100% [1-34]. The corresponding cutoff wavelength range is ~400-157nm. This variation of band gap as a function of alloy composition is the largest one that can be found in well established semiconductor systems such as GaAs, AlGaN and Si [1-37].

Realization of Mg-Zn-O alloy is challenged by the incompatible electronic configuration and crystal structure of MgO (NaCl type cubic structure with lattice constant a=4.24Å) and ZnO (wurtzite, hexagonal structure with lattice constants a= 3.24Å and c= 5.20Å). According to the phase diagram of ZnO-MgO binary system, solid solubility of MgO in ZnO is less than 4 mol% [1-38]. This situation is in contrast to the standard semiconductor alloying e.g. AlGaN and AlGaAs, where two (or more) components of the alloy have the same crystal structure so that the final alloy also has the same crystalline structure [1-39].

In spite of a large structural dissimilarity and limited solid solubility between ZnO and MgO, Ohtomo et al[1-32] demonstrated the first synthesis of high-quality, single-phase $Mg_xZn_{1-x}O$ thin films with Mg concentrations up to 33 at.% due to the non-equilibrium nature of the pulsed laser deposition(PLD) growth. Above 33%, MgO is reported to segregate from the wurtzite MgZnO lattice limiting its band gap maximum up to 3.9eV. Although there are reports of molecular beam epitaxy (MBE) [1-17] and metalorganic vapour-phase epitaxy (MOVPE)[1-40] growth with Mg containing up to 49 at.%, most of the MgZnO thin film growth has been carried out by PLD[1-32, 1-33, 1-41]. It should be noted that all the above-mentioned MgZnO thin films possess hexagonal structure. On the other hand, the phase diagram predicts a solid solution of ZnO in the cubic MgO lattice up to 40at.%, and very recently, Choopun et al[1-42] and Narayan et al[1-38] reported on the growth of cubic $Mg_xZn_{1-x}O$ thin films grown by PLD, with Mg composition x in the range of 0.50-0.86 and 0.82-1.00, respectively.

Due to dissimilarity of crystal structures between ZnO and MgO, the change of a crystal structure will be the inherent drawback of the Mg-Zn-O system that can inevitably cause phase separation and mixed phases for certain composition. Thus, discontinuity is expected when tuning the bandgap from one end to the other. Minimizing the phase separation region is thus a necessary step toward realization of high quality $Mg_xZn_{1-x}O$ thin films and alloy heterostructures. Shown in Figure 1.6[1-34] is the summary of the band gap alloying in thin films grown by pulsed laser deposition as a function of Mg content in ZnO and its optical properties. $Mg_xZn_{1-x}O$ thin films alloys with Mg content between 40 to 60 mol% are not single phased. For x >0.6, all Mg-rich alloys are found to be cubic phase similar to that of MgO structure.

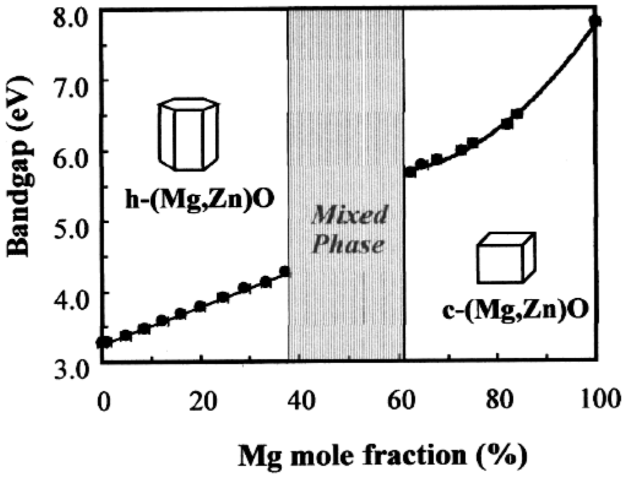

FIG. 6. Composition tuned $Mg_xZn_{1-x}O$ band gap and the corresponding phases. The shaded area is the phase separated region that has no well defined band gap. The band gap of pure MgO is represented by an open circle at $E_g = 7.8$ eV.

1.7 Pulsed Laser Deposition(PLD)

1.7.1 Mechanisms of PLD

The principle of pulsed laser deposition, in contrast to the simplicity of the system set-up, is a very complex physical phenomenon. It involves all the physical processes of laser-material interaction during the impact of the high-power pulsed radiation on a solid target. It also includes the formation of the plasma plume with high energetic species, the subsequent transfer of the ablated material through the plasma plume onto the heated substrate surface and the final film growth process. Thus PLD generally can be divided into the following four stages.

1. Laser radiation interaction with the target
2. Dynamic of the ablation materials
3. Deposition of the ablation materials with the substrate
4. Nucleation and growth of a thin film on the substrate surface

In the first stage, the laser beam is focused onto the surface of the target. At sufficiently high energy densities and short pulse duration, all elements in the target surface are rapidly heated up to their evaporation temperature. Materials are dissociated from the target and ablated out with stoichiometry as in the target. The instantaneous ablation rate is highly dependent on the fluences of the laser irradiating on the target. The ablation mechanisms involve many complex physical phenomena such as collisional, thermal, and electronic excitation, exfoliation and hydrodynamics.

During the second stage the emitted materials tend to move towards the substrate according to the laws of gas-dynamic and show the forward peaking phenomenon [1-43]. R. K. Singh [1-44] reported that the spatial thickness varied as a function of $\cos^n q$, where n>>1. The laser spot size and the plasma temperature have significant effects on the deposited film uniformity. The target-to-substrate distance is another parameter that governs the angular spread of the ablated materials. Hanabusa [1-45] also found that a mask placed close to the substrate could reduce the spreading.

The third stage is important to determine the quality of thin film. The ejected high-energy species impinge onto the substrate surface and may induce various type of damage to the substrate. The mechanism of the interaction is illustrated in the following Figure 1.7. These energetic species sputter some of the surface atoms and a collision region is established between the incident flow and the sputtered atoms. Film grows immediately after this thermalized region (collision region) is formed. The region serves as a source for condensation of particles. When the condensation rate is higher than the rate of particles supplied by the sputtering, thermal equilibrium condition can be reached quickly and film grows on the substrate surface at the expenses of the direct flow of the ablation particles.

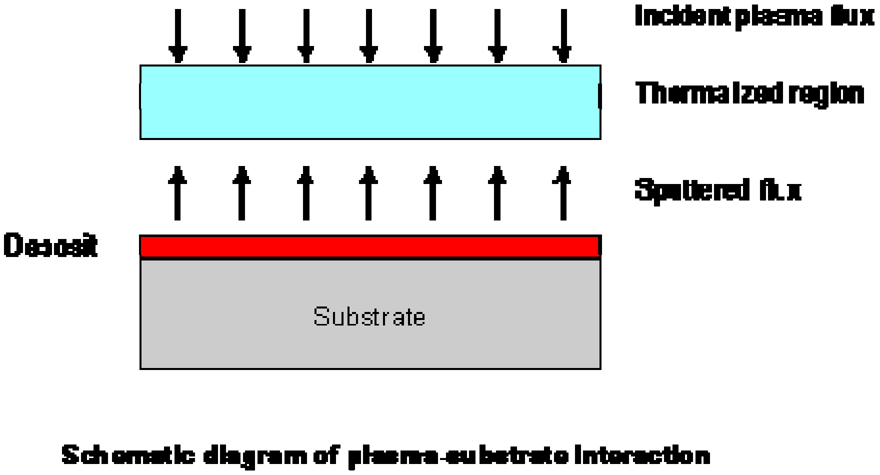

Figure 1.7 Schematic diagram of plasma-substrate interaction.

Nucleation-and-growth of crystalline films depends on many factors such as the density, energy, degree of ionization, and the type of the condensing material, as well as the temperature and the physical-chemical properties of the substrate. The two main thermodynamic parameters for the growth mechanism are the substrate temperature T and the supersaturation Dm. They can be related by the following equation

$$\mathrm{D}m = kT\, ln(R/R_e)$$

where k is the Boltzmann constant, R is the actual deposition rate, and Re is the equilibrium value at the temperature T.

The nucleation process depends on the interfacial energies between the three phases present - substrate, the condensing material and the vapour. The minimum-energy shape of a nucleus is like a cap. The critical size of the nucleus depends on the driving force, i.e. the deposition rate and the substrate temperature. For the large nuclei, a characteristic of small supersaturation, they create isolate patches (islands) of the film on the substrates, which subsequently grow and coalesce together. As the supersaturation increases, the critical nucleus shrinks until its height reaches an atomic diameter and its shape is that of a two-dimensional layer. For large supersaturation, the layer-by-layer nucleation will happen for incompletely wetted foreign substrates.

The crystalline film growth depends on the surface mobility of the adatom (vapour atoms). Normally, the adatom will diffuse through several atomic distances before sticking to a stable position within the newly formed film. The surface temperature of the substrate determines the adatom's surface diffusion ability. High temperature favours rapid and defect free crystal growth, whereas low temperature or large supersaturation crystal growth may be overwhelmed by energetic particle impingement, resulting in disordered or even amorphous structures.

Metev and Veiko [1-46, 1-47] suggested that the N_{99}, the mean thickness at which the growing, thin and discontinuous film reaching continuity is given by the formula:

$$N_{99} = A\,(1/R)^{1/3} \exp(-1/T),$$

where R is the deposition rate (supersaturation related) and T is the temperature of the substrate and A is a constant related to the materials.

In the PLD process, due to the short laser pulsed duration (~10 ns) and the small temporal spread (<10 μs) of the ablated materials, the instantaneously deposition rate can be enormous (~10 μm/s). Consequently a layer-by-layer nucleation is favoured and ultra-thin and smooth film can be produced. In addition the rapid deposition of the energetic ablation species helps to raise the substrate surface temperature. In this respect PLD tends to demand a lower substrate temperature for crystalline film growth.

1.7.2 Historical development of PLD

After the first high-power ruby laser was demonstrated by T.H.Maiman at Hughes Research Laboratories in 1960[1-48]，there were a lot of theoretical and experimental studies on the interactions of intense laser beams with solid surfaces[1-49], liquids[1-50], and gaseous materials[1-51]. The ease with which material was vaporized suggested that the intense laser radiation could be used to deposit thin films. This idea was quickly demonstrated after a few years [1-52]. As the laser technology was still immature at that time. The devolopment of PLD was slow.

In the 1970's, there a major breakthrough came about in PLD when electronic Q-switch was developed to deliver short pulses with very high peak laser power density exceeding 10^8 Wcm^{-2}. At such power density, the laser can virtually ablate any material. As a result, PLD became a versatile method to deposit thin films of a wide choice of materials. Moreover, the development of the high-efficiency harmonic generator in this period allowed laser to deliver shorter wavelength radiation. The absorption depth of short wavelength in the target material radiation is shallower. In addition, UV radiation enhances non-thermal interaction which promotes congruent evaporation and minimizes "splashing". As a result, high quality stoichiometric films can be easily produced.

In the 1980's, as excimer lasers, which deliver up to 1J of pulsed UV/deep UV laser energy in ~10ns became readily available, PLD was already established as a major film growth technique. It has been extensively used by researchers to fabricate thin films of various materials, ranging from metal and semiconductors to ceramics and polymers.

Another breakthrough was triggered by the successful growth of high T_c superconducting films in 1987[1-53]. It has been further proved that PLD is an applicable and convincible technique to explore new frontier in thin film material research.

Since then, PLD has been widely adopted in obtaining heteroepitaxy of oxides on semiconductors [1-54] and the growth of perovskite ferroelectric film [1-55]. Nitrides [1-56], epitaxy layers of TiN on (100) Si substrate [1-57], the synthesis of buckminster fullerenes (i.e. C60) [1-58] and various superlattic growths by PLD have also been reported. Production-related issues concerning reproducibility [1-59], large area scale-up [1-60] and multiple-level devices have also begun. Furthermore, Ultra-Fast Pulsed Laser Deposition (Ultra-Fast PLD) installation has been designed and constructed in 1997 at the Laser Physics Center, Australian National University. The outcome has been a spectacular increase in the deposition rates. Moreover, the first experiments of this group on evaporation of graphite demonstrated that the microroughness of the deposited diamond-like film is extremely low-it is in the order of atomic layer thickness. The technique makes it possible to eliminate the major disadvantage of the conventional laser deposition method, which is the presence of particulates affecting the film quality. Whereas particulate-free and atomically flat surfaces are definitely desirable attributes of femto second laser PLD, the as-deposited film crystallinity has not been emphasized.

Indeed, for most cases, in particular for oxide materials, the crystallinity of the deposited film is not as good as laser PLD.

1.7.3 Some fundamental parameters for thin film deposition

The quality of the as-grown films is very sensitive to some physical parameters such as the substrate temperature, the kinetic energy of the deposition flux and the deposition rate. Effects from background gas are also critical in some cases.

1.7.3.1 Substrate temperature

In the initial stages of the film growth the flux deposited on the substrate might re-evaporate from the surface, nucleate into a cluster, be consumed by existing clusters or be trapped on a surface defect site. All these processes are dependent upon the mobility of the deposited atom on the surface. Natural high mobility occurs at high substrate temperatures.

The microstructure of the deposited films is very often determined by the substrate temperature. Also it is well known that the closer the substrate temperature to the melting temperature of the film, the more film relaxation channels are energetic accessible. Hence, the substrate temperature can be used as a processing parameter to induce different structures.

1.7.3.2 Energy of the deposition flux

Growing films from species impinging at higher kinetic energies generally improves the film quality [1-61]. The effects of high kinetic energy ion bombardment of the substrate include ballistic collision, ion mixing and thermally simulated exchange mixing. These effects help to raise the substrate temperature which in turn governs the film properties like film stress and crystal structure. An important manifestation of depositing high incident kinetic energy species is that quality crystalline films can be obtained at a much lower substrate temperature.

1.7.3.3 Deposition rate

The deposition rate can vary over a wide range and is strongly dependent on the nature of the materials to be deposited. It has to be considered on a case by case basis. The influence of the deposition rate on the grown films is complicated. However, there are some useful guidelines to follow. Too high a deposition rate causes film deterioration because of the reduced opportunity for film relaxation. Too small a deposition rate, on the other hand, demands high vacuum. The lower the deposition rate, the more chance the film will incorporate unwanted gaseous impurities. In addition, the deposition rate needs to be higher than the deposition rate in order to lay a material layer.

1.7.3.4 Vacuum quality and background gas

Two additional effects arise as the result of introducing background gas, namely, chemical reaction and non-reactive thermal collision between the energetic flux and the background gas. Using high kinetic energy deposition fluxes in a background gas can induce gas phase reactions, which might compensate for some loss of a constituent element such as oxygen or nitrogen in the oxide and nitride films, respectively. Numerous such examples are found in PLD. A representative example is the formation of YO from the ablation of Y in O_2 [1-62, 1-63].

Introduction of a background gas is not universally advantageous to all deposition techniques. The kinetic energy and angular distribution of the ablated fluxes can be controlled by the introduction of a background gas. In general, high background gas pressure reduces the kinetic energy of the ablated species. The deposition fluxes are confined in the forwarding direction. As a result, the deposition yield is much higher in the central direction. However, the uniformity of the deposited film thickness is limited to a small region normal to the target surface. Also, the vapor species can undergo enough collisions that nucleation and growth can occur to form particulate before their arrival at the substrate. On the contrary, lower ambient pressure or vacuum produces a uniform film of much bigger area, at the expenses of reduced deposition yield.

1.7.4 Advantages and disadvantages of PLD

Conceptually and experimentally, PLD is extremely simple, probably the simplest among all thin film growth techniques. Film growth can be carried out in a reactive environment containing any kind of gas with or without plasma excitation. This process is flexibility, fast response, energetic evaporants and congruent evaporation. The advantage of PLD method over other deposition techniques such as molecular beam epitaxy and metallorganic vapor phase epitaxy includes the unique capability of transferring any source materials to the surface of a substrate. Its pulsed nature, which affords high controllability of the deposition thickness, plus the potential of synchronizing the high flux/short duration pulses with pulsed reactive gas sources makes PLD a desirable film growth technique. Since the focused laser beam has a very high energy density which can evaporate all the components simultaneously, irrespective of their difference in melting point. The high kinetic energy of the ablation plume, which promotes surface mobility adatoms on the grown films helps in crystallization and improving the structural quality.

PLD allows for easy handling, since the laser source is placed outside the reaction chamber. The emission of energetic ions during laser-target-vapor interaction has an important influence on the layer formation, i.e. it enables growth of adherent and epitaxial films at lower temperature than other methods. A lower deposition temperature reduces the undesirable substrate interdiffusion processes, thermally induced internal stress and re-evaporation of volatile components. This is especially important for the deposition on impurity doped compound and complex materials having low melting point components. In addition, the PLD method allows the in-situ growth of different materials. For example, using a rotating multi-target holder, the laser beam can be rastered different targets by setting a suitable alignment.

Comparing with other film growth techniques, the vacuum requirement of PLD is less stringent and can be achieved by a relatively economical pumping system. It enables us to fabricate films in high partial pressures of reactive gas such as oxygen. The presence of reactive gas can help to bind volatile species to the substrate, preserving the film stoichiometry. PLD has a distinct advantage over sputtering in that it does not require a constant glow discharge, which can limit independent control of process parameters.

There are certain disadvantages of using PLD. The presence of particulate is an intrinsic problem adhered to PLD. The size of particulates can be as large as ~μm, which is bigger than the thickness dimension of the deposited film. They induce defects and inhibit the formation of atomic flat film surface. The numbers of the particulates can be greatly reduced by placing a blocking mask in between the substrate and the target holder, and this is called “eclipse” method. Due to the limited angular spread of the plume, deposition of films on large-area substrates may be difficult. The thickness of the film is the highest at the center of the plasma plume and decreases rapidly with the distance away from the center point. So for large area film the uniformity is not good. It can be improved somewhat by tilting and rotating the substrate.

1.8 Objectives of research

The high exitonic energy of ZnO allows efficient emission at high temperature. In order to utilize this feature we would wish to maximize the ZnO content in $Mg_xZn_{1-x}O$ system yet retaining the cubic structure. The high-pressure phase of rocksalt structure ZnO is metastable at low pressure and readily reverts back to the normal wurtzite structure under ambient condition. A likely solution is to use MgO(100) substrates to grow $Mg_xZn_{1-x}O$ films. The perfectly lattice matched cubic MgO may help to stablize the high pressure cubic ZnO and lead to cubic $Mg_xZn_{1-x}O$ with $x<0.5$. The ability to trap the cubic phase of ZnO in ambient condition would also allow epitaxial growth of $Mg_xZn_{1-x}O$ films on Si or GaAs via buffer layers. This approach could lead to monolithic integration of ZnO based devices with electronic supporting circuits on a single chip for blue/UV optoelectronics.

N-type semiconducting can be readily achieved in ZnO based oxide either through intrinsic oxygen vacancy and Zn rich condition, or via trivalent element doping. Appropriate metal doping, such as Al and In, could increase the electrical conductivity of ZnO and lead to transparent conducting oxide (TCO), which are much preferable for the fabrication of p-n junction used as UV-detectors. Combined with other p-type conducting oxides such as Li-doping NiO or LSMO, hetero- TCO p-n junctions could be realized. In these kinds of rectifying junctions, more wealthy and potentially useful electrical properties could be provided than the conventional diodes due to the rich choice of oxides and their dopants. In addition, high temperature diode operation is allowed because of the large bandgap of these oxide semiconductors. Development of portable UV-detector that is mainly composed of wide-gap TCO semiconductor pn-junction has been required to date and attracted much interest recently.

In this project, we attempt to:

1. synthesis of cubic $Mg_xZn_{1-x}O$ for x<0.5 on LAO(100) and MgO(100) substrates and study its structural, electrical and optical properties.
2. study the different substrate impact on $Mg_xZn_{1-x}O$ (0<x<1) and bandgap engineering
3. dope with other element to tune the electrical conductivity of cubic $Mg_xZn_{1-x}O$ while keeping the original structure
4. fabricate all oxide hetero- p-n junctions with good rectifying properties:
   p-$Li_{0.15}Ni_{0.85}O$/n-Nb-STO, p-$Li_{0.15}Ni_{0.85}O$/n-ZnO
   and p-$Li_{0.15}Ni_{0.85}O$/n-In-$Mg_xZn_{1-x}O$

1.9 Outline of thesis

Background theory related to this research project and literature review on ZnO and $Mg_xZn_{1-x}O$ doping thin films with their related research work are described in this chapter. Conduction mechanism in oxide semiconductors, thin film growth mode and epitaxial growth definitions are discussed. A brief introduction of pulsed laser deposition technique is also presented including the working mechanism, historical development as well as the advantages and disadvantages of utilizing PLD to prepare complex oxide thin films.

Chapter 2 introduces the experimental techniques and various characterization methods. PLD setup with each of the equipment used in the system is sequentially discussed. We also describe the experimental procedures including target fabrication, substrate preparation and the film deposition process. This chapter also introduces the measurement techniques such as XRD, TEM, and I-V characteristic measurements.

In chapter 3, we report the preparation of $Mg_xZn_{1-x}O$ targets and alloy $Mg_xZn_{1-x}O$ thin films on different kinds of substrates. $Mg_xZn_{1-x}O$ targets with different chemical composition have been fabricated, and detailed procedures of which are described. Deposition conditions of $Mg_xZn_{1-x}O$ films are listed in this chapter. Finally optimization of deposition conditions to obtain high quality epitaxial grown films are discussed.

In chapter 4, results on microstructure and characterization of $Mg_xZn_{1-x}O$ alloy thin films grown on $LaAlO_3$ (LAO) (100), MgO (100), MgO (111) and Al_2O_3 (0001) substrates are investigated respectively. Microstructure and surface morphology are observed by XRD, AFM, SEM and HRTEM techniques. Optical spectra in infrared and UV to visible regime are carried out with FTIR and UV-Vis transmittance spectrum system. Resistivity against temperature relationship is obtained by four-point and two-point electrode methods.

Chapter 5 mainly focuses on the fabrication and characterization of p-$Li_{0.15}Ni_{0.85}O$/n-Nb-STO, p-$Li_{0.15}Ni_{0.85}O$/n-ZnO and p-$Li_{0.15}Ni_{0.85}O$/n-In-$Mg_xZn_{1-x}O$ junctions. Firstly, deposition of single $Li_{0.15}Ni_{0.85}O$ and In-$Mg_{0.5}Zn_{0.5}O$ layers are described. Bi-layed junctions are then followed. The characteristics and performance of these junctions have been investigated and all the results are furnished in this chapter.

A summary of the important results and achievements attained in the present investigation are emphasized and concluded in the last chapter of this thesis. As we have demonstrated in our work of the successes of PLD deposition of cubic $Mg_xZn_{1-x}O$ films and all transparent oxide p-n junctions, further research and development are suggested. The values of the present project are also summarized.

CHPATER 2

EXPERIMENTAL TECHNIQUES AND CHARACTERIZATION METHODS

2.1 Pulsed Laser Deposition setup

PLD uses a high power laser as the external energy source to vaporize the target materials. By simply rastering the laser spot over the target surface, the laser radiation will be absorbed by the target materials. The electromagnetic energy is converted to electronic excitation and then to thermal, chemical, and even mechanical energy to cause evaporation, ablation, excitation, plasma formation, and exfoliation. Evaporants from the target form a luminous "plume" consisting of a mixture of energetic species of atoms, molecules, electrons, ions, clusters, micro-sized solid particulates, and molten globules. The "plume" is highly directional and rapidly expands into the vacuum from the target surface to form a nozzle jet with hydrodynamic flow characteristics. They will finally condensed on the collector and then undergo thermal and non-thermal interaction with the substrate.

2.1.1 Excimer Laser

Laser wavelengths used in PLD are always lies within a range from 200nm to 400nm. At this spectral region, the materials for deposition of thin films exhibit strong absorption and the interaction between the target and the laser beam is primarily non-thermal interaction. In this project, a KrF excimer laser emitting radiation of 248nm wavelength was used. Excimer laser is a gas discharge laser that emits radiation directly in the UV region and delivers high output in excess of 1J/pulse. Excimer is a diatomic molecule that exists in an electronically excited state. The upper state of the excimer is formed by a chemical reaction, form its constituents after one of them or both have been electrically excited or ionized in a fast high voltage discharge. The excimer can undergo laser transitions from its upper state to its repulsive or rapidly discharging ground state. Due to the high ratio of upper state lifetime to lower state lifetime, population inversion and high gain can be achieved very easy in excimer laser.

2.1.2 Optics

The optical elements that couple the energy from the laser to the target are lens, apertures, mirrors, beam splitter, and laser window. Between the laser and the deposition chamber, optical elements are placed in order to steer and focus the beam. The laser beam enters the deposition chamber through the laser window. For both the lenses and laser windows, they must be made out of laser-quality optical material. It is observed that the transmittance of fused silica at wavelength of 248nm is well above 90%. So fused silica is the suitable material for KrF excimer laser.

2.1.3 Vacuum System and chamber

A PLD deposition system is comprised of the following elements: stainless steel vacuum chamber, target manipulation, substrate holder and/or heater, pump, gas flow, and vacuum gauging. In addition to the standard ports required on all vacuum chambers (e.g., pumping port, gas inlet, pressure gauging, and viewports), the PLD chamber must have ports for the rotating targets, substrates, and laser beam.

In our research, thin films were made in a chamber, which is connected to a rotary pump and diffusion pump to a base pressure of 8×10^{-6}Torr. Pressure of the chamber was monitored by ionization gauge (ULVAC 122A). When we fabricated oxide thin films, a vacuum condition (~100mTorr) will be needed and only the rotary pump was used to create the desired base ambient (~1mTorr). Ablation targets of about 20mm diameter were affixed, via a target mount, onto the tip of a rotation axle with 5 RPM rotating speed. The laser beam was directed to irradiate the flat surface of the rotating target at an angle of 45°. Laser pulse of energy of 250mJ was focused to a spot size such that energy density is maintained at about $6\mathrm{Jcm}^{-2}$. The substrates were adhered to the front of the substrate holder/heater placed at 5cm away the target.

Growth of crystalline films requires careful control of the substrate temperature during film deposition. We used a homemade 4cm diameter substrate holder which provides stable temperature that can vary from room temperature to 800°C. It utilizes halogen quartz lamps (150W maximum output) enclosed in a cylindrical shaped stainless steel case as the heating element. The temperature of the substrate holder is determined by a type K thermocouple (Nickle-Chromium, Nickel-Aluminum). Heating rate is controlled by a programmable regulator (PAC 15-0321E). The substrate is mounted on the faceplate of substrate holder with high temperature silver paste (G3691).

The high thermal conductivity of silver paste can provide a uniform temperature distribution in the substrate and ensure the substrate temperature to be as close to the measured value by the thermocouple as possible.

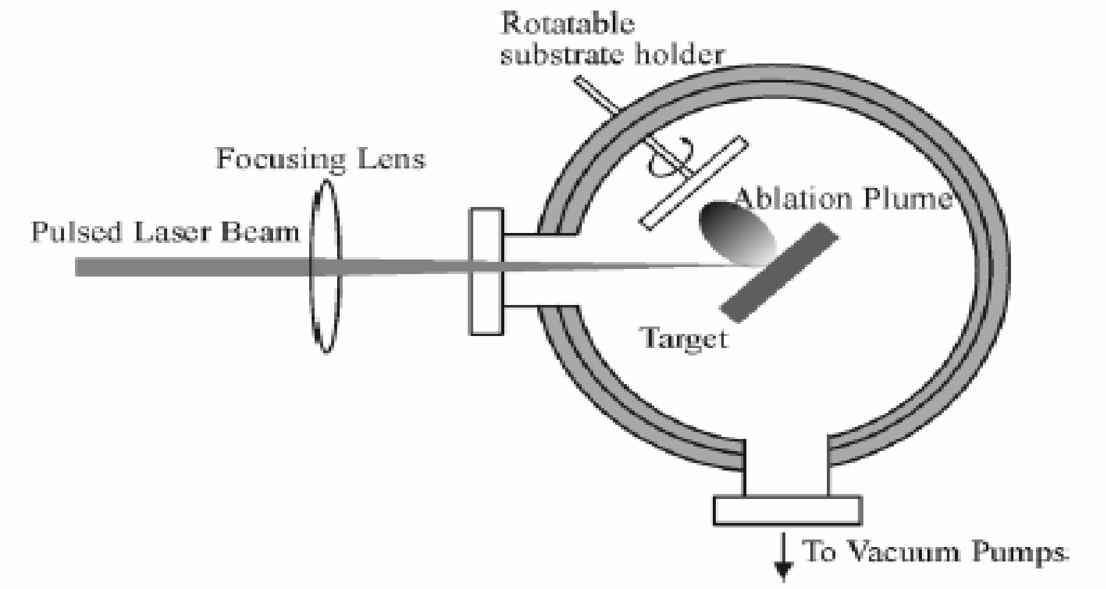

Figure 2.1 Schematic diagram of Pulsed Laser Deposition setup.

2.1.4 Target arrangements in PLD

Several different target arrangements are used in our PLD setup. The most common one is depicted in Figure 2.1. Excimer laser is focused on the surface of the target which is rotated during the deposition process. This setup is most simple and direct to fabricate single layer on a single substrate. Another arrangement is the rotating multiple-target holder configuration, which is used for in situ deposition of multilayer thin films of different materials. The excimer laser is irradiated on the rim of the rotating targets. In situ multi-layer fabrication could be achieved by sliding up and down the shaft for target selection without breaking the vaccum. The last one is a split-target arrangement, which allows to fabricate thin film of various composition ratios easily. Two half-circle of different materials are put together to form a single split target. Composition of thin film could be conveniently varied by adjusting the laser to ablate different parts of the split target using of the off-center rotation [2-1].

2.2 Experimental Procedures

2.2.1 Target fabrication

All the targets in our project were prepared by the standard solid-state reaction from high purity powders of constituent oxides. The correct composition of the powders was weighted and mixed together. They were then mixed with ethanol and grounded by ball-milling machine for 10 hours. Afterwards, they were dried and grinned to fine powder. Two calcination processes were carried out in order to get rid of the carbon component from the mixed powder and to let the chemical reaction to occur between these oxides. The calcinated powder was compressed by an oil-compressor at a pressure of 3.5 Ton into the desired pellet size. A final sintering was then carried out to form the desired target. All these calcinations and sintering processes were processed at desired temperatures in air for about 10 hours. The final targets were analyzed by a standard X-ray powder diffractometer and the chemical composition of these ceramic targets were evaluated by Energy Dispersive X-ray (EDX).

The calcinations and sintering temperatures are tabulated in the following Table 2.1. Each of the calcinations and sintering processes were done in air and lasted for 10 hours.

Table 2.1 Calcination and sintering temperature of the targets.

	ZnO	$Mg_xZn_{1-x}O$	$Li_xNi_{1-x}O$
1st Calcination Temp.	1100℃	1100℃	1100℃
2nd Calcination Temp.	1200℃	1200℃	1200℃
Sintering Temp.	1320℃	1450℃	1400℃

2.2.2 Substrate Preparation

For good epitaxial growth of our films, single crystal oxide substrates (100) oriented LAO (a=3.789Å) and MgO (a=4.24Å) were used to grow $Mg_xZn_{1-x}O$ cubic films, and Al_2O_3 (0001) and MgO (111) substrates were used to grow hexagonal $Mg_xZn_{1-x}O$ films. The lattice constants of LAO, MgO (100), MgO (111), Al_2O_3 (0001) and Nb-STO substrates used in this project and the deposited films are listed in Table 2.2. Lattice mismatch between the substrates and the films in the present work are also included. The substrates ware bought from commercial companies. The size of the substrate is 0.5cm×1cm. Due to the contamination on the surface can greatly affect the film quality, the substrates were cleaned ultrasonically in acetone for 10 minutes before use.

Table 2.2 Lattice constant values of LAO, MgO (100), MgO (111), Al_2O_3 (0001) and Nb-STO substrates and their lattice mismatch to ZnO, LNO and $Mg_xZn_{1-x}O$ films.

Substrate	Lattice constant (nm)	Lattice mismatch to ZnO(a=0.325,c=0.521nm)	Lattice mismatch to LiNiO(0.416nm)	Lattice mismatch to $Mg_xZn_{1-x}O$(~0.423nm)
$LaAlO_3$(001)	0.379		9%	10%
MgO(001)	0.421		1%	0.5%
Al_2O_3(0001)	a=0.476,c=1.299	31%	19%	20%
MgO(111)	0.595	9% for 2 ZnO match with 1 MgO	1%	0.5%
Nb-STO	0.390		6%	8%

2.2.3 Deposition Process

All the films were deposited by PLD method. The targets were mounted on the rotating target holder. The films can be fabricated under different oxygen ambient pressure by filling a suitable amount of oxygen into the vacuum chamber.

2.3 Characterization methods

In our study, the deposited films have been characterized using several techniques to yield information on their structural and electrical properties. The crystalline structures of the deposited films were examined by X-ray diffractometer (XRD) using CuK$_\alpha$ radiation. Surface morphology of films was studied by Atomic Force Microscopy (AFM). The electrical properties were measured by a high input impedance digital electrometer. The film thickness was determined by a surface profiler machine (Alpha step profiler- Tencor Instrument, model P-10)

2.3.1 Surface profiling

The thickness of our PLD films was determined from the surface profiler machine. Schematic picture is shown in Figure 2.2. The profiler is composed of electromagnetical sensor that detected the mechanical movement of a stylus as it traces the topography of a film-substrate step-an operation similar to phonograph needle on the track of a record. The vertical stylus movement is digitized and data can be processed to magnify areas of interest and yield best-profile fits. A step was made by partial masking of the substrate during the deposition process. Film thickness was directly read out as the height of the resulting step-contour trace. A precise measurement of film thickness can be determined because the vertically height resolution of the alpha step profiler can be as small as 1nm. However, it should be noted that the accuracy of the profiler measurement may suffer due to:

1. stylus penetration and scratching of soft films
2. excessive noise generated from the surface roughness
3. vibration of the equipment

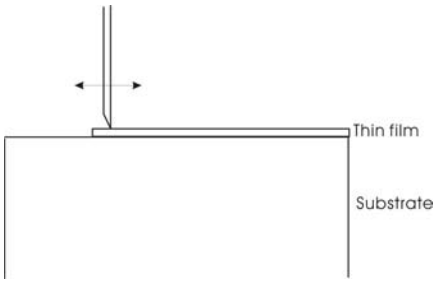

Figure 2.2 Film thickness measurement by alpha step profiler.

2.3.2 X-ray diffractometry (XRD)

XRD is a non-destructive method for determining the information about crystal structure and atom location of bulk targets, powders or thin films. In this project, the crystalline qualities of the targets and films were characterized by X-ray diffractometer (Philip X'pert system) operating in four-circle mode. The CuK$_\alpha$ radiation with a wavelength of 1.54Å was used. The radiation from CuK$_\beta$ line was filtered out by a Ni filter.

X-rays have high energies and short wavelength. When a beam of x-rays impinged on a solid material, a portion of the beam would be scattered in all directions by the electrons. Also, the crystalline solid consists of a regular array of atoms, it may form a natural three-dimension "diffraction grating" for x-rays. So, the atomic arrangements in the crystal could be deduced by x-ray diffraction.

When a parallel monochromatic beam of x-rays is incident on the testing film, some of the rays will be reflected from the plane but some will be absorbed or scattered. If this collimated beam of continuous distributed x-rays was allowed to fall on a crystal, the atoms in the crystal became diffraction centers and constructive interference in certain direction would be formed.

In order to produce the diffraction pattern, the wavelength and the interplanar spacing of the diffracted rays must satisfy the Bragg's Law:

$$\mathbf{n\lambda = 2d_{hkl}\sin\theta}$$

where d is the interplanar spacing. Since non-constructive interference will give a very low–intensity diffracted beam, thus Bragg's Law just applied to constructive interference only.

For crystal structures having cubic symmetry, $d_{hkl} = \dfrac{a_0}{(h^2+k^2+l^2)^{1/2}}$, in which a_0 is the lattice parameter (unit cell edge length).

Figure 2.3 shows the three rotating axes of the sample. CuK$_\alpha$ radiation (1.54Å) was used. The 2θ-θ scan can be used to determine the crystalline phases of the grown films. It allows us to observe the lattice planes of the thin films grown with the direction of the substrate surface.

For the ω scan, which is carried out by fixing the 2θ value of the selected peak and the angle θ is scanned for a few degree, allows us to know the degree of out-of-plane orientation of the thin film fabricated. The value of the Full Width Half Maximum (FWHM) reflects the degree of the orientation of the thin films. The smaller of the FWHM, the higher the degree of the orientation. Generally, a FWHM of $\sim 1^o$ is considered to be good oriented film and if it is $\leq 1^o$, it can be said as highly oriented films.

For the 2θ-θ scan, it only reveals the out-of-plane parameter of the film. In order to characterize the epitaxy of the film, the in-plane structure of the film should also be determined. ϕ scan is used to characterize the in-plane mosaicity of the film. By titling the ϕ angle to a suitable value and fixing the 2θ and θ angles corresponding to the selected plane (for example, in the (110) family of plane of the substrate or film of cubic structure, the psi angle should be titled to 45^o), a 360°-ϕ scan can yield in-plane alignment of the film with respect to the substrate. In the case of $Mg_xZn_{1-x}O$ and LiNiO, both being cubic structure, their ϕ scan will display four fold symmetry. Therefore, we will see four peaks with each peak being separated by 90^o. If the four peaks of the film were at the same ϕ angles as that of the substrate, we then say that the film was cube-on-cube epitaxially grown on the substrate.

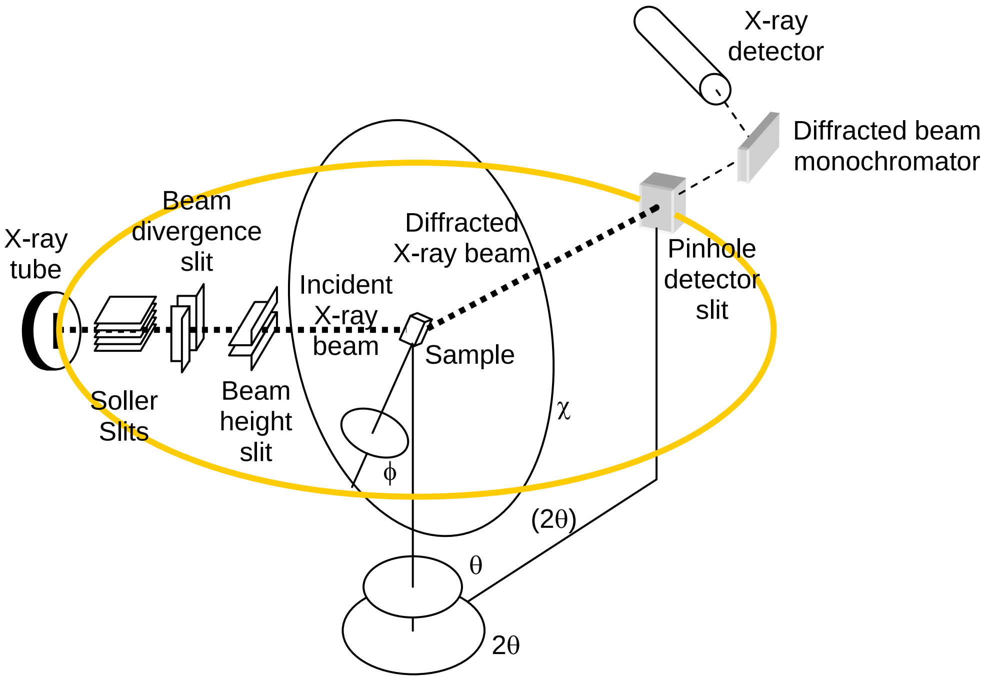

Figure 2.3 Experimental geometry, showing four primary axes of goniometer, X-ray tube, detector and slits.

2.3.3 Atomic Force Microscopy (AFM)

AFM consists of scanning a sharp tip on the end of a flexible cantilever, across a sample surface who maintaining a small and consistent force. The tips typically have an end radius of a few nm depending on tip type. The scanning motion is conducted by piezoelectric scanner which scans the tip in a raster pattern with respect to the sample (or scans to the sample with respect to the tip). The tip-sample interaction is monitored by reflecting a laser off the back of the cantilever into a split photodiode detector. By detecting the difference in the photodiode detector output voltage, changes in the cantilever deflection or oscillation amplitude are determined. Usually, AFM has three imaging modes: contact mode, noncontact mode and tapping mode.

By using AFM, the surface morphology and crystal size of thin films can be revealed. We use this AFM to investigate the problems and control of particulates under different compositions of films.

2.3.4 Scanning Electron Microscopy (SEM) and Energy-Dispersive X-ray spectrometer (EDX)

SEM can image and analyse bulk specimens. We used a Field Emission Scanning Electron Microscope (FESEM) - JEOL JSM-6335F and a Leica stereoscan 440 to obtain sample surface morphology and the cross-section images. For FESEM, a field-emission cathode in the electron gun of a scanning electron microscope provides narrower probing beams at low as well as at high electron energy than those found in conventional SEM. Consequently it provides both improved spatial resolution and minimized sample charging and damage. In addition, FESEM can probe closer to the immediate material surface due to reduced penetration of low kinetic energy electrons. In SEM, electrons from a thermionic, Schottky or field-emission cathode are accelerated through a voltage difference between cathode and anode that may be as low as 0.1KeV or as high as 50KeV. The smallest beam cross-section at the gun with a diameter of the order about 10-50μm for thermionic emission or the virtual source with a diameter of 10-100nm for Schottky or field-emission guns, is demagnified by a two-or three-stage electron lens system, so that an electron probe of diameter 1-10nm carrying an electron-probe current of 10^{-9}-10^{-12}A is formed at the specimen surface. The interactions with the electron beam and the specimen surface cause several types of energetic emissions, including backscattered electrons, secondary electrons, Auger electrons (a special form of secondary electron), continuous X-rays and characteristics X-rays that are emitted from the area of the specimen where the electron beam is impinging. The induced signals are detected by the detector. The signals from the detector are then amplified by circuitry and synchronized with the scan generator to produce a SEM image, which comes from the secondary and backscattered electrons. Phases within a material are distinguished by the backscattered electrons.

The SEM specimens require being conductive. Inconductive specimen will build up negative charge on its surface and will deflect the incident electron beam and ruin the image, therefore inconductive specimens should be coated with a conductive layer such as Au, Pt or carbon with thickness about 10 to 20nm. This will help to increase secondary and backscattered electron emissions, to reduce thermal damages and to eliminate surface charging, leading to a relatively shaper SEM image.

EDX system is often installed in the SEM equipment to identify the type and the amount of element species in the specimens. Each X-ray quantum releases its entire energy (unlike electron which releases only part of its total energy upon each of its interactions) by generating photoelectron. Each photoelectron generated therefore can have extremely high kinetic energy (up to several tens of KeV) and upon further inelastic collisions generate many more electron-hole pairs. Therefore the current collected in the biased circuit is proportional to the X-ray quantum energy. By using multi-channel analyser, characteristic X-ray spectra are obtained. Cross-reference with the data bank thus allows identification of the elements. Also the spectral peak intensity gives quantitative measurement of the amount of the element. EDX provides a quick overview of the elements present in the specimen but with poor resolution and it is not applicable for element with atomic number below 11[2-5].

2.3.5 Transmission Electron Microscopy (TEM)

In our project, we used JEOL JEM-2010 Electron microscope to observe the crystal structrue and epitaxial relationship of films. The TEM specimens were prepared by using the focused-ion-beam (Gatan Model 691 Precision ion polishing system) etching techniques.

In contrast to the SEM, in which the electrons probe bulk specimens, the transmission electron microscope makes use to high-energy electrons to irradiate thin specimens of around 0.1μm or less in thickness. The electrons are transmitted and form an image of the specimen magnified in several steps with the aid of electron-optical lenses. The entire image can be observed directly on a fluorescent screen and is not built up line by line on a CRT as in the SEM. In the TEM, the electrons emitted from the electron gun are accelerated to energy of 100KeV. The condenser lens then shapes them to an approximately parallel beam which illuminates the specimen uniformly. The objective lens produces a first image, which is then further magnified by the intermediate and projector lenses and finally projected onto the fluorescent screen. If a film is inserted into the beam path instead of the fluorescent screen, the image can be recorded by exposing the photographic emulsion.

The image contrast is generated in the following way: the incident electrons are elastically scattered or diffracted in the specimen by small angles. In most cases, only those electrons which penetrate the specimen without scatterings (directly transmitted beam) are used for image formation. To allow this, an adjustable aperture is inserted into the back focal plane of the objective lens. The objective aperture limits the scattering angle of the electrons scattered at the specimen to the order of 1 mrad and allows essentially only the direct beam to pass through. An image produced in this way is therefore called the bright-field image in analogy to light optics. Since the scattered or diffracted electrons are excluded from this image, any changes in the intensity of the transmitted beam due to inhomogeneities in the specimen with respect to, e.g., density, thickness, and orientation, create an image contrast.

Provision of thin specimens with a thickness in the region of 0.1μm requires suitable specimen preparation techniques which are significantly more complex than those of SEM specimens. Compared with the SEM, however, the TEM offers a higher resolution which extends down to atomic dimensions. Beyond this, the transmission of thin specimens yields a wealth of information about the material structure, such as grain size, crystal defects etc.

2.3.6 Fourier Transform Infrared Spectroscopy (FTIR)

Infrared spectroscopy is concerned with vibrational and rotational energy changes of the molecule in sample. It provides a completely different approach to record the optical spectra in the infrared regime. This spectrometer uses a beam splitter, one fixed mirror and one moving mirror to achieve same function as the conventional dispersive spectrometer. In essence FTIR spectrum is obtained by recording the interferograms with and without a sample in the beam. Transforming the interferograms into spectra of the source with sample absorptions and the source without sample absorptions are done via computer software. The ratio of the former to the latter therefore corresponds to a double beam dispersive spectrum. The method of FTIR overcomes the disadvantage of the measurement of one resolution element at a time and the disadvantage of the energy entering and leaving the monochromator being limited by narrow slits.

Quantitative analysis by means of infrared absorption spectroscopy is based on the use of Beer's law [2-6]:

$$\mathrm{A}=\log\frac{1}{T}=\mathrm{abc}$$

Where A is absorbance, T transmittance, a absorptivity, b sample thickness, and c sample concentration.

$$\text{Transmittance}=\frac{Transmitted\quad radiation\quad intensity}{Incident\quad radiation\quad intensity}=\frac{I}{I_0}$$

2.3.7 Transmittance

Transmittance of the films were measured by a UV-2100PC UV-VIS Scanning Spectrophotometer by SHIMADZU company. This spectrophotometer has a broad light source wavelength from 200nm to 900nm. The transmittance against wavelength profile can give clear information on the bandgap energy of the materials. The band gap energy and the tansition mechanism could be deduced by a profile of $\alpha h\nu^n$ against hν, where α is absorption coefficient and n is dependent on the transition mechanism. α can be expressed as $\alpha = (\ln 1/T)/d$, where T is the transmittance and d is the thickness of the films. The material is said to possess indirect band gap if n=0.5, and direct band gap if n=2.

2.3.8 X-ray Photoelectron Spectroscopy (XPS)

A Physical Electronics 5600 multi-technique system was used to record element compositions and chemical states in the $Mg_xZn_{1-x}O$ series films.

Surface analysis involves a group of techniques used to investigate the elemental composition and chemical states (status of bonding) between atoms at the surface of a solid. X-ray photoelectron spectroscopy, which is also known as electron spectroscopy for chemical analysis (ESCA), is probably the most widely used surface analysis technique [2-7]. In an XPS analysis experiment, the sample is irradiated by a x-ray beam. The x-ray beam excites photoelectrons from the atoms at the surface of a solid.

When a x-ray photon hits the core electron of an atom, the electron is knocked out if the photon energy is high enough. The following relationship holds:

$$h\nu=E_k+E_b,$$

where hν is the incident x-ray photon energy, E_k is the kinetic energy of the emitted electron as measured by an electron energy analyzer, and E_b is binding energy of the electron to the atom. By measuring the energy of the emitted electron, the composition of elements and chemical states of the sample are determined because elements have unique electron binding energies. XPS is thus able to detect all elements except hydrogen.

In addition, in conjunction with ion beam sputtering, composition at deeper depths can also be obtained (depth profiling) since the photoelectrons can only escape from a region near the surface. XPS is also a quantitative technique. The XPS peak intensities after normalized by the sensitivity factors can be used to calculate the surface chemical composition.

2.3.9 Current-Voltage measurement (I-V)

An electrometer of Keithley 6517A Electrometer/ High resistance meter is used to measure the current-voltage characteristics of the rectifying properties of p-n junctions. Ohmic contacts are made on each side of the junction. To increase the precision and reproducibility of the measurement, four contacts are often used in a linear configuration. The inner ones are current sensors; the outer ones are voltage-input sensors. The lowest current limit and upper current limit are 20pA and 10mA, respectively. Typical current flowing through the fabricated p-n junctions ranged from several hundred nano- A to several milli- A. For a conventional semiconductor diode I-V characteristic, four regions are included: linear region, exponential region, leakage current region and breakdown region.

2.3.10 Resistivity-Temperature measurement (R-T)

The Resistivity against Temperature measurement was taken by two-point probe method by placing two electrodes on the surface of the sample. Potential difference was applied between the two electrodes and the resulting current was measured. The temperature range can be from 77K to 500K. From the R-T relation, we could deduce the conduction mechanism of the films at room temperature as well.

The sample together with the probe heads were mounted in a cryostat. After pouring liquid nitrogen into the cryostat and reaching 77K, the sample temperature was programmed with a digital temperature controller. Resistance against temperature data was taken on warming to 500K by an automated data acquisition system. The resistivity ρ in a unit of Ωcm, was calculated by the relation $\rho=Rlt/d$, where R is the measured resistance, l is the length of electrode, t is the film thickness and d is the two point distance. The conductivity $\sigma = 1/\rho$.

CHAPTER 3

PREPARATION OF $Mg_xZn_{1-x}O$ TARGETS AND ALLOY THIN FILMS

3.1 Introduction

In this project $Mg_xZn_{1-x}O$ (MZO) ceramic materials with x=0 to x=1 were fabricated. All the bulk $Mg_xZn_{1-x}O$ were made into a disc form by standard solid-state reaction from high purity powders of constituent oxides. They were used as the ablation targets for all the PLD experiments.

3.2 Preparation of $Mg_xZn_{1-x}O$ targets

The preparation of single-phase MZO ceramics was achieved by conventional solid-state reaction. Proper amount of magnesium oxide (MgO, 98% purity) and Zinc oxide (ZnO, 99.95% purity) were weighted and mixed by ball milling machine in ethanol with zirconia media for more than 6 hours. The milling time should continue long enough for complete milling because it is an important procedure in order to obtain the homogeneous solid solution. Table 3.1 shows the required chemicals and their appropriate desired weight to fabricate $Mg_xZn_{1-x}O$, $Li_{0.15}Ni_{0.85}O$ and 8at.% In_2O_3 doping $Mg_{0.5}Zn_{0.5}O$ targets needed to deposit films and p-n junction described in chapter 4 and chapter 5.

Table 3.1 Required chemicals and weight.

	ZnO	MgO	Li_2CO_3	NiO	In_2O_3
molecular weight(g)	81.4	40.3	73.9	74.7	277.63
$Mg_{0.9}Zn_{0.1}O$ desired weight (g)	2.442	10.881			
$Mg_{0.7}Zn_{0.3}O$ desired weight (g)	4.884	5.642			
$Mg_{0.5}Zn_{0.5}O$ desired weight (g)	6.512	3.224			
$Mg_{0.4}Zn_{0.6}O$ desired weight (g)	9.768	3.224			
$Mg_{0.2}Zn_{0.8}O$ desired weight (g)	13.024	1.612			
ZnO desired weight (g)	10				
$Li_{0.15}Ni_{0.85}O$ desired weight (g)			0.831	9.524	
8at%In_2O_3-$Mg_{0.5}Zn_{0.5}O$ desired weight (g)	5.349	2.648			3.173

The mixed powders after milling were then dried in ohmic furnace with temperature set at 100°C to remove ethanol and volatile organic contents. The dried powders were grinded by hand using agate mortar and pestle to fine powders again. They were subsequently calcinated for two times in a covered alumina crucible for about 10 hours in a carbolite furnace in order to get rid of the carbon component from the mixed powder and to let the chemical reaction to occur. Calcination is a solid-state reaction that different material components are reacted to form a new phase material. Hand-grinding is a necessary procedure after each calcination process.

The calcinated powder was then placed inside a steel mould and compressed by an oil-compressor at a pressure of 3.5 Ton for 10 minutes so that all the powder was uniformly and densely pressed inside the mould into the desired pellet size.

A final sintering was then carried out to form the desired laser ablation target. This step is essential to densify the ceramic by reducing or eliminating of the pores between the powder particles. When the samples were calcinated or sintered, they were placed on alumina plate and covered by alumina crucibles for protecting from ambient atmosphere. Time should be set long enough to allow for the completion of reaction and grain growth.

The calcinations and sintering temperatures are tabulated in Table 3.2. Each of the calcinations and sintering processes were done in air and lasted for 10 hours. Detailed temperature-time schedule of processing procedures is shown in Figure 3.1.

Table 3.2 Calcination and sintering temperature of the targets.

	ZnO	$Mg_xZn_{1-x}O$	$Li_{0.15}Ni_{0.85}O$	In-$Mg_{0.5}Zn_{0.5}O$
1st Calcination Temp.	1100℃	1100℃	1100℃	
2nd Calcination Temp.	1200℃	1200℃	1200℃	1100℃
Sintering Temp.	1320℃	1450℃	1400℃	1350℃

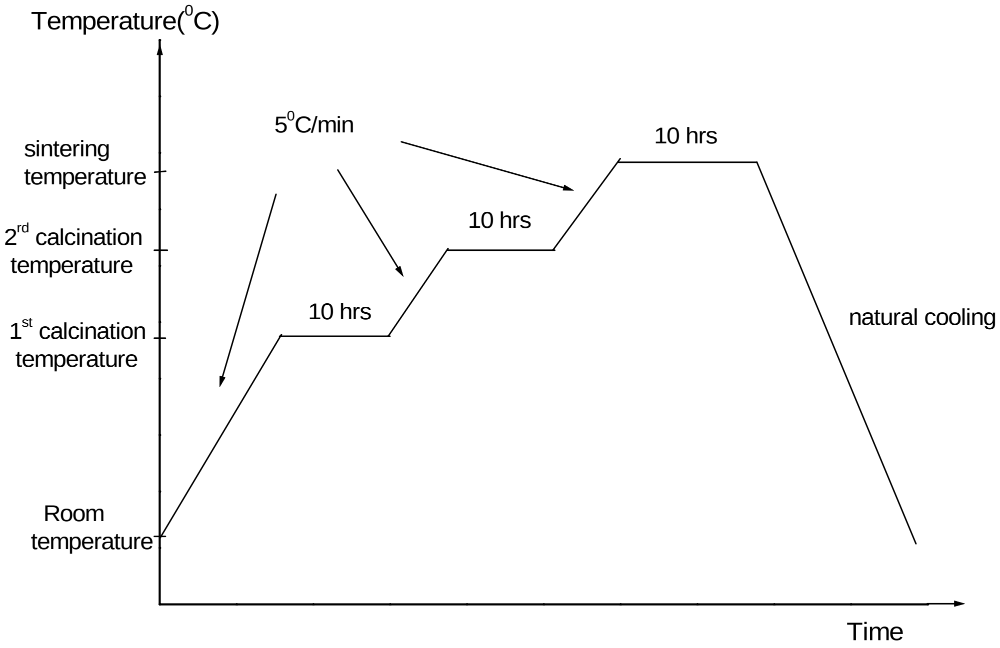

Figure 3.1 The temperature-time schedule of each calcination and sintering process of ceramics targets.

3.3 XRD studies of structural characteristics and EDX analysis of $Mg_xZn_{1-x}O$ targets

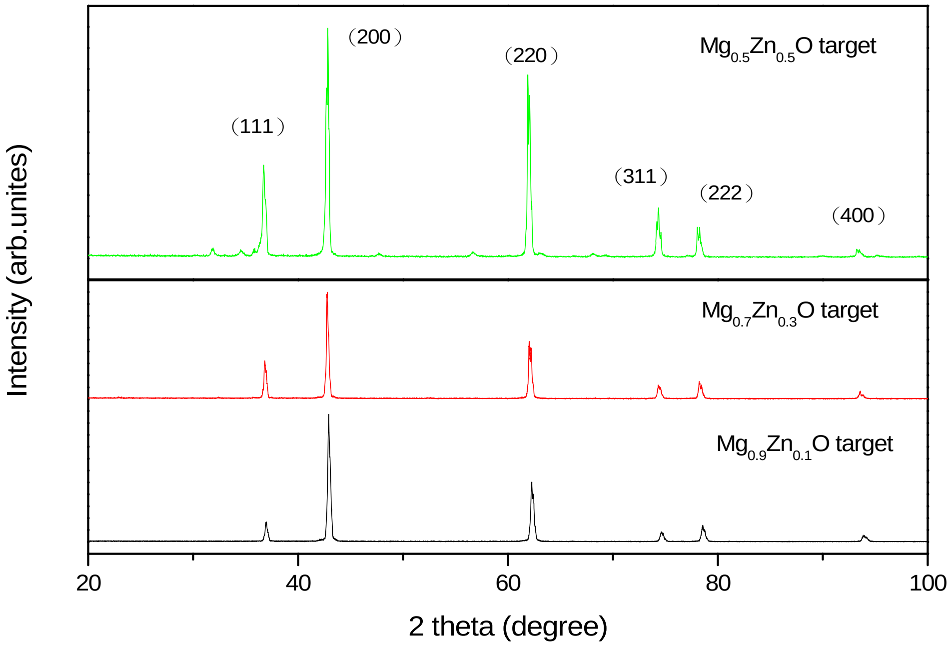

Figure 3.2 XRD patterns of the air-sintered targets from the mixture of stoichiometrical $Mg_{0.9}Zn_{0.1}O$, $Mg_{0.7}Zn_{0.3}O$ and $Mg_{0.5}Zn_{0.5}O$ compositions.

The final targets were analyzed by a standard X-ray powder diffractometer. The XRD patterns of the air-sintered $Mg_{0.9}Zn_{0.1}O$, $Mg_{0.7}Zn_{0.3}O$ and $Mg_{0.5}Zn_{0.5}O$ targets show similar XRD patterns and are shown in Figure 3.2. All the three targets are single-phase compounds. Major sharp x-ray diffraction peaks match well with those listed in the database (International centre for Diffraction Data, ICDD). Lattice constants of the targets are calculated with 2θ values and hkl indices. They are 0.421nm, 0.422nm, and

0.423nm for $Mg_{0.9}Zn_{0.1}O$ target, $Mg_{0.7}Zn_{0.3}O$ target and $Mg_{0.5}Zn_{0.5}O$ target, respectively. We could see that the lattice constant increases with ZnO composition, in general agreement with the Vegard's law. Figure 3.3 gives an intuitionistic graph of the relationship between Mg composition x and the lattice constant of targets.

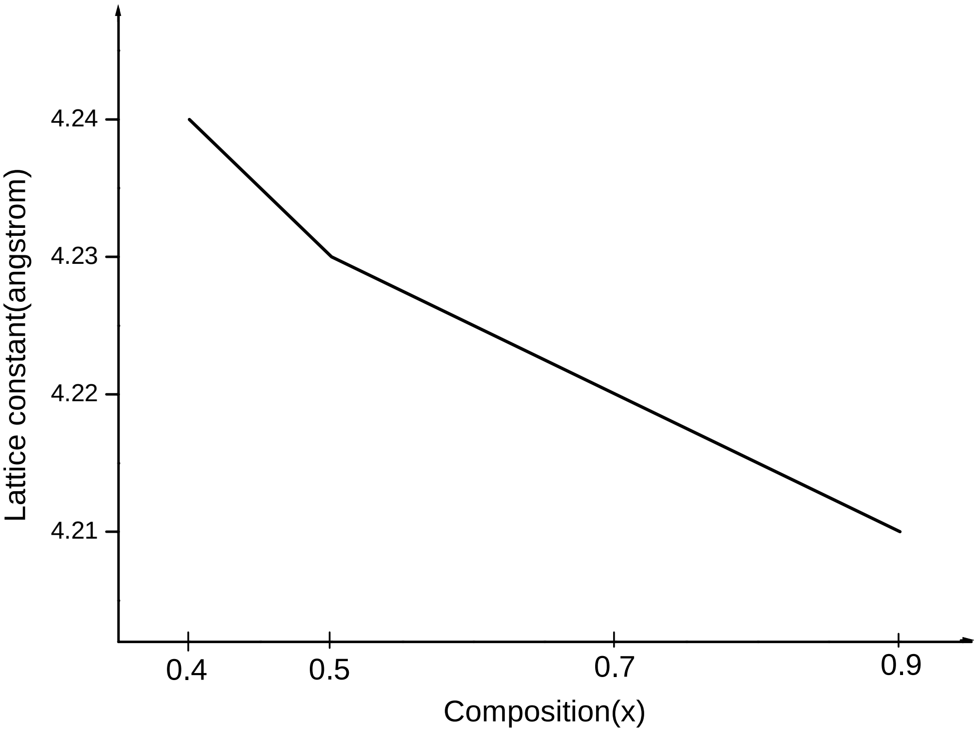

Figure 3.3 Relationship between the lattice constant values of targets and the MgO composition x.

At the same time, the θ-2θ scans of the ZnO, $Mg_{0.2}Zn_{0.8}O$ and $Mg_{0.4}Zn_{0.6}O$ targets are shown in Figure 3.4. ZnO diffraction peaks are indexed and matched well according to the database. $Mg_{0.2}Zn_{0.8}O$ target shows a similar pattern with ZnO target, indicating also a single phase material. Small amount of MgO doped into ZnO has no noticeable change in the major hexagonal crystal arrangement of the target. However the $Mg_{0.4}Zn_{0.6}O$ target used for film deposition in this study is a mixed-phase compound. This is revealed in the XRD pattern shown in Figure 3.5. Apart from reflections that could be indexed according to the hexagonal ZnO phase, some reflections from the cubic MgO phase have appeared. In the following chapters, different orientation growth of $Mg_{0.4}Zn_{0.6}O$ films on either cubic or hexagonal substrates are studied. Due to the fact that $Mg_{0.4}Zn_{0.6}O$ targets are mixed phased, it will be of interest to deposit MZO on cubic substrates so as to force the MZO to grow in pure cubic form. To our best knowledge, (100) oriented c-MZO with high content of ZnO is reported for the first time here. Indeed this c-MZO epi-layer provides templates to grow homo- or hetero-structures of ZnO related compounds, which may lead to useful devices, such as UV emitters or detectors, with performance that supersedes those offered by group-Ⅲ nitrides.

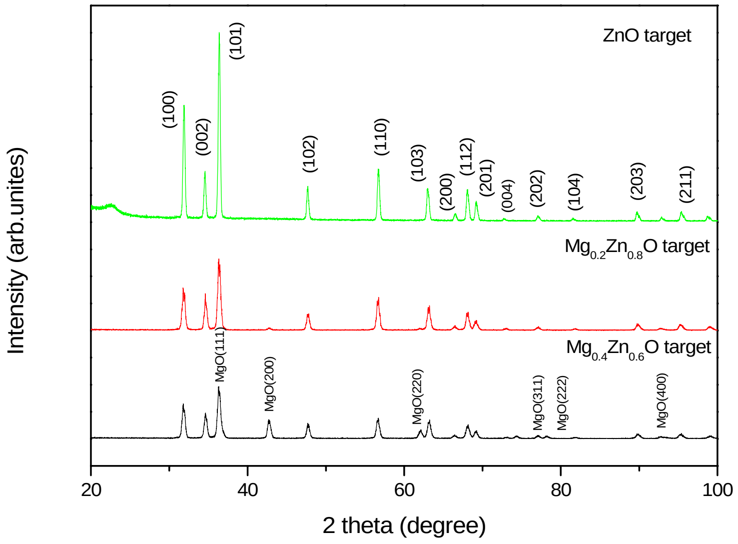

Figure 3.4 XRD patterns of the air-sintered ceramic targets from the mixture of stoichiometric $Mg_{0.4}Zn_{0.6}O$, $Mg_{0.2}Zn_{0.8}O$ and ZnO compositions.

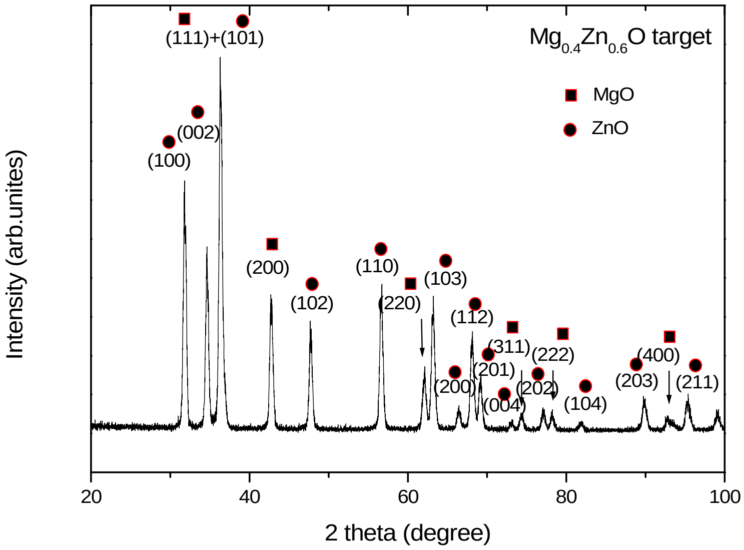

Figure 3.5 XRD pattern of the air-sintered ceramic target from the mixture of stoichiometric $Mg_{0.4}Zn_{0.6}O$ composition.

EDX test was carried out to verify the chemical compositions of the $Mg_xZn_{1-x}O$ targets. The data are shown in Table 3.3. The EDX analysis of all targets exhibits a slight MgO rich when compared with the nominated compositions. It may caused by the different melting point of MgO (2830°C) and ZnO (1975°C).

Table 3.3 EDX data of chemical compositions of $Mg_xZn_{1-x}O$ targets.

Target name	Mg atomic %	Zn atomic %
$Mg_{0.9}Zn_{0.1}O$	95.48	4.52
$Mg_{0.7}Zn_{0.3}O$	71.07	28.93
$Mg_{0.5}Zn_{0.5}O$	60.91	39.09
$Mg_{0.4}Zn_{0.6}O$	42.58	57.42
$Mg_{0.2}Zn_{0.8}O$	27.63	72.37
ZnO	0	100

3.4 Deposition of $Mg_xZn_{1-x}O$ films on LAO(100), MgO(100), MgO(111) and Al_2O_3(0001) substrates

$Mg_xZn_{1-x}O$ thin films were deposited by PLD method on different kinds of substrates using our own sintered targets. The surfaces of the substrates were ultrasonically cleaned in acetone. Then the substrate was placed on the substrate holder at about 4-5cm distance away from the target in the vacuum chamber. Good thermal contact is guaranteed by applying high temperature silver paste between the substrate and the substrate holder. The substrate temperature during growth was kept at 650°C. The chamber was evacuated to a base pressure of 2×10^{-5} Torr by a oil diffusion pump. The targets were ablated by a KrF excimer laser (Lambda Physik, Complex 205) operating at wavelength of 248nm. The average pulse energy was 250mJ. The laser was focused through a fused silica window of the vacuum chamber onto the target surface with fluence at ~5 Jcm^{-2}. The film growth rate was kept at about 10nm per min. so that the film thickness was controlled by the growth time. Using a lower laser fluence and a longer target-substrate distance are effective ways to reduce the formation of particulates on the film surface. During the deposition, oxygen pressure, pulse frequency and deposition time was maintained at $\sim3\times10^{-5}$ Torr, 10Hz and 30min, respectively. The resulted film thickness is 200-300nm. In order to improve the crystallinity of the deposited films, in-situ post-deposition annealing was generally performed for 20 minutes. Then films were naturally cooled to room temperature at the base pressure.

3.5 Optimization of deposition conditions

There are a few parameters that can be varied in PLD: the substrate temperature Ts, the ambient pressure, the target-substrate distance and the laser fluence. Among these factors, substrate temperature and ambient pressure are the most important ones in controlling of the structure and the quality of the PLD-produced films.

Substrate temperature (Ts) is crucial in the film deposition process. It influences the film's crystallinity and surface morphology because a low substrate temperature results in low surface migration of adatoms and poor crystallization. Too high a Ts, on the other hand, causes the adatoms to re-evaporate from film surface. Hence, at an appropriately set substrate temperature, the high kinetic energy of the ablated species is able to enhance the surface diffusion of the atoms. Then the mobile adatoms can move to their most stable positions, which are created by the potential field of the substrate, leading to better crystallinity. For our $Mg_xZn_{1-x}O$ thin films, 650°C is the appropriate substrate temperature to obtain excellent single crystal epitaxy films on LAO(100), MgO(100), MgO(111), and Al_2O_3(0001) substrates.

As we have mentioned before, it is necessary to immit certain amount of oxygen into the vacuum chamber for growing oxide films. During the deposition process ambient oxygen helps to maintain oxygen stoichiometry and to stabilize the desired crystal phase. However, some oxides such as rocksalt MgO and MnO and wurtzite ZnO, are stable even in an oxygen free environment. For $Mg_xZn_{1-x}O$, excellent single crystal epitaxial films could only be obtained in high vacuum condition. The crystal quality is enhanced by decreasing the ambient pressure. FWHM of the rocking curves of the films decreases with decreasing deposition pressure from 10^{-2} Torr to 10^{-5} Torr. Our PLD chamber could be evacuated to 1×10^{-5} Torr by a diffusion pump. Substrate heating normally degraded the vacuum. So all of our $Mg_xZn_{1-x}O$ films were deposited with a pressure of 2×10^{-5} Torr to 6×10^{-5} Torr.

CHAPTER 4

MICROSTRUCTURE AND CHARACTERIZATION OF $Mg_xZn_{1-x}O$ ALLOY THIN FILMS

4.1 Introduction

We deposited our $Mg_xZn_{1-x}O$ alloy thin films on four kinds of substrates, $LaAlO_3$(LAO)(100), MgO(100), MgO(111) and Al_2O_3(0001). Microstructure and surface morphology of these series of films were investigated by X-ray diffraction (XRD), atomic force microscopy (AFM), scanning electronic microscopy (SEM), transmission electron microscopy (TEM) and high resolution TEM (HRTEM). Fourier Transform Infrared Spectroscopy (FTIR) and tranmittance spectrum were carried out to investigate the absorption spectra in infrared and visible regime. Resistivity against temperature range from 150K to 350K is obtained by four-point and two-point electrode methods. And the actual film compositions of selected samples were measured by a physical Electronics 5600 multi-technique X-ray Photoelectron Spectroscopy (XPS) system. We will discuss the results by classifying them in different substrates.

4.2 Microstructure and characterization of $Mg_xZn_{1-x}O$ alloy thin films on LAO substrates

4.2.1 XRD studies of structural characteristics

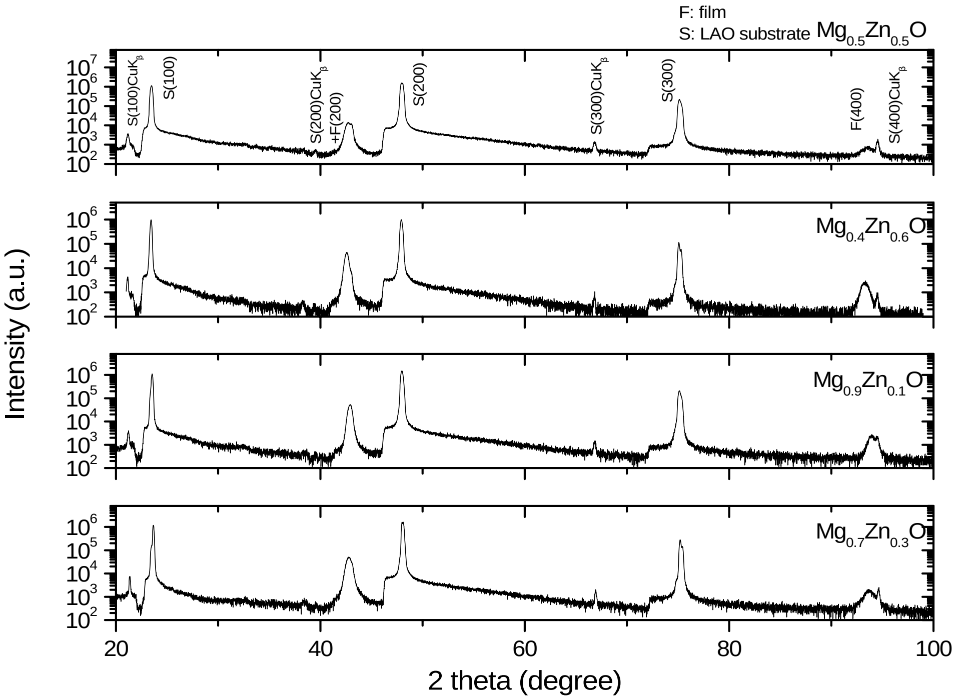

Figure 4.1 XRD 2 theta scan of $Mg_xZn_{1-x}O$/LAO(100) (x=0.4,0.5,0.7,0.9) film (pressure: 3×10^{-5} torr; temperature: 650°C).

MgO single crystal is the most appropriate and premier choice of substrates to grow epitaxy c-MZO films. However, its x-ray diffraction pattern will be exactly overlapped with that of MZO and our x-ray diffractometer is not able to resolve them. For this reason, our initial c-MZO film growth was on LAO. LAO substrate was chosen because a cubic substrate of appropriately matched lattice dimension could help to force MZO to grow in cubic form with high Zn content that is close to or even goes beyond the solubility limit. It is also expected to stabilize the high pressure cubic ZnO phase in these films. Figure 4.1 shows the XRD θ-2θ patterns of $Mg_xZn_{1-x}O$ series films deposited at 650°C on LAO (100).

All the films shown in the figure have cubic structure. Strong reflections from (200) and (400) diffraction planes were indexed according to the cubic structure. The MZO (200) planes with 2θ peak at about 42.6° coincides with the LAO substrate (200) CuK_β peak. Take a typical $Mg_{0.4}Zn_{0.6}O$ film for example, the peak at 42.6° has a full width at half maximum (FWHM) of 1.11°. This peak has an angular position that coincides with the LAO (200) CuK_β peak (FWHM equals to 0.2°, instrumentation limit for single crystal). Resolved MZO peaks occur at high order diffraction spectra.

The MZO (400) and LAO (400) CuK_β diffractions are distinctly separated and possess similar intensity, which are shown clearly in Figure 4.2 of the XRD 2 theta pattern of MZO (400) diffraction planes.

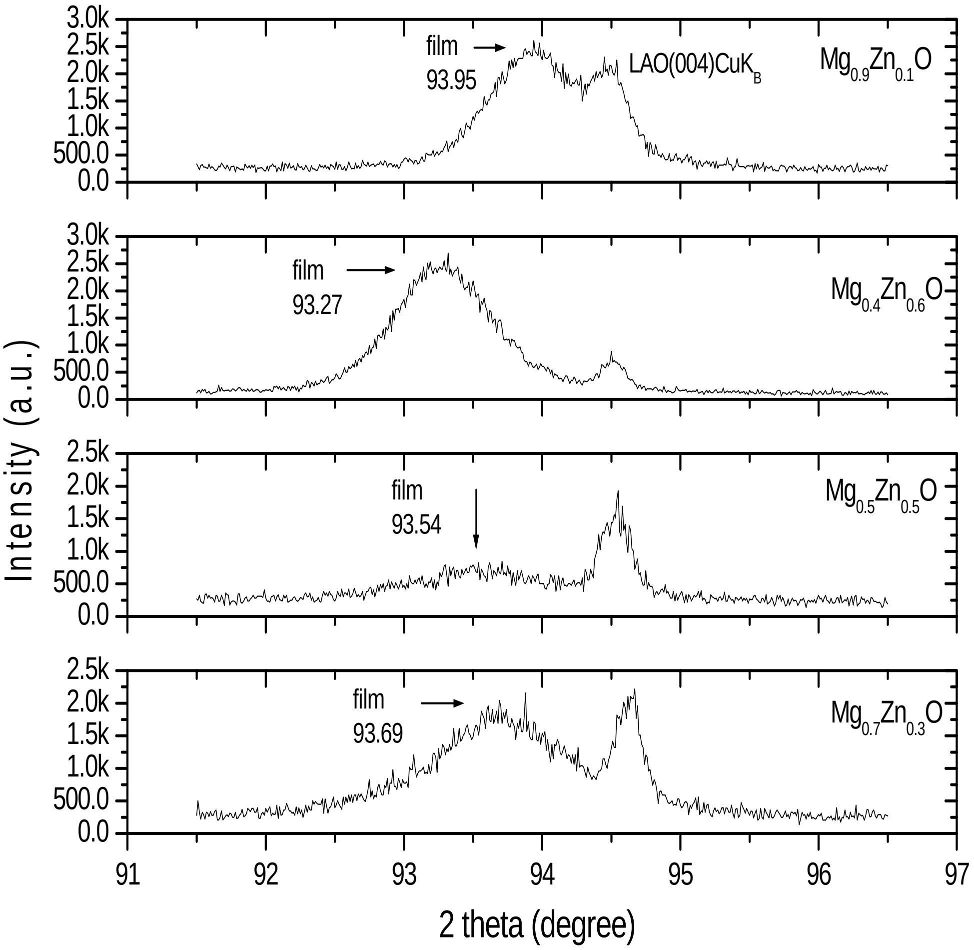

Figure 4.2 Close up view of 2 theta patterns of MZO (400) diffraction planes at near 94°.

MZO (400) planes shift to lower 2 theta angles when increasing the ZnO content. The 2 theta equal to 93.95°, 93.69°, 93.54° and 93.27° for $Mg_{0.9}Zn_{0.1}O$, $Mg_{0.7}Zn_{0.3}O$, $Mg_{0.5}Zn_{0.5}O$ and $Mg_{0.4}Zn_{0.6}O$ films, respectively. The observed difference in intensity of these MZO (400) peaks may due to the variation in crystalline quality and thickness of the films.

The series of $Mg_xZn_{1-x}O$ films (200) diffraction planes are shown in Figure 4.3. Similarly the (200) reflection shifts slightly to larger 2θ angle with increasing x, i.e. more Mg, indicating that there is a slight expansion in lattice parameter due to the substitution of larger Zn^{2+} ion. The increase in lattice parameter is small due to the similarity in the ionic radii of Mg^{2+} and Zn^{2+}. The result is comparable with the XRD patterns of our $Mg_xZn_{1-x}O$ targets and some previous reports [4-1, 4-2, and 4-3].

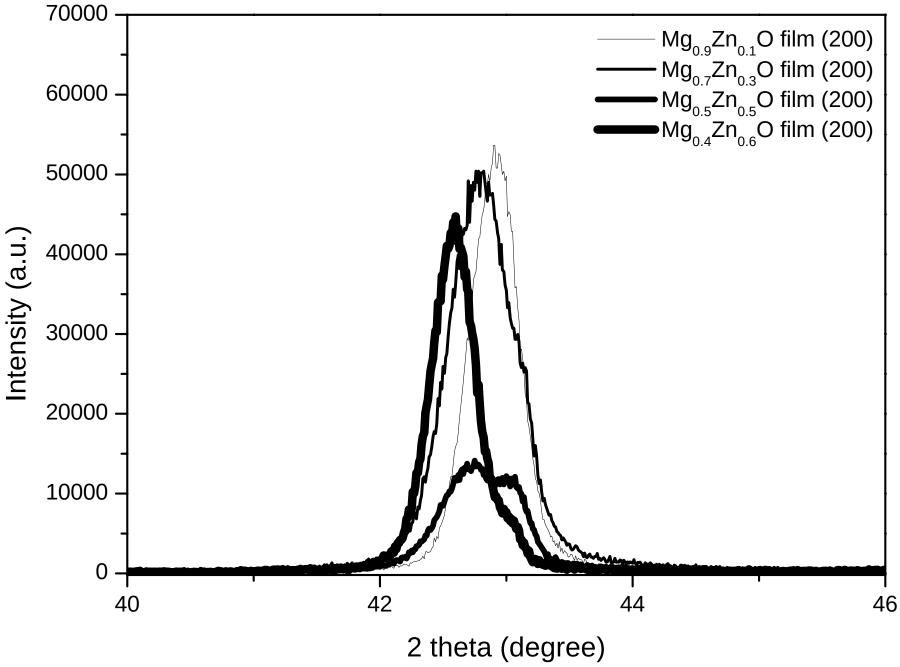

Figure 4.3 XRD 2 theta patterns of $Mg_xZn_{1-x}O$ films (200) diffraction planes.

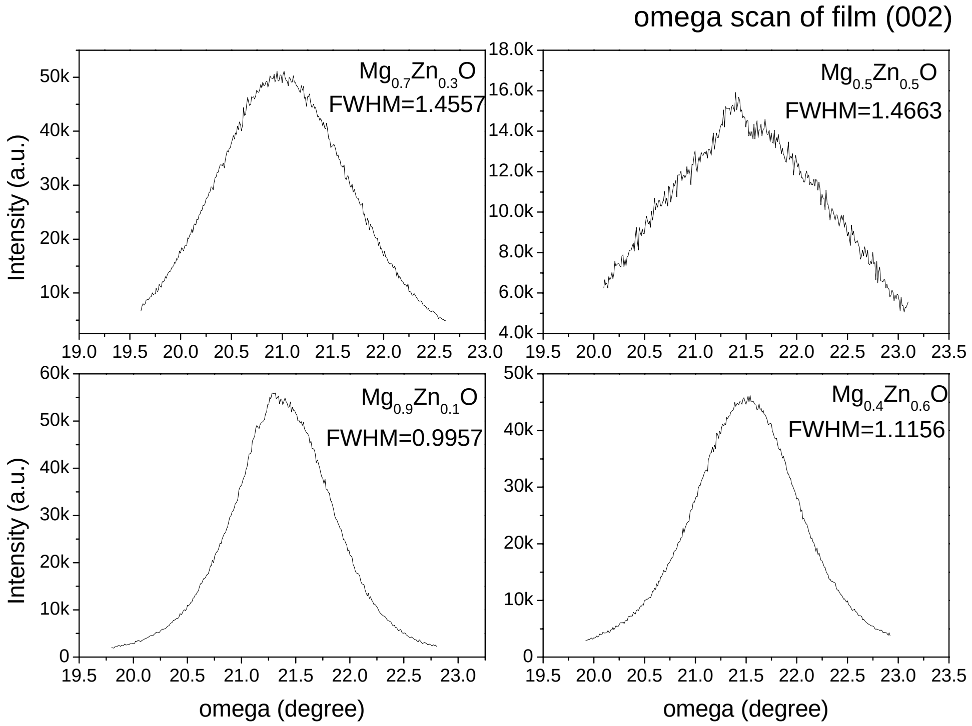

Figure 4.4 Rocking curves on the $Mg_xZn_{1-x}O$ (200) diffraction planes.

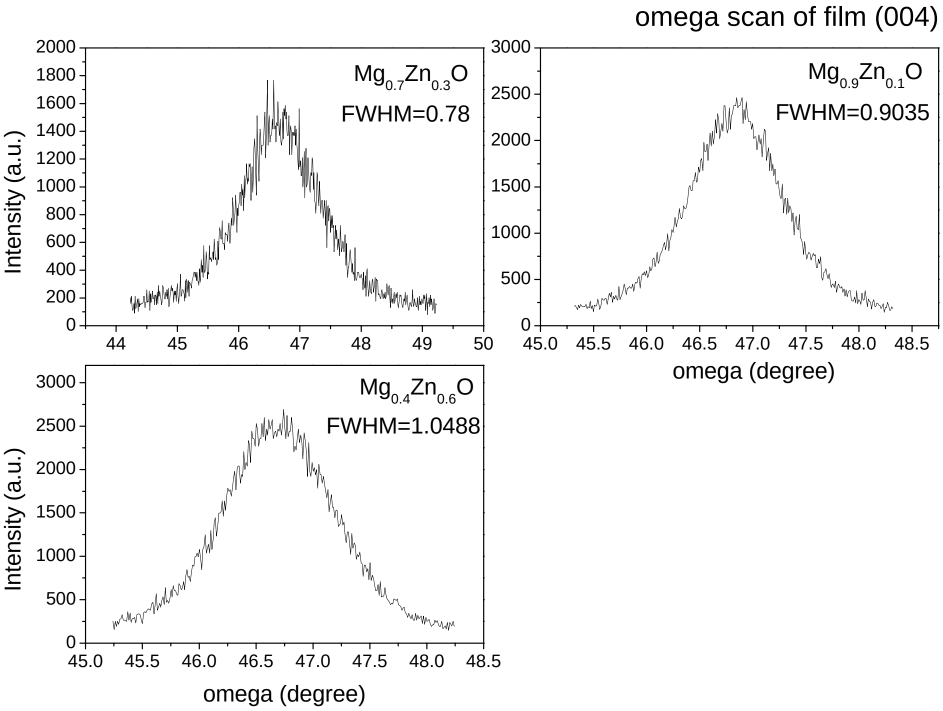

Figure 4.5 Rocking curves on the $Mg_xZn_{1-x}O$ (400) diffraction planes.

XRD ω-rocking curves on the $Mg_xZn_{1-x}O$ (200) and (400) reflections are shown in Figure 4.4 and 4.5. The corresponding FWHM of the curves are indexed, all of them are around 1°, indicating good crystal grain orientation of our MZO films.

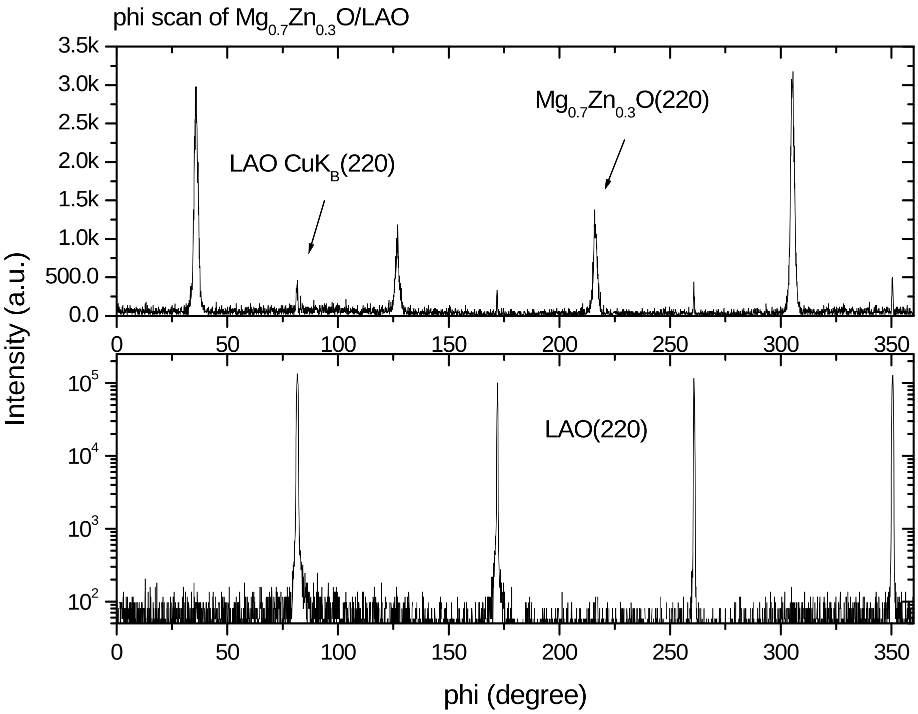

Figure 4.6 360^0-ϕ scans on $Mg_{0.7}Zn_{0.3}O$ (220) and LAO (220) reflections.

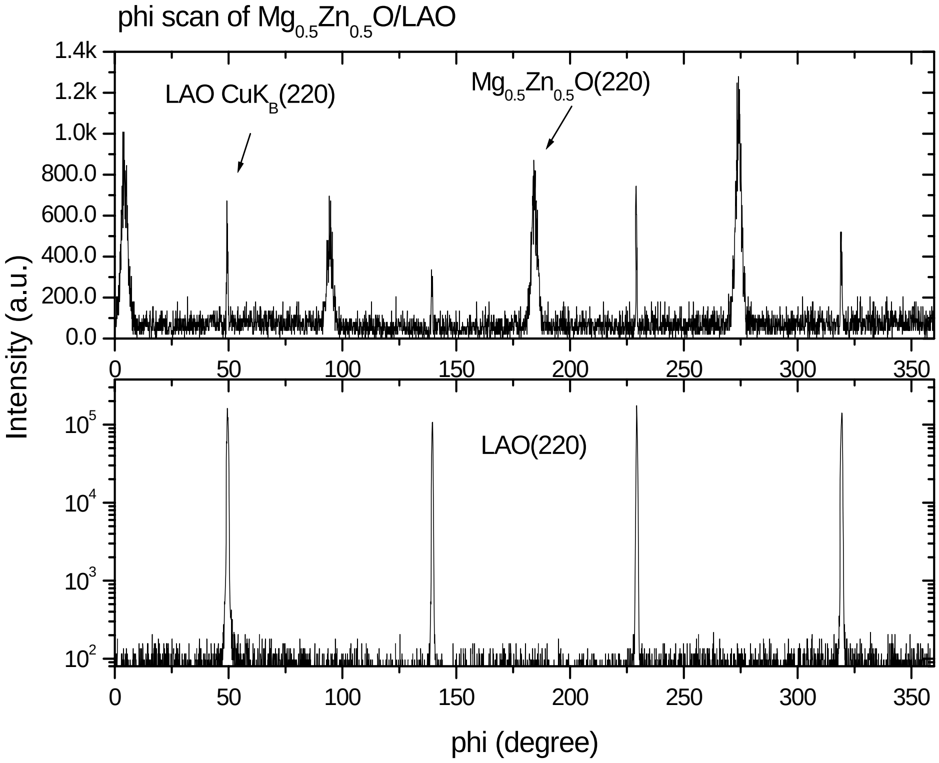

Figure 4.7 360^0-ϕ scans on $Mg_{0.5}Zn_{0.5}O$ (220) and LAO (220) reflections.

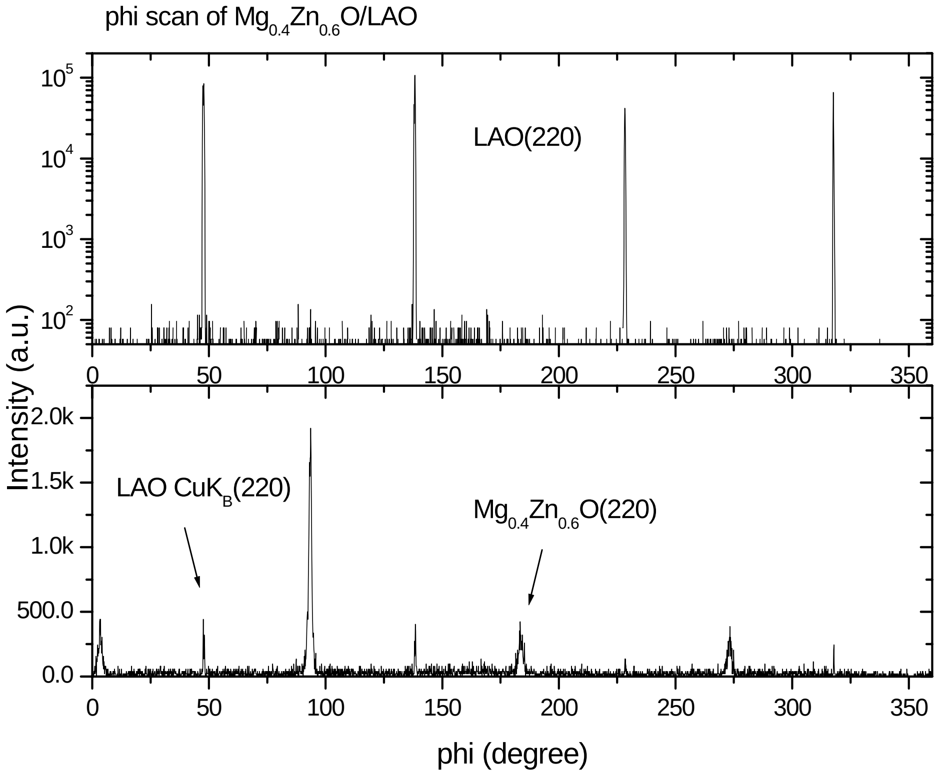

Figure 4.8 360^0-ϕ scans on $Mg_{0.4}Zn_{0.6}O$ (220) and LAO (220) reflections.

Figure 4.6 shows x-ray ϕ scans on the $Mg_{0.7}Zn_{0.3}O$ (220) and LAO (220) reflections, respectively. It is clear from the clean four-fold symmetry diffraction profiles that a heteroepitaxial cubic $Mg_{0.7}Zn_{0.3}O$ film has been grown on the LAO(100) substrate. There is however a 45° rotation between the (100) MZO and (100) LAO planes. The LAO CuK_{β} (220) four-fold symmetry diffraction peaks are also detected when performing the ϕ scan of $Mg_{0.7}Zn_{0.3}O$ film because $Mg_{0.7}Zn_{0.3}O$ (220) and LAO CuK_{β} (220) planes possess quite similar 2 theta values. The epitaxy relationship between the c-MZO film and LAO substrate is (100) $_{MgxZn1-xO}$||(100)$_{LAO}$ (out-of-plane) and (011) $_{MgxZn1-xO}$||(010)$_{LAO}$ (in-plane). Same profiles were obtained on the 360^0-ϕ scans on $Mg_{0.5}Zn_{0.5}O$ (220) and LAO (220) reflections and the 360^0-ϕ scans on $Mg_{0.4}Zn_{0.6}O$ (220) and LAO (220) reflections and shown in Figure 4.7 and 4.8, respectively. $Mg_{0.9}Zn_{0.1}O$ film has similar XRD patterns and are not shown here.

Lattice constants of the films are calculated with 2θ values and hkl indices. They are 0.4213nm, 0.4227nm, 0.4231nm and 0.4246nm for $Mg_{0.9}Zn_{0.1}O$, $Mg_{0.7}Zn_{0.3}O$, $Mg_{0.5}Zn_{0.5}O$ and $Mg_{0.4}Zn_{0.6}O$ films, respectively. We can see that the lattice constant increases with ZnO composition, in general agreement with the Vegard's law. An intuitionistic description of the relationships between the ZnO composition in MZO films, the lattice constants of MZO and 2 theta degree of the MZO (400) planes are shown in Figure 4.9.

The cubic lattice constants of MZO and LAO are ~ 4.23Å and 3.78Å respectively. The resulting lattice mismatch is over 10%. For this reason cube-on-cube epitaxial growth of c-MZO on LAO is unlikely. Instead a 45° rotated diagonal domain growth (2 diagonal units of c-MZO to 3 units of LAO) has a mismatch of less than 2%. Detailed epitaxy relationship is studied further with TEM images and is presented in section 4.2.3.

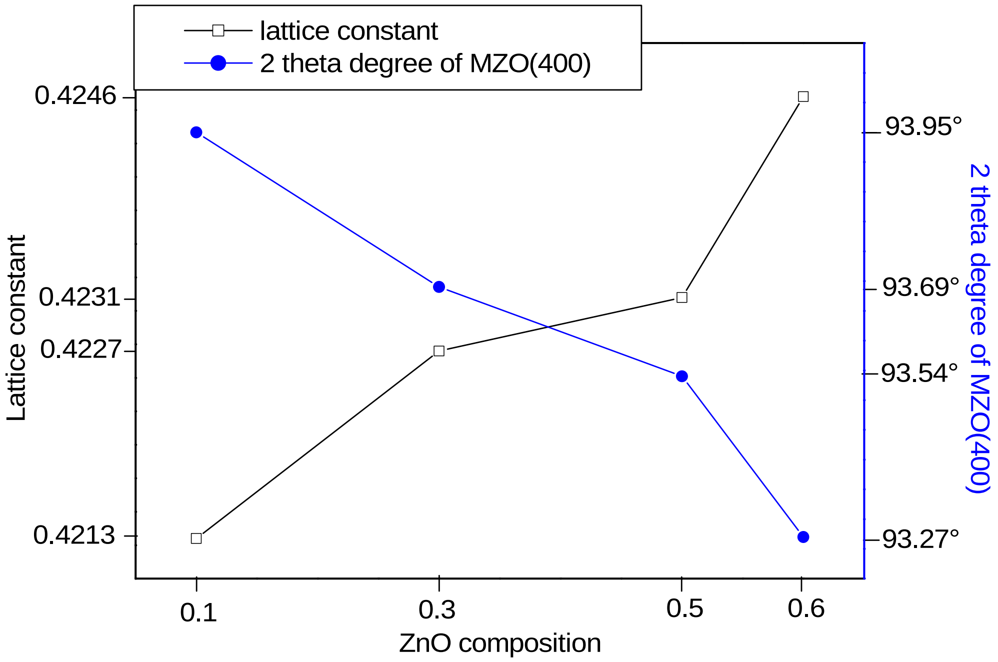

Figure 4.9 The relationships between the lattice constant data and ZnO composition in the MZO films; and the 2 theta degree of MZO (400) planes and ZnO composition in the MZO films.

4.2.2 AFM and SEM studies of surface morphology

The surface of the MZO films grown at high vacuum atmosphere is reasonably smooth except for some particulates with the size of about 1μm. Figure 4.10-4.12 show the typical AFM images of $Mg_{0.9}Zn_{0.1}O$ film, $Mg_{0.7}Zn_{0.3}O$ film and $Mg_{0.5}Zn_{0.5}O$ film grown on LAO(100) substrates with different image range. The image Z range, image Rq and the image roughness R_a over the 30μm ×30μm surface is labeled on these pictures separately. The average roughness R_a is about 100nm. Some bright ball-like areas come from big particulates on the top of these films. As-grown films littered with particulates is a typical problem in using PLD method. The physical mechanisms leading to splashing or particulate formation include the sub-surface boiling, expulsion of the liquid layer by shock wave recoil pressure and exfoliation. These particulates will greatly affect the growth of the subsequent layers as well as the electrical properties of the films. For device quality film growth, this problem can be remedied by inserting a shadow mask to block off the particulates. As a result a much more smooth film surface can be obtained.

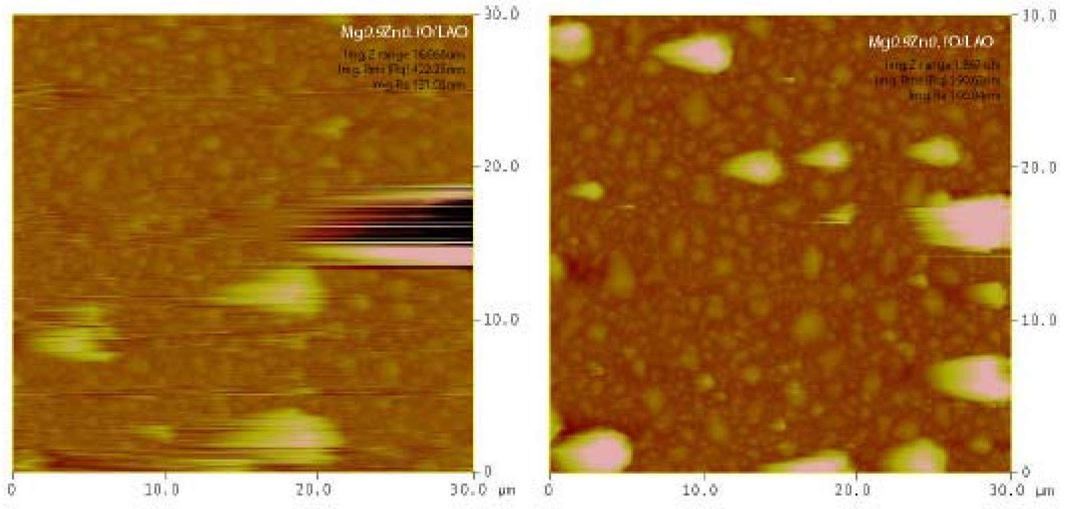

Figure 4.10 Typical AFM images of the $Mg_{0.9}Zn_{0.1}O$ film with different image range on LAO (100) substrates.

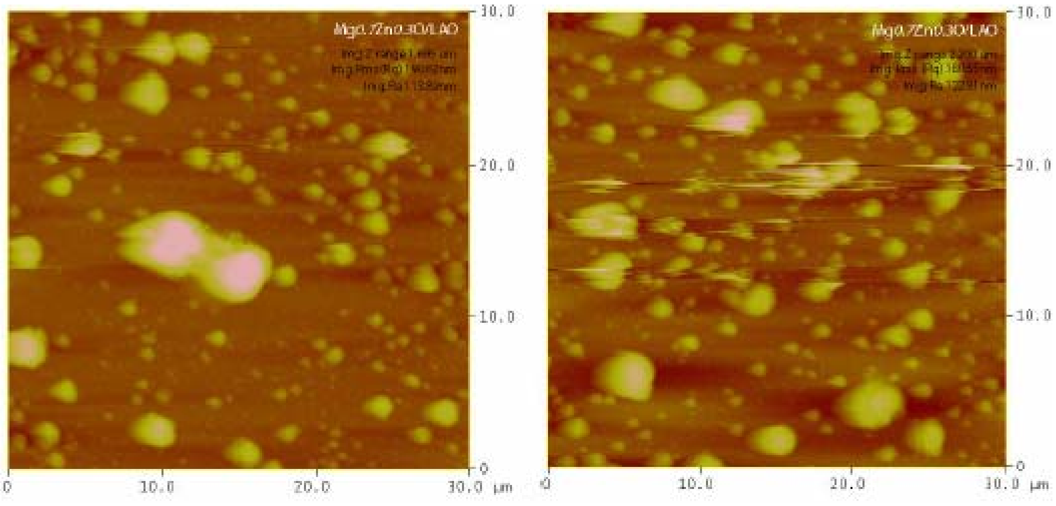

Figure 4.11 Typical AFM images of the $Mg_{0.7}Zn_{0.3}O$ film with different image range on LAO (100) substrates.

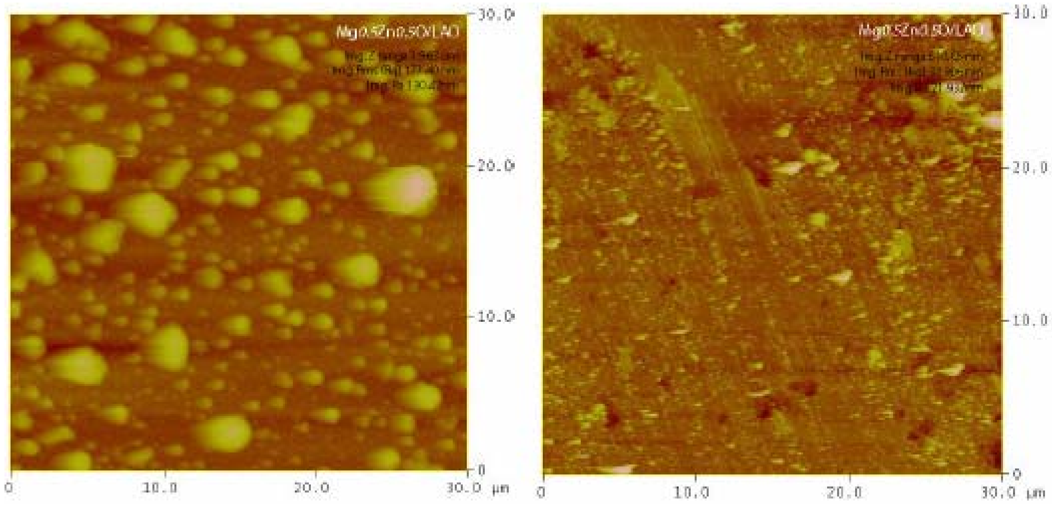

Figure 4.12 Typical AFM images of the $Mg_{0.5}Zn_{0.5}O$ film with different image range on LAO (100) substrates.

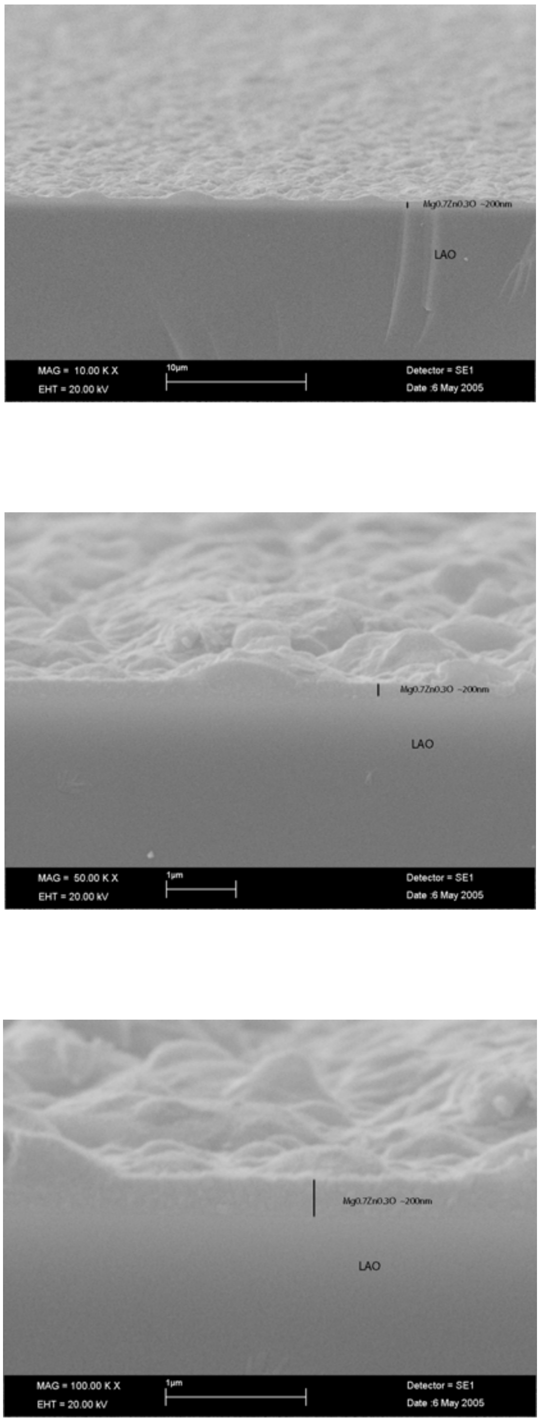

Figure 4.13 Scanning electron micrograph of cross section of the typical $Mg_{0.7}Zn_{0.3}O$ film on LAO substrate with different resolutions.

SEM photographs of cross section of typical $Mg_{0.7}Zn_{0.3}O$ film grown on LAO substrate are shown in Figure 4.13. The surfaces of the MZO films grown under vacuum are reasonably smooth and remained featureless at magnifications up to 10 000. When the magnification increases to 50 000, the surfaces become fluctuant, and some droplets or particulates with the size of about 1μm that are common in PLD deposited films could be observed. The cross-section morphology reveals sharp boundary and layer thickness is about 200nm.

4.2.3 TEM studies of epitaxial crystal arrangement characteristics

Figure 4.14(a) shows the low magnification cross-sectional bright-field TEM image from the sample $Mg_{0.6}Zn_{0.4}O$/LAO under two-beams condition with g indicated on the image. The film is about 250nm thick in agreement to the thickness estimated from the growth conditions. The image shows high density of dislocations. Most of them are confined to the interface as the consequence of domain matching epitaxy (DME), which will be discussed later in details. Figure 4.14(b) is the selective area electron diffraction (SAED) pattern taken over an area including the film and the substrate. The electron beam directions are B = [00-1] and B = [01-1] for the $LaAlO_3$ and the MZO film respectively. The pattern is indexed using regular and italic fonts for the $LaAlO_3$ and the MZO respectively. The diffraction pattern confirm the epitaxial relationship (100)MZO//(100)$LaAlO_3$, [011]MZO//[010]$LaAlO_3$.

Figure 4.15(a) shows the as-recorded high resolution TEM (HRTEM) images viewing along [0-11] MZO/ [001] $LaAlO_3$. The image demonstrates clearly the MZO film grows epitaxially with an atomically sharp interface and an in-plane epitaxy relationship [011] MZO// [010] $LaAlO_3$. The corresponding power spectrum after the FFT is shown in the inset. The (1-11), (-111) planes of MZO and the (110), (-1-10) planes of $LaAlO_3$ are labeled in the inset. The Fourier-filtered image using the marked reflections is shown in Figure 4.15(b). The dislocations are marked in the image. The Fourier-filtered image shows the matching between (111) MZO planes with (110) $LaAlO_3$ planes. However they represent the same configuration of dislocations formed from the matching of (011) MZO planes with (010) $LaAlO_3$. The periods between the dislocation are specified on the image both for the MZO and $LaAlO_3$.

The strain relaxation is analysis under the framework of domain matching epitaxy (DME). Two epitaxial relationships in the in-plane direction will be considered: (i) cube-on-cube configuration i.e. [010]MZO//[010]$LaAlO_3$, and (ii) rotation of 45° from the cube-on-cube configuration i.e. [011]MZO//[010]$LaAlO_3$. In case (i), the initial misfit strains, defined by $\varepsilon = d_f / d_s - 1$, are equal to +11.9%, where d_f ($=d_{100(\mathrm{MgZnO})}$) and d_s ($=d_{011(\mathrm{LaAlO})}$) are the spacing of planes of the film and substrate respectively. The magnitude of the strain is higher than the critical strain (7% – 8%) of conventional lattice matching. In DME, it is predicated the matching of 8 (100) planes of MZO with 9 (100) planes of $LaAlO_3$ resulting to the 8/9 domain matching. This matching leaves a residual strain ε_r of –0.53%, where $\varepsilon_r = (md_f/nd_s - 1)$ and m=8, n=9. The residual strain is accommodated by introducing the (m+1)/(n+1) domain, i.e. 9/10 domain. The alternating of these two set of domains is controlled by the frequency factor α, which is calculated from the equation: $(m+\alpha)\ d_f = (n+\alpha)\ d_s$. It follows that α is equal to 0.4 indicating the 8/9 and 9/10 domains alternates with sequence of 6 and 4. In case (ii), the analysis is carried out along two directions [011]MZO//[010]$LaAlO_3$ and [001]MZO//[011]$LaAlO_3$, in order to understand the strain relaxation for 45° rotation from cube–on –cube growth. For the alignment of (011) MZO planes with (010) $LaAlO_3$ planes, the initial misfit strain ε is –20.9%. (d_f=$d_{011(\mathrm{MgZnO})}$= 0.299nm and d_s =$d_{010(\mathrm{LaAlO})}$=0.378nm) The matching of 4/3 domain leads to residual strain ε_r of 5.5% which is accommodated by the matching of 5/4 domain. The sequence of the two domains is predicated to be 1:4 following from the frequency factor α of 0.788. For the alignment of (001) MZO planes with (011) $LaAlO_3$ planes, the initial misfit strain ε is 58.4%. (d_f=$d_{001(\mathrm{MgZnO})}$= 0.423nm and d_s =$d_{011(\mathrm{LaAlO})}$=0.267nm) The matching of 1/2 domain leads to residual strain ε_r of –20.8% which is accommodated by the matching of 2/3 domain. The sequence of the two domains is predicated to be 2:5 following from the frequency factor α of 0.712. Note that the 2/3 domain matching results in a residual strain ε_r of 5.6%. The above analysis shows that both of the cube-on-cube growth or its 45° rotated counterpart is possible under the DME. In the present study only the 45° rotated configuration was observed. It is assumed that the domain matching by 5/4, 4/3 domains along [011] MZO and 1/2, 2/3 domains along [001] MZO facilitate extra release of energy much better than the cube-on-cube situation. It is worth noting that the sequence 5/4, 4/3 domain observed in Figure 4.15(b) departs from the ideal 1:4 ratio indicating a complex strain relaxation mechanism is present.

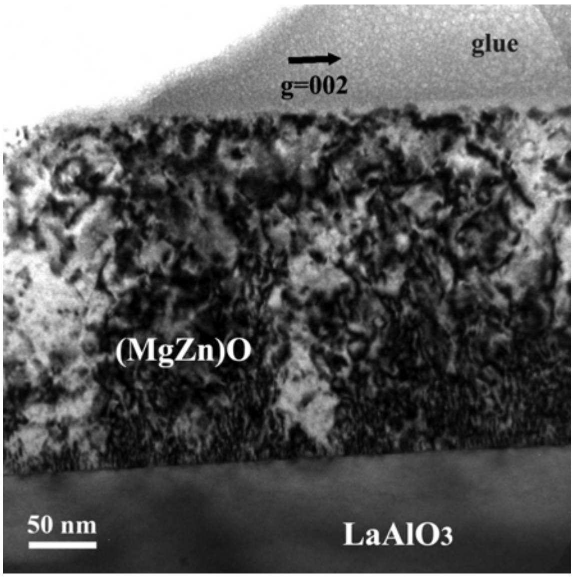

Figure 4.14 (a) Low magnification of cross-sectional bright-field TEM image showing a high density of dislocation near the interface.

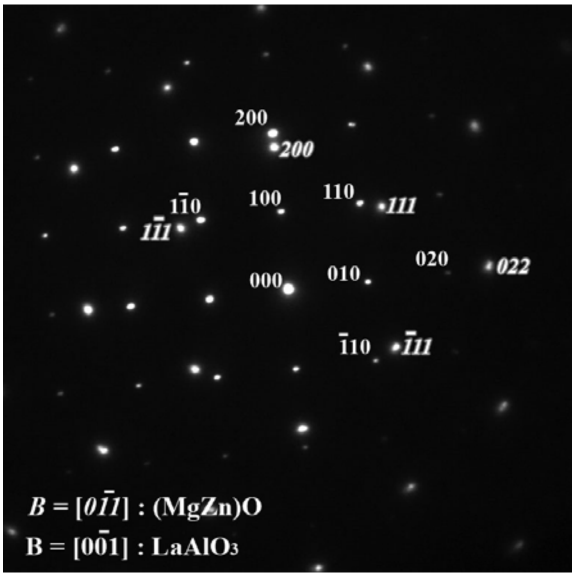

Figure 4.14 (b) SAED pattern obtained from the film and the substrate showing their epitaxial relationship.

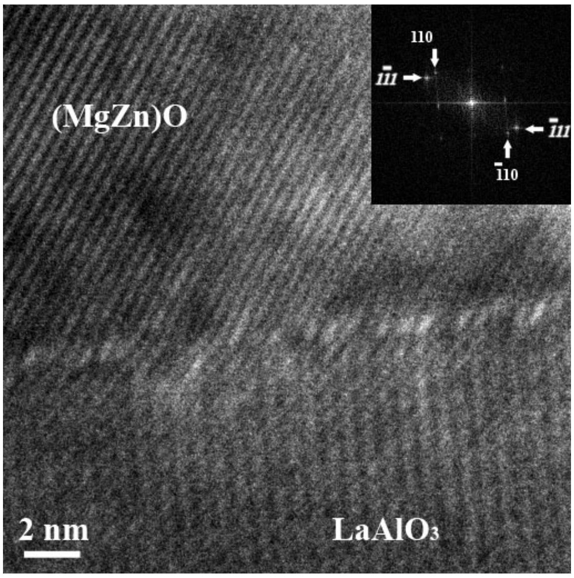

Figure 4.15 (a) As-recorded HRTEM image showing a clean interface between the film and the substrate.

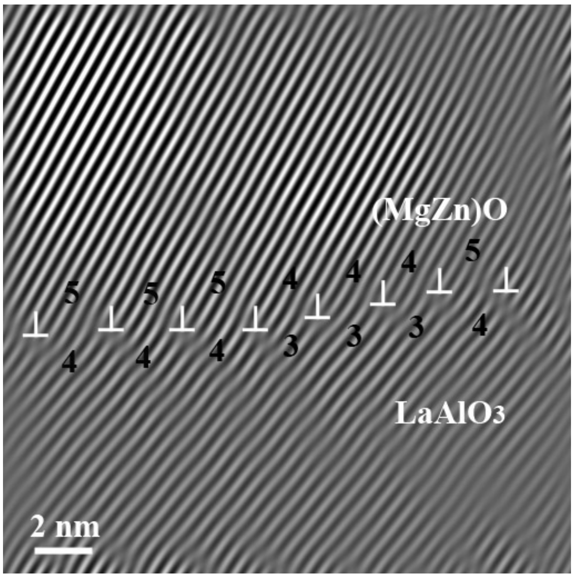

Figure 4.15 (b) The Fourier-filtered image of Figure 4.15(a) showing an array of dislocation and the lattice matching of (-111) (MgZn)O and (-110) $LaAlO_3$ planes with a ratio of 5/4.

4.2.4 FTIR spectra analysis and XPS test

Figure 4.16 shows the FTIR spectra of $Mg_xZn_{1-x}O$ films grown on LAO substrate. All c-MZO films (x=0.4, 0.5, 0.7, 0.9) with cubic structure have similar IR transmittance peak, namely a small dip at 20 μm. The hexagonal structured MZO possesses a different IR pattern, which is shown in Figure 4.35.

T. Tanigaki et al. [4-4] indicated in their measurements that a broad IR absorption peak at 20μm was due to cubic ZnO particle. Two absorption peaks, at 18.0μm and 23μm, were caused by *w*-ZnO since the haxagonal particle is a uniaxial crystal. Our FTIR data reveal a small single peak at near 20μm only, a sign of pure cubic ZnO structure. Other FTIR results on hexagonal MZO and the comparison discussion between these two structures will be presented in section 4.5.5.

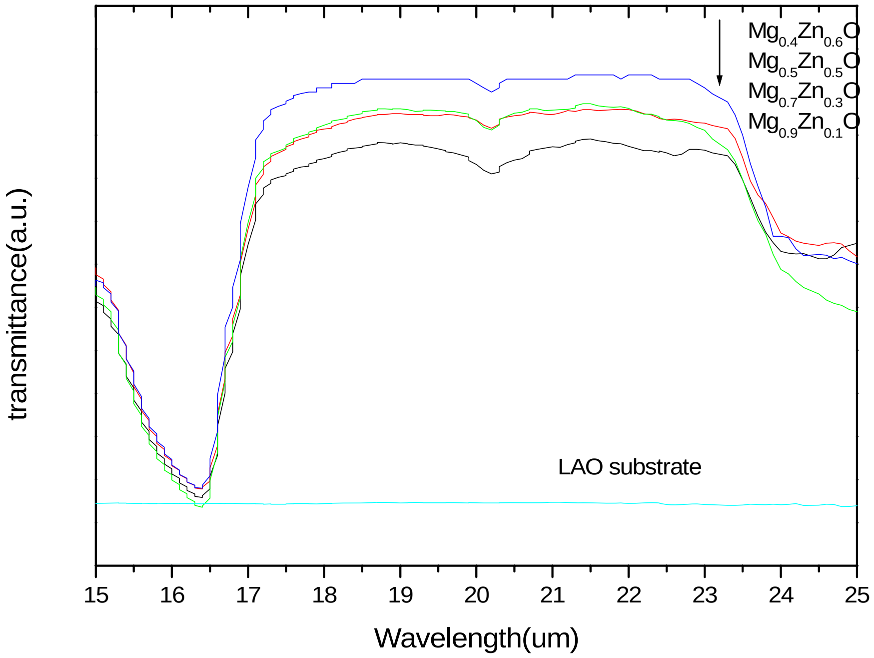

Figure 4.16 FTIR spectra of $Mg_xZn_{1-x}O$ films and LAO substrate.

The actual chemical compositions of the MZO films were studied by XPS technique. It has been reported that the Mg content in the films tends to be larger than that in the target [4-5, 4-6, 4-7], same results are obtained in our experiments. Some selected typical data are shown in Table 4.1. ZnO has a much higher vapour pressure than MgO and in the PLD process the deposited films tend to loose quite a substantial amount of Zn. Hence the actual film composition will have less Zn than the original nominal Zn content. Indeed, XPS analyses revealed film composition of $Mg_{0.6}Zn_{0.4}O$, $Mg_{0.7}Zn_{0.3}O$, $Mg_{0.82}Zn_{0.18}O$ and $Mg_{0.95}Zn_{0.05}O$, represents $Mg_{0.4}Zn_{0.6}O$, $Mg_{0.5}Zn_{0.5}O$, $Mg_{0.7}Zn_{0.3}O$ and $Mg_{0.9}Zn_{0.1}O$, respectively.

Table 4.1 Selected XPS data of $Mg_xZn_{1-x}O$ films.

Nominal composition	Atomic concentration	
	Mg	Zn
$Mg_{0.4}Zn_{0.6}O$/LAO	60	40
9nm surface sputtered $Mg_{0.4}Zn_{0.6}O$/LAO	83	17
$Mg_{0.35}Zn_{0.65}O$/LAO	73	27
9nm surface sputtered $Mg_{0.35}Zn_{0.65}O$/LAO	82	18

4.3 Microstructure and characterization of $Mg_xZn_{1-x}O$ alloy thin films on MgO (100) substrates

In fact, cubic MgO(100) substrate could provide a more matched lattice constant for $Mg_xZn_{1-x}O$ alloy thin films than that of the LAO(100) substrate. However our XRD is not able to discern the plane reflection peaks or signals between films and substrates. Nevertheless we do expect better epitaxial crystal films could be grown on MgO (100) substrates. Therefore we have also deposited $Mg_xZn_{1-x}O$ films on cubic MgO (100) substrates to form cubic MZO with high Zn content. XRD profiles and TEM photographs were used to illustrate the microstructure of $Mg_xZn_{1-x}O$/MgO heterostructure.

4.3.1 XRD studies of structural characteristics

Figure 4.17 shows the XRD θ-2θ patterns of selected $Mg_{0.4}Zn_{0.6}O$/MgO and $Mg_{0.7}Zn_{0.3}O$/MgO films deposited at 650°C. Same cubic structure patterns were obtained in this $Mg_xZn_{1-x}O$/MgO(100) series of films and reflections from (200) and (400) diffraction planes were indexed. Because $Mg_xZn_{1-x}O$ films and MgO substrate have very close lattice constants, c-$Mg_xZn_{1-x}O$ (200) diffraction at about 42.7° overlaps with that of MgO (200). At higher order diffraction region, reflection from c-$Mg_xZn_{1-x}O$ (400) at about 94.0° coincides with that of MgO (400). Comparing with Figure 4.1, c-$Mg_xZn_{1-x}O$/MgO (200) and (400) diffraction planes possess same angular positions with c-$Mg_xZn_{1-x}O$/LAO (200) and (400) diffraction planes. That is to say, substrates have little effects on the lattice parameters of c-$Mg_xZn_{1-x}O$ films.

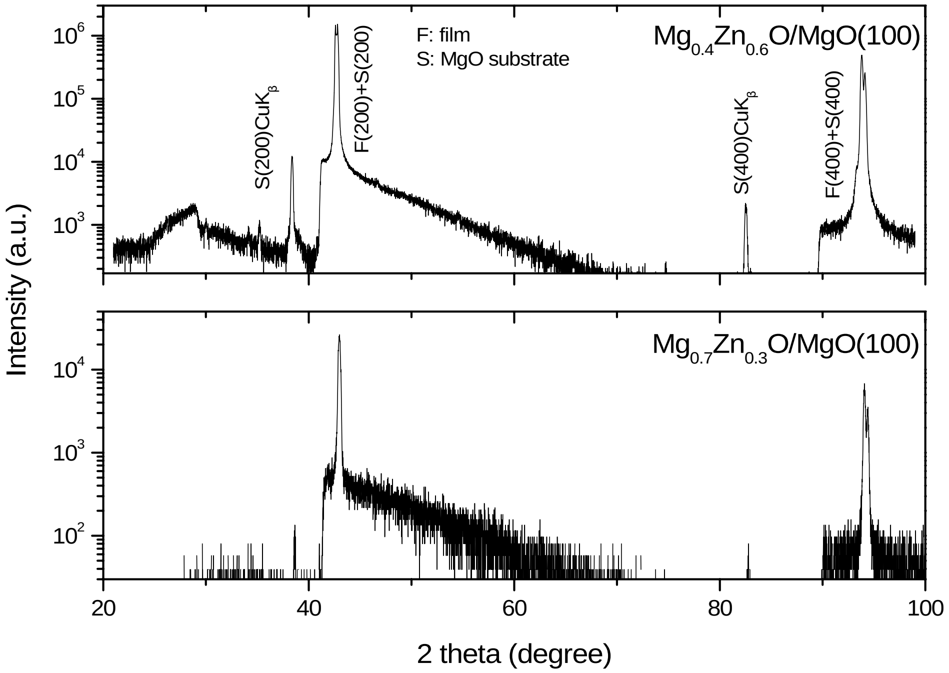

Figure 4.17 XRD 2 theta scan of $Mg_xZn_{1-x}O$/MgO(100) (x=0.4, 0.7) films (pressure: 3 ×10^{-5} Torr; temperature: 650°C).

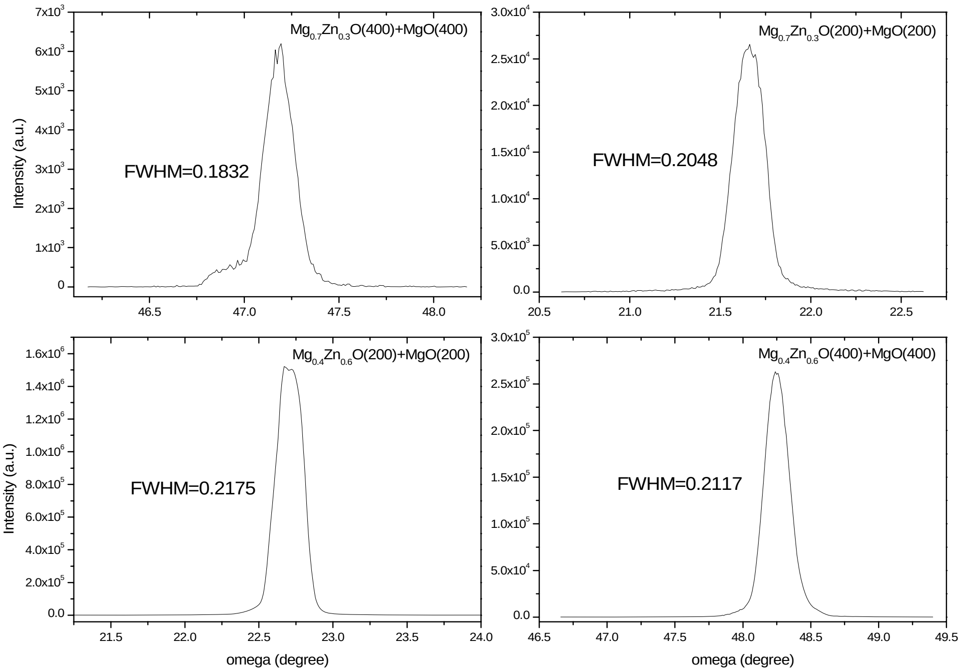

Figure 4.18 Rocking curves on the $Mg_xZn_{1-x}O$ (x=0.4, 0.7) (200) and (400) diffraction planes on MgO (100) substrates.

XRD ω-rocking curves on the $Mg_xZn_{1-x}O$ (200) and (400) reflections are shown in Figure 4.18. In fact, the weak signal of $Mg_xZn_{1-x}O$ films are completely overwhelmed by the signal of the MgO substrate. The corresponding FWHM of the curves are also noted. All of them are around 0.2°, reflecting (instrumentation limit) the crystal grain orientation of MgO substrates only.

4.3.2 TEM studies of epitaxial crystal arrangement characteristics

In order to get more precise information about the crystalline quality and the nature of interface, we performed transmission electron microscopic investigation.

Bright-field TEM micrographs of the cross section of the $Mg_{0.6}Zn_{0.4}O/MgO$ sample and the selective area electron diffraction (SAED) pattern taken over an area including the film and the substrate were carried out. The results are displayed in Figure 4.19(a) and (b). The interface between $Mg_{0.6}Zn_{0.4}O$ film and MgO substrate was studied by high resolution TEM image, which is shown in Figure 4.19(c). The interface is not easily identifiable. The diffraction pattern and the as-recorded HRTEM image confirm the perfectly matched cube-on-cube homo-epitaxial relationship (100)(MgZn)O//(100)MgO, [010](MgZn)O//[010]MgO. The film is about 150 nm thick. Crystal grains are alloy-like grown with same texture as the MgO substrate.

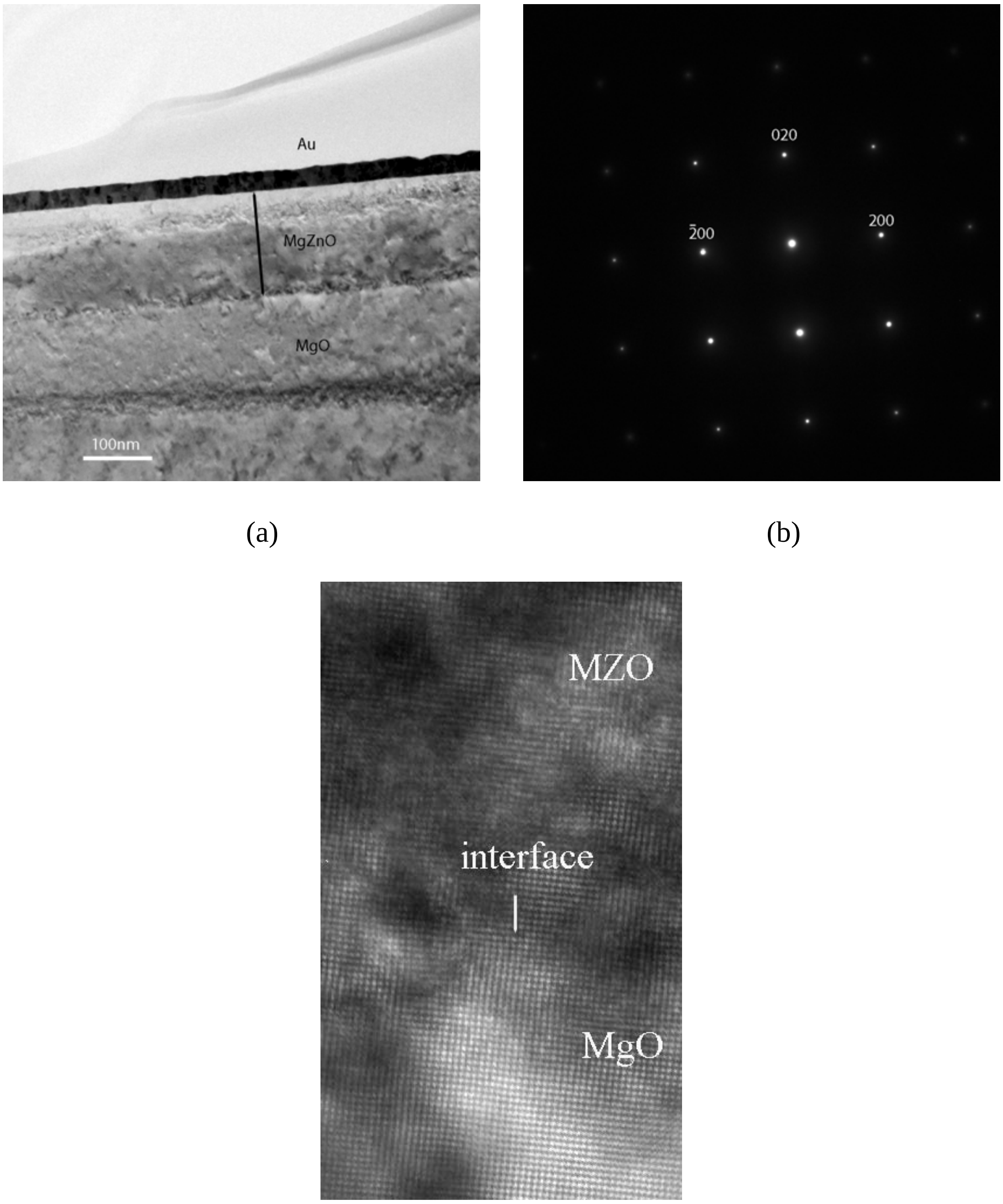

(a)

(b)

(c)

Figure 4.19 (a) Low magnification of cross-sectional bright-field TEM image of MgZnO/MgO film, (b) SAED pattern obtained from the film and the substrate showing their epitaxial relationship and (c) HRTEM image showing an unclean interface between the film and MgO substrate.

4.4 Microstructure and characterization of $Mg_xZn_{1-x}O$ alloy thin films on MgO (111) substrates

4.4.1 XRD studies of structural characteristics

Substrate is a key parameter that helps to prepare crystalline films to have a particular structure or to oriented along a certain direction so as to suit some application needs. $Mg_xZn_{1-x}O$ alloy thin films were also deposited on MgO (111) substrate with the same deposition condition. Figure 4.20 shows the XRD θ-2θ patterns of selected $Mg_xZn_{1-x}O$/MgO (111) films deposited at 650°C and pure ZnO/MgO(111) film.

Cubic crystalline structures were obtained in $Mg_xZn_{1-x}O$/MgO(111) series of films. XRD reflections from (111) and (222) diffraction planes were indexed. We have faced the same issue here as with $Mg_xZn_{1-x}O$/MgO (100) films previously. The c-$Mg_xZn_{1-x}O$ (111) plane with 2θ diffraction peak at about 36.9° overlaps with that of MgO (111) plane. The high order diffraction from c-$Mg_xZn_{1-x}O$ (222) with 2θ peak at about 78.6° coincides with that of MgO (222) plane. All these make the identification of c-MZO (111) difficult.

XRD ω-rocking curves on the selected $Mg_{0.4}Zn_{0.6}O$ (111) and (222) reflections are shown in Figure 4.21 for reference. Weak signals of $Mg_{0.4}Zn_{0.6}O$ film are over shadowed by those of MgO substrate of high intensity. The corresponding FWHM of the curves are around 0.2°, masking the actually crystal grain orientation of the $Mg_{0.4}Zn_{0.6}O$ film.

Figure 4.20 simultaneously gives the 2θ XRD pattern of ZnO film deposited on MgO (111) substrate. From the figure, we know that a high-quality ZnO film has been grown on the substrate. Preferred (0002) and (0004) orientations with high intensity were observed. C-axes of the ZnO crystal grains become uniformly perpendicular to the substrate surface at current deposition temperature. It is reported that the surface energy of (0002) planes is the lowest in the ZnO crystal [4-8]. Grains with the lower surface energy will become larger as the films grows. Hence the crystal orientation develops into one crystallographic direction of the lowest surface energy, which means that the (0002) texture of ZnO may be easily formed. Figure 4.21 includes the ω scan of ZnO (0002) and (0004) peak, the FWHM of the curve is about 1.5°, indicating a fairly good crystal grain orientation.

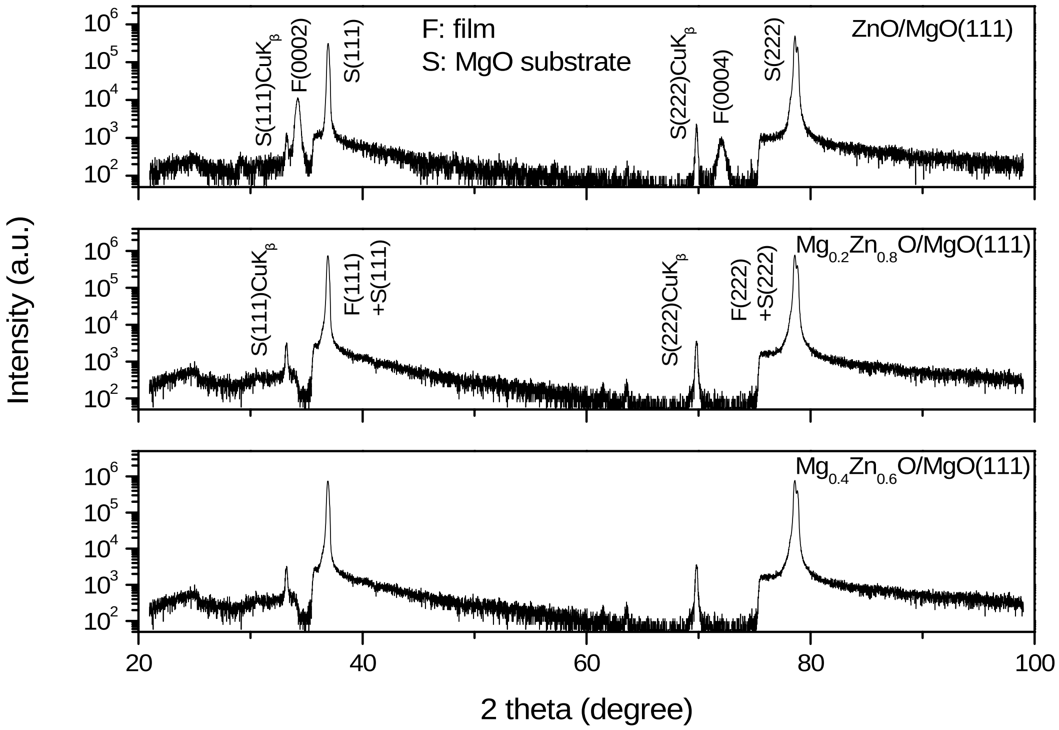

Figure 4.20 XRD 2 theta scan of $Mg_xZn_{1-x}O$/MgO(111) (x=0.2, 0.4) films and ZnO/MgO(111) film (pressure: 3×10^{-5} torr; temperature: 650°C).

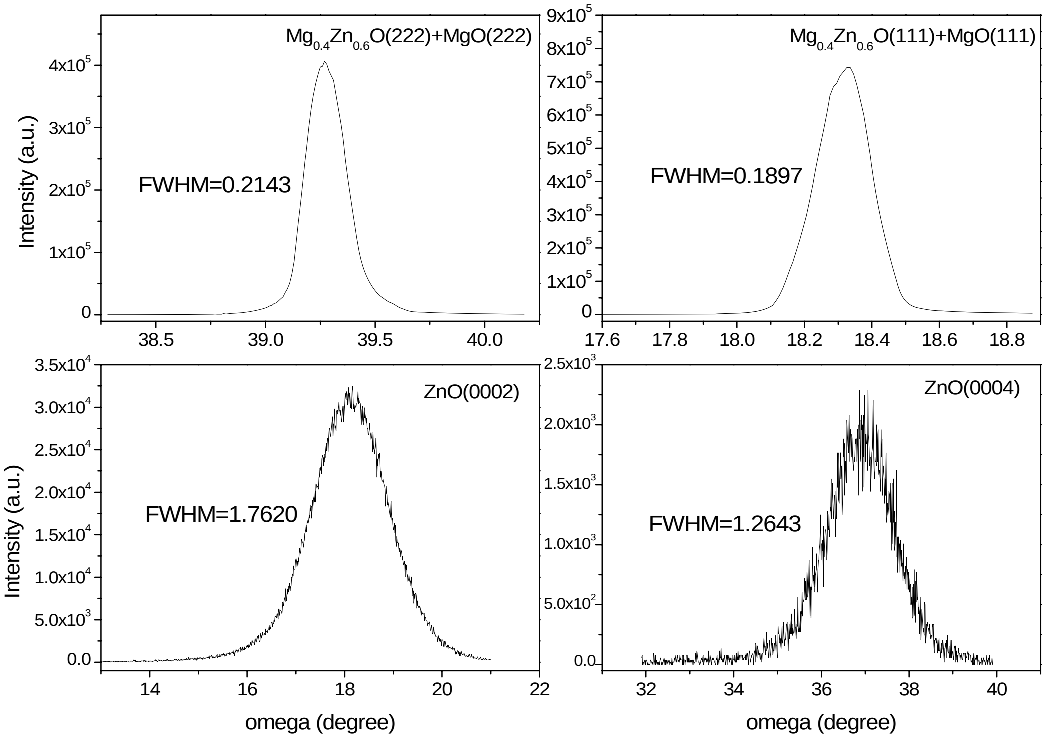

Figure 4.21 Rocking curves on the $Mg_{0.4}Zn_{0.6}O$ (111) and (222) diffraction planes and ZnO (0002) and (0004) diffraction planes on MgO (111) substrates.

As for the epitaxial relationship measurement, 360^0-ϕ scan is taken on ZnO (1002) and MgO (002) reflections respectively, which is shown in Figure 4.22. Three-fold symmetry diffraction peaks of MgO(002) and six-fold symmetry diffraction profiles of ZnO(1002) were observed, indicating that the ZnO layer was heteroepitaxially grown on the MgO(111) substrate with epitaxial relationships of (0001)ZnO||(111)MgO (out-of-plane) and (1002)ZnO||(002)MgO (in-plane).

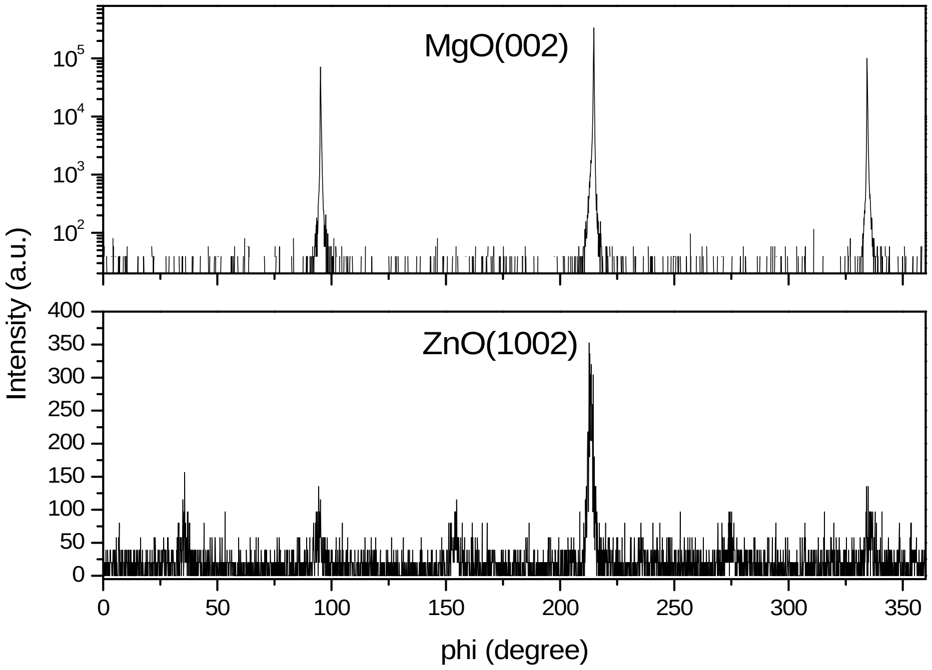

Figure 4.22 360^0-ϕ scans on ZnO (1002) and MgO (002) reflections.

4.4.2 SEM studies of surface morphology

Figure 4.23 illustrates the surface analysis by SEM made on the $Mg_{0.4}Zn_{0.6}O$/MgO(111) sample. The revealed feature confirms the uniformity of the film and its good coherent nature with the substrate. Film exhibits smooth, dense and mirror-like microstructure without crack and large voids. Only a few particles on the surface are observed.

SEM photographs of cross section of a typical ZnO film grown on MgO (111) substrate are shown in Figure 4.24. The discernable layer with columnar structure is observed. The thickness of ZnO layer is estimated to be about 300nm. The interface appears smooth and sharp.

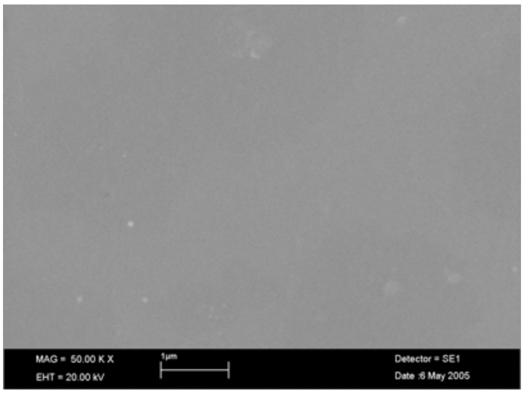

Figure 4.23 SEM surface morphology of $Mg_{0.4}Zn_{0.6}O$ thin film on MgO (111) substrate.

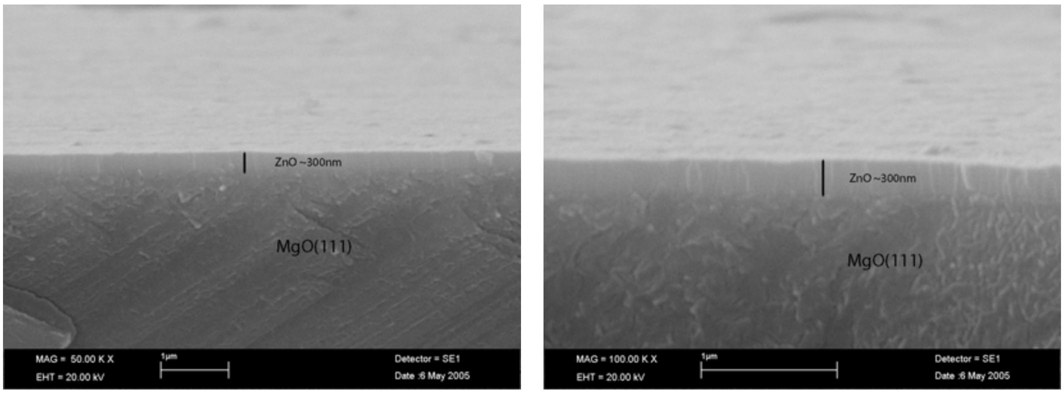

Figure 4.24 Scanning electron micrograph of cross section of the typical ZnO film on MgO (111) substrate with different resolutions.

4.5 Microstructure and characterization of $Mg_xZn_{1-x}O$ alloy thin films on Al_2O_3 (0001) substrates

4.5.1 XRD studies of structural characteristics and XPS test

$Mg_xZn_{1-x}O$ alloy thin films have also been successfully grown on Al_2O_3 (0001) substrate by pulsed laser deposition. The structural properties of the deposited $Mg_xZn_{1-x}O$ films of selected composition (x=0, 0.2, 0.4) were characterized by four-circle x-ray diffractometer. Figure 4.25 shows the XRD θ-2θ profiles of $Mg_xZn_{1-x}O$ films deposited at 650°C. The strong reflections of MZO(0002) and (0004) diffraction planes are identified in ZnO and $Mg_{0.2}Zn_{0.8}O$ films, which are different from those of $Mg_{0.4}Zn_{0.6}O/Al_2O_3$ film(detailed discussion will be shown in later paragraph). No trace of other reflection is observed, indicating the films are single phase. We also observed peaks corresponding to (0006) and (00012) planes of sapphire. The Al_2O_3 substrate (0006) CuK_β peak and (00012) CuK_β peak were also indexed. The ω-scan rocking curves were performed to gauge the orientation quality of the films, as shown in Figure 4.26. The full width at half maximum of ZnO (0002) and ZnO (0004) is 0.7494° and 0.6108°, and of $Mg_{0.2}Zn_{0.8}O$ (0002) and (0004) is 1.4364° and 0.8737°, respectively.

Comparing the ZnO (0004) plane with the $Mg_{0.2}Zn_{0.8}O$ (0004) plane, the 2 theta values equal to 72.74° and 72.36° for $Mg_{0.2}Zn_{0.8}O$ and ZnO, respectively. Same with the result of $Mg_xZn_{1-x}O$ films deposited on LAO substrates, MZO planes diffraction peaks shift to lower 2 theta angles when increasing the ZnO content. This is due to a slight expansion in the lattice constant when substituting the Mg^{2+} ion with larger Zn^{2+} ion. However, the increase rate in lattice parameter is small because of the similarity of the ionic radii of Mg^{2+} and Zn^{2+} ions.

The XRD 360° ϕ-scan of the $Mg_xZn_{1-x}O$ (1002) and Al_2O_3 (1002) were performed to confirm the epitaxy of the grown films. The results are shown in Figure 4.28 and 4.29. It is noticed that the peaks are separated by 60° due to a six-fold symmetry in the diffraction profiles of $Mg_xZn_{1-x}O$ (1002), while the peaks are separated by 120° due to a three-fold symmetry in the diffraction profiles of Al_2O_3 (1002). It is shown that MZO grows epitaxialy on sapphire with preferred c-axis orientation. However, the ϕ-scan clearly revealed a 30° rotation between some planes of MZO and Al_2O_3. This in-plane rotation relationship differs from the ϕ-scan result of MZO and MgO(111), which has no rotation and is shown in Figure 4.22. The epitaxial relationship between the film and substrate is concluded to be (0001)MZO||(0001)Al_2O_3 (out-of-plane) and (1002)MZO||(1002) Al_2O_3(in-plane).

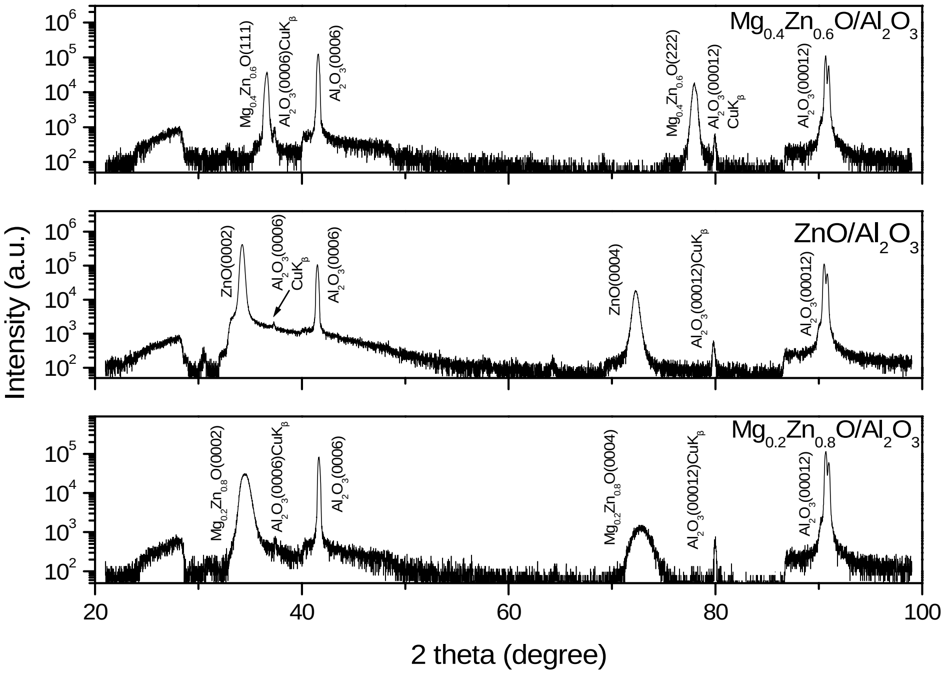

Figure 4.25 XRD 2 theta scan of $Mg_xZn_{1-x}O/Al_2O_3(0001)$ (x=0,0.2,0.4) film (pressure: 3×10^{-5} torr; temperature: 650°C).

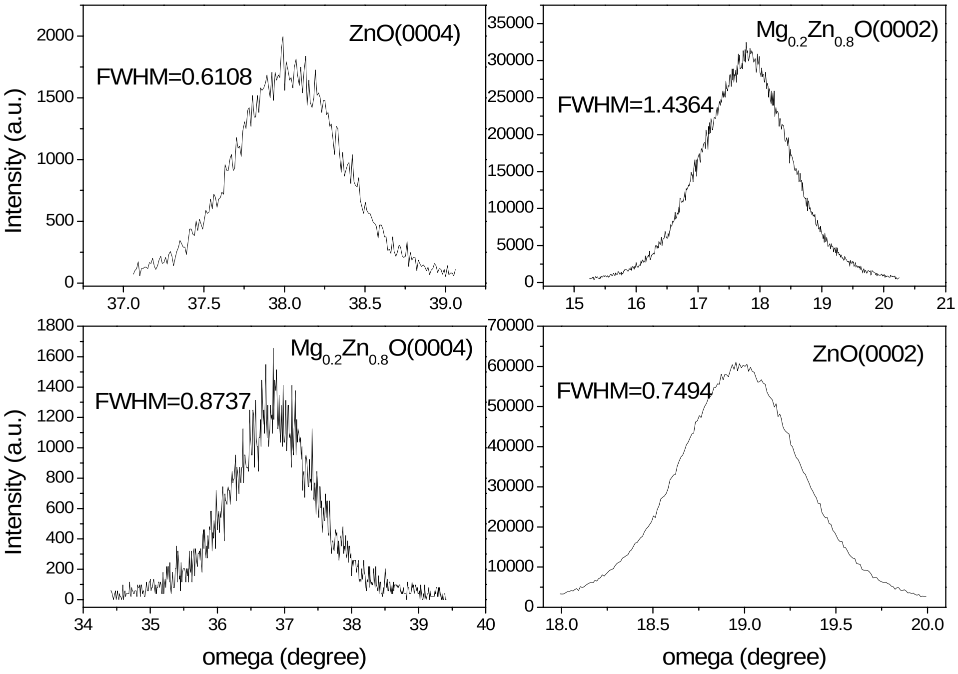

Fgiure 4.26 Rocking curves on the $Mg_xZn_{1-x}O$ (x=0, 0.2) (0002) and (0004) diffraction planes on Al_2O_3 (0001) substrates.

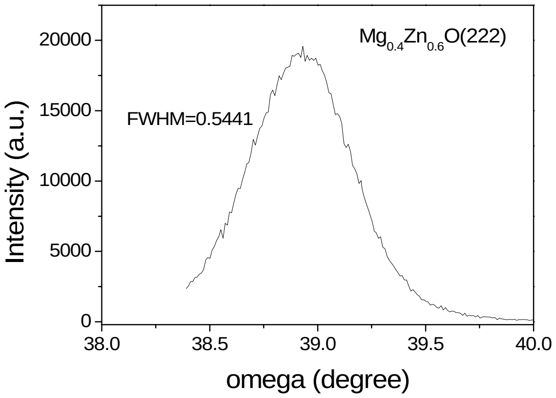

Fgiure 4.27 Rocking curve on the $Mg_{0.4}Zn_{0.6}O$ (222) diffraction plane on Al_2O_3 (0001) substrate.

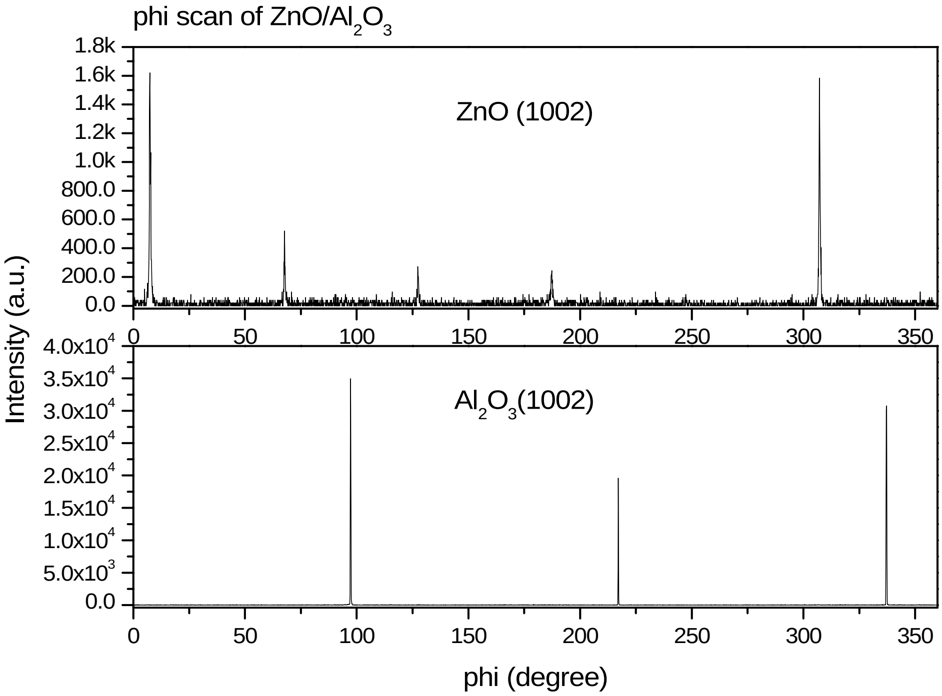

Figure 4.28 360^0-ϕ scans on ZnO (1002) and Al_2O_3 (1002) reflections.

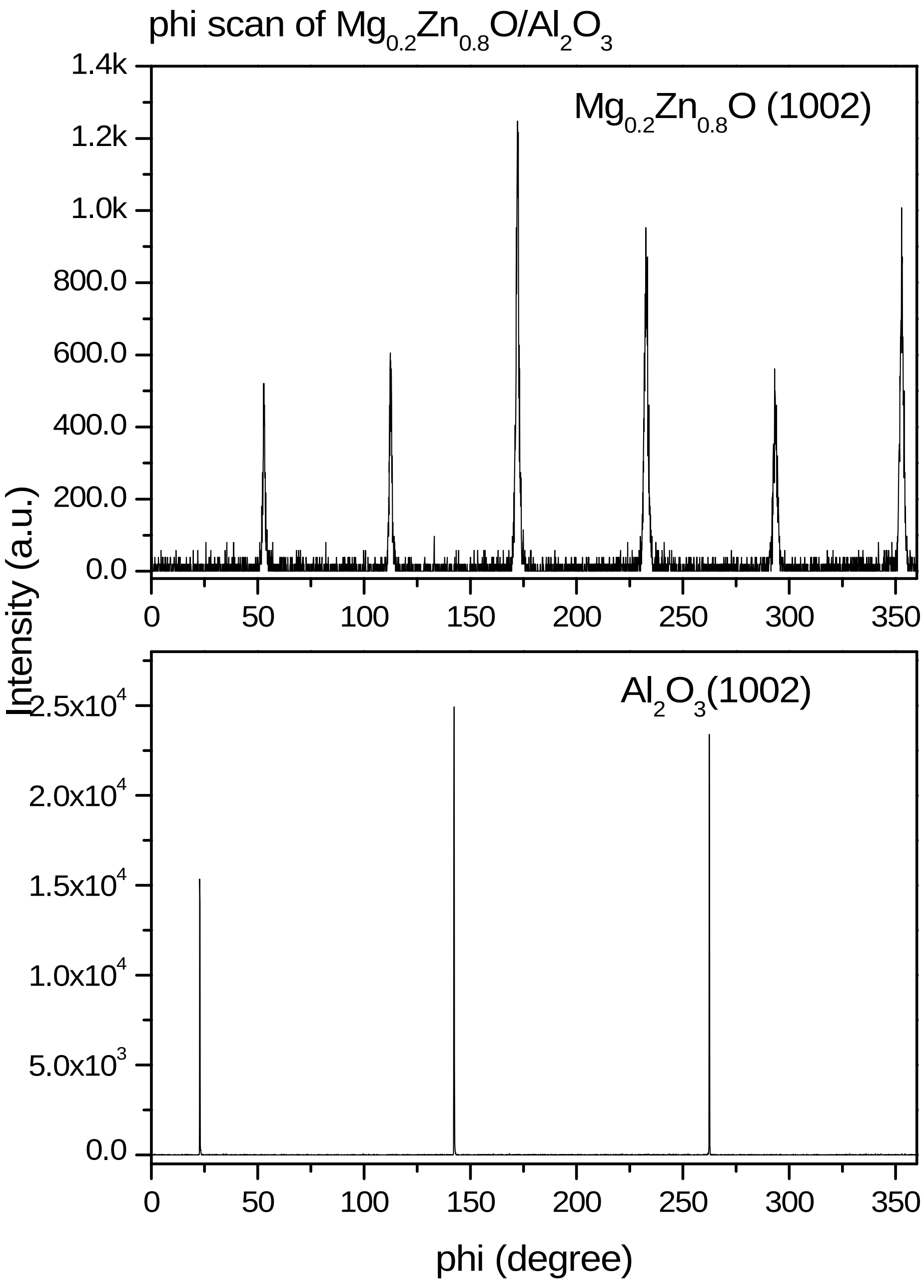

Figure 4.29 360^0-ϕ scans on $Mg_{0.2}Zn_{0.8}O$ (1002) and Al_2O_3 (1002) reflections.

As for the $Mg_{0.4}Zn_{0.6}O/Al_2O_3$ film, different structure was obtained from $Mg_{0.2}Zn_{0.8}O/Al_2O_3$ and ZnO/Al_2O_3 films. Cubic structure patterns were shown in Figure 4.25 and reflections from $Mg_{0.4}Zn_{0.6}O$(111) and $Mg_{0.4}Zn_{0.6}O$(222) diffraction planes were indexed. This structure is the same as that of $Mg_{0.4}Zn_{0.6}O$ film deposited on MgO (111) substrate. XRD ω-rocking curve on the $Mg_{0.4}Zn_{0.6}O$ (222) diffraction of film grown on Al_2O_3 (0001) substrate is shown in Figure 4.27. The corresponding FWHM of the curve is measured to be 0.544°, indicating a good crystal grain orientation of the $Mg_{0.4}Zn_{0.6}O/Al_2O_3$ film. This value could also be obtained for $Mg_{0.4}Zn_{0.6}O$ (222) grown on MgO (111) substrate, only that it is too weak to be completely overshadowed by the diffraction from the MgO (111) substrate. Detailed epitaxy relationship of $Mg_{0.4}Zn_{0.6}O$ film on Al_2O_3 substrate is studied further with TEM images.

From the above XRD results, we know that cubic $Mg_{0.4}Zn_{0.6}O$ film was realized even on Al_2O_3 substrate. Hexagonal $Mg_{0.2}Zn_{0.8}O$ and ZnO films, on the other hand, were obtained on sapphire substrates. XRD patterns of $Mg_{0.2}Zn_{0.8}O$ and ZnO targets are the same, which is presented in Figure 3.4. The reason is that in the $Mg_{0.2}Zn_{0.8}O$ phase, Mg^{2+} ions replace some of the Zn^{2+} ions by managing to keep the original ZnO hexagonal structure.

On the other hand, films grown from ablating $Mg_{0.4}Zn_{0.6}O$ target have mixed phases. Apart from reflections that could be indexed according to the hexagonal ZnO phase, some reflections from the cubic MgO phase appeared. According to the XPS result of $Mg_{0.35}Zn_{0.65}O/Al_2O_3$ film, which is shown in Table 4.2, the actual composition is about $Mg_{0.68}Zn_{0.32}O$. The films loose quite a lot of Zn content in the PLD deposition process because ZnO has a much higher vapour pressure than MgO. Therefore we could conclude that films possess higher Mg amount than the original nominal amount. The actual Mg content in $Mg_{0.4}Zn_{0.6}O/Al_2O_3$ film is therefore more than 60%. Cubic MgO dominate the structure formation in $Mg_{0.4}Zn_{0.6}O$ film and cubic $Mg_{0.4}Zn_{0.6}O$ films with (111) preferred orientation were obtained on Al_2O_3 substrate.

Table 4.2 XPS data of $Mg_{0.35}Zn_{0.65}O/Al_2O_3$ film.

Nominal composition	Atomic concentration	
	Mg	Zn
$Mg_{0.35}Zn_{0.65}O/Al_2O_3$	68	32
9nm surface sputtered $Mg_{0.35}Zn_{0.65}O/Al_2O_3$	80	20

4.5.2 Comparison study of XRD structural characteristics of $Mg_xZn_{1-x}O$ alloy thin films on MgO (111) and Al_2O_3 (0001) substrates

Figure 4.30 shows the comparison study of the XRD 2 theta scans of $Mg_{0.4}Zn_{0.6}O$ films on MgO (111) and Al_2O_3 (0001) substrates under the same conditions. Same cubic structure patterns with reflections from $Mg_{0.4}Zn_{0.6}O$ (111) and $Mg_{0.4}Zn_{0.6}O$ (222) diffraction planes were obtained, although films are deposited differently on cubic MgO and hexagonal sapphire substrates.

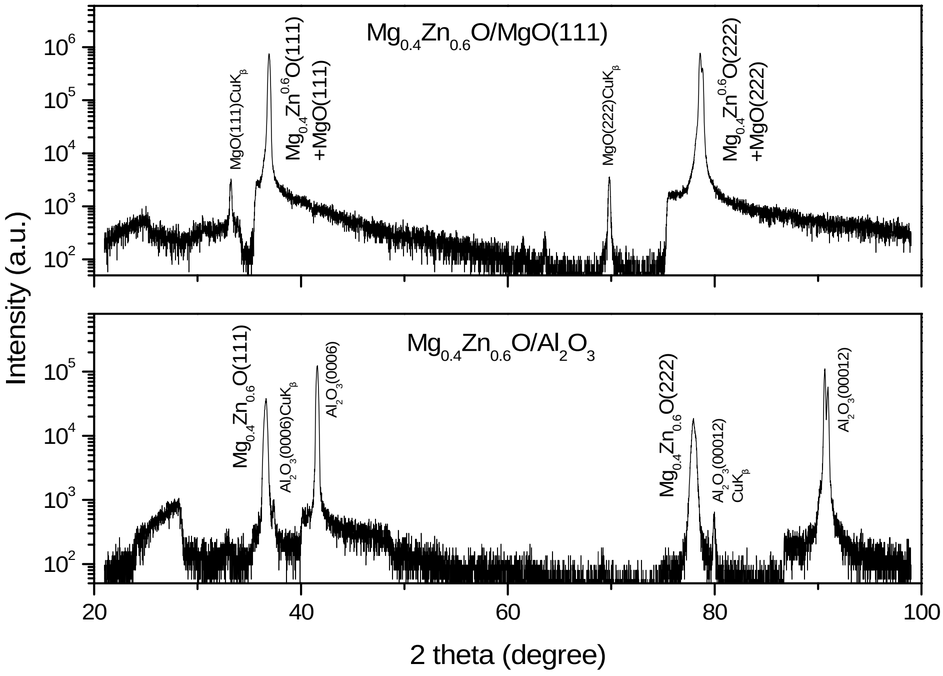

Figure 4.30 XRD 2 theta scans of $Mg_{0.4}Zn_{0.6}O$ films on MgO(111) and Al_2O_3(0001) substrates (same conditions, pressure: 3×10^{-5} torr; temperature: 650°C).

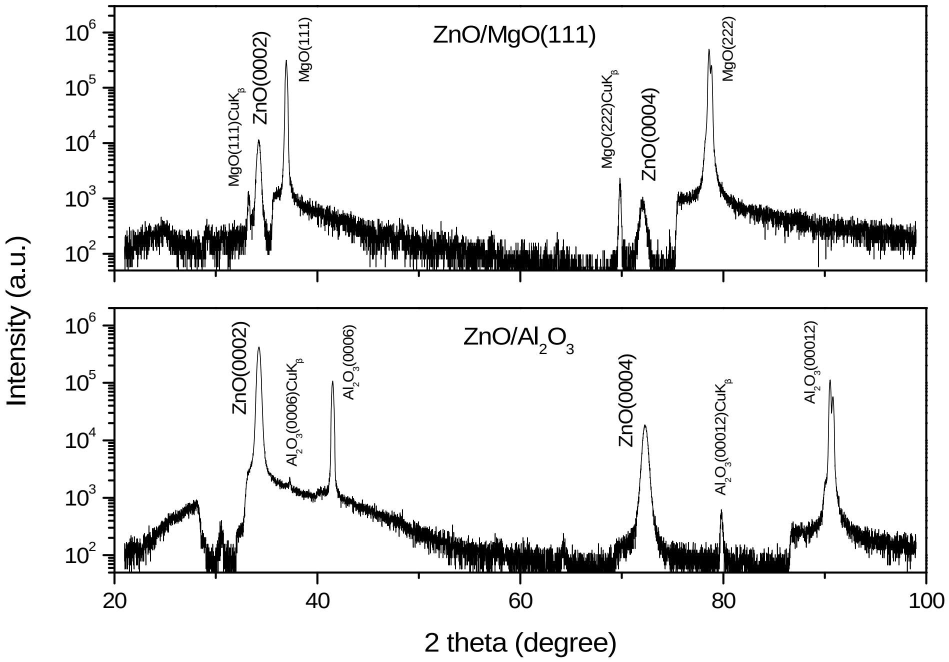

Figure 4.31 XRD 2 theta scans of ZnO films on MgO(111) and Al_2O_3(0001) substrates (same conditions, pressure: 3×10^{-5} torr; temperature: 650°C).

The comparative studies of the XRD 2 theta scans of ZnO films on MgO (111) and Al_2O_3 (0001) substrates are shown in Figure 4.31. Same hexagonal structure patterns with reflections from ZnO (0002) and ZnO (0004) diffraction planes at same 2θ angle are seen and indexed. It is evident that ZnO films can be heteroepitaxially grown on these two kinds of substrates.

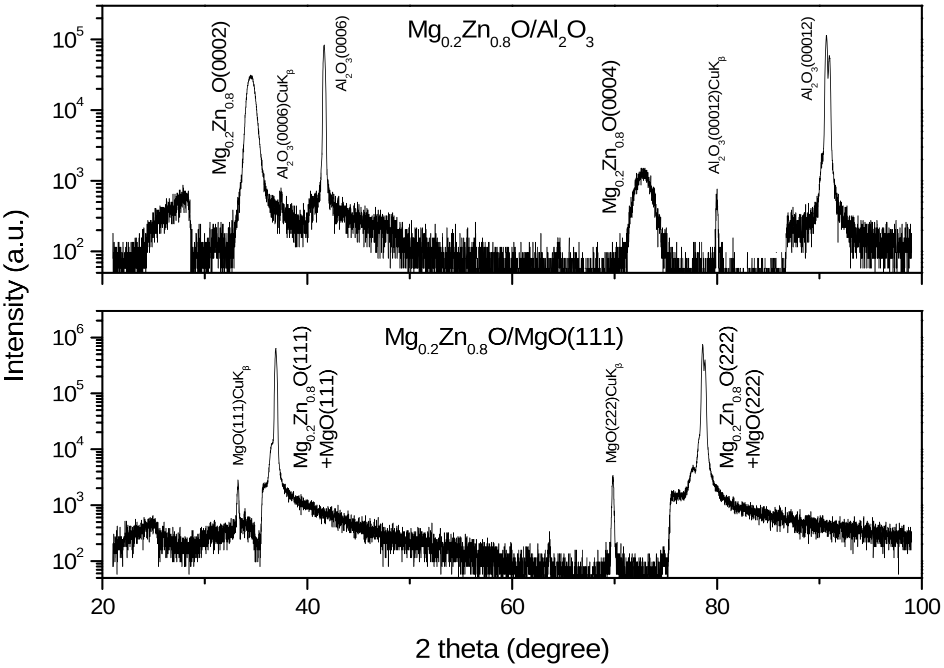

Figure 4.32 XRD 2 theta scans of $Mg_{0.2}Zn_{0.8}O$ films on MgO(111) and Al_2O_3(0001) substrates (same conditions, pressure: 3×10^{-5} torr; temperature: 650°C).

However, for the $Mg_{0.2}Zn_{0.8}O$ films deposited on MgO (111) and Al_2O_3 (0001) substrates, different structure were obtained. Figure 4.32 shows the comparison study of the XRD 2 theta scans of $Mg_{0.2}Zn_{0.8}O$ films on MgO (111) and Al_2O_3 (0001) substrates. $Mg_{0.2}Zn_{0.8}O/Al_2O_3$(0001) film possesses the same hexagonal structure pattern as that of the ZnO/Al_2O_3(0001) film. The reason has been discussed in section 4.5.1. On the other hand, cubic structure pattern with reflections from $Mg_{0.2}Zn_{0.8}O$ (111) and $Mg_{0.2}Zn_{0.8}O$ (222) diffraction planes was obtained for films grown on MgO (111) substrate. We could conclude that substrates play a deciding role on the formation of crystalline $Mg_{0.2}Zn_{0.8}O$ film.

4.5.3 SEM studies of surface morphology

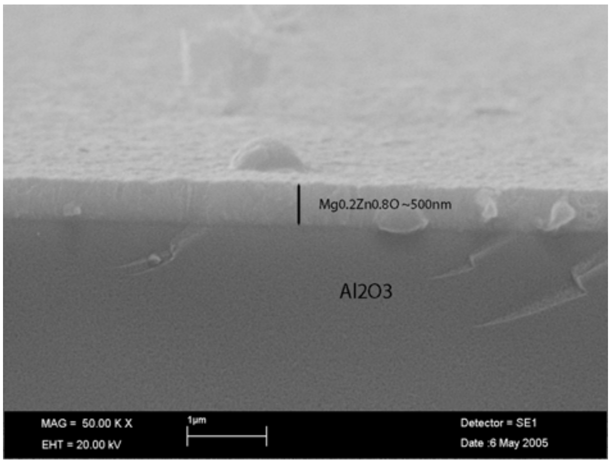

Figure 4.33 Scanning electron micrograph of cross section of the typical $Mg_{0.2}Zn_{0.8}O$ film on Al_2O_3 substrate.

Scanning electron microscopy was employed to characterize the cross-section morphology of the selected $Mg_{0.2}Zn_{0.8}O/Al_2O_3$ film. The image is shown in Figure 4.33. Similarly, the film exhibits smooth and dense microstructure without large voids or cracks. A few particulates are observed on the surface. Columnar structure of $Mg_{0.2}Zn_{0.8}O$ layer is evident and the interface between film and Al_2O_3 substrate is smooth and sharp. The thickness of $Mg_{0.2}Zn_{0.8}O$ film is estimated to be about 500nm. Comparing the picture with those of MZO/LAO films, which are shown in Figure 4.13, we know that the MZO/LAO film has a larger average roughness than that of the MZO/Al_2O_3 film. Substrate effect is the only factor that contributes to this phenomenon.

4.5.4 TEM studies of epitaxial crystal arrangement characteristics

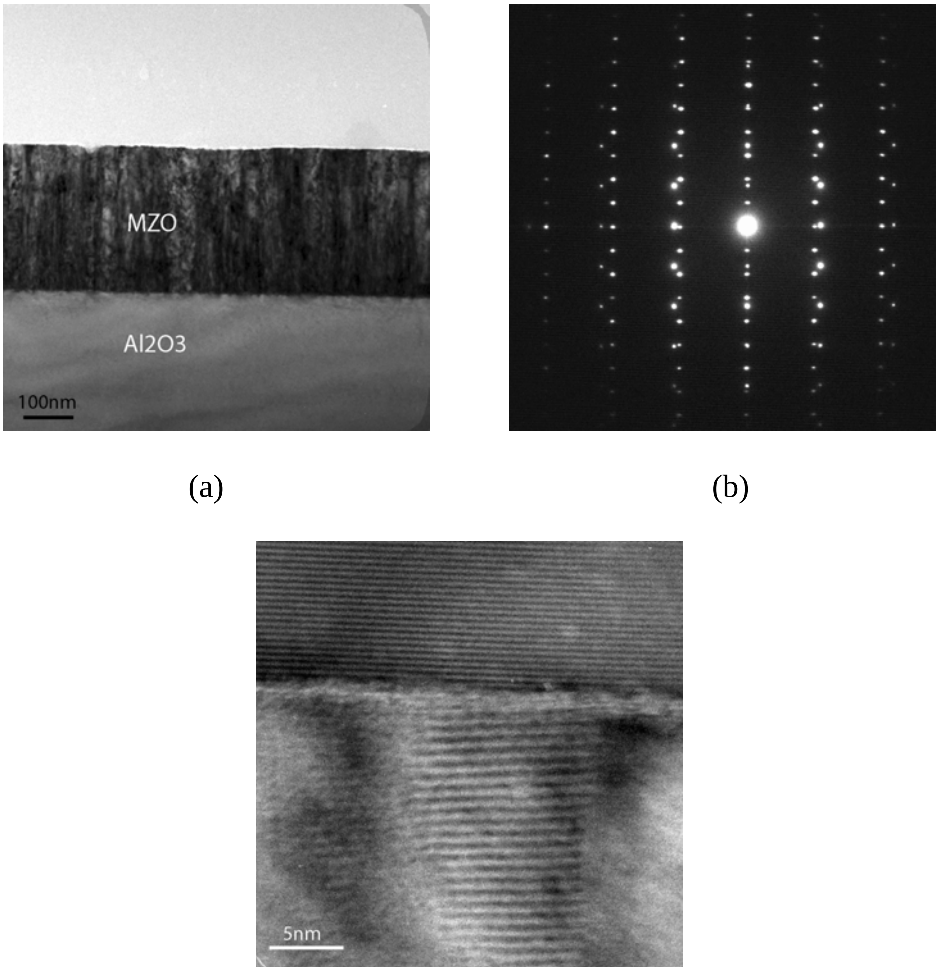

(a) (b)

(c)

Figure 4.34 (a) Low magnification of cross-sectional bright-field TEM micrograph of MgZnO/Al_2O_3 (0001) film, (b) SAED pattern obtained from the film and the substrate showing their epitaxial relationship and (c) high resolution of cross-sectional TEM photograph of MgZnO/Al_2O_3 (0001) film.

Transmission electron microscope was used to investigate the heterostructure in order to get more precise information about the nature of the MZO/Al_2O_3 interface and the crystalline quality on the substrate. The bright-field cross-section TEM micrograph from the MZO/Al_2O_3 (0001) film is shown in Figure 4.34(a), while the corresponding SAED pattern of the film is shown in Figure 4.34(b). The pattern contains diffraction spots corresponding to epitaxial MZO film and sapphire substrate, respectively. Typical columnar crystal grains produced by PLD and oriented vertically to the substrate are obtained. They directly verify the c-axis orientation of the film. High resolution of cross-sectional TEM photograph of MgZnO/Al_2O_3 (0001) film is shown in Figure 4.34(c), film and substrate both contain parallel lines. Detailed epitaxial relationships should be studied further.

4.5.5 FTIR spectra analysis

IR spectra of MZO grown on Al_2O_3 substrate are depicted in Figure 4.35. It is shown that the peaks near 16μm and 20μm in hexagonal MZO/Al_2O_3 film are due to the different frequency of the material in two directions ($C\perp$ and $C||$), which reflected an atomic bonding force difference in the film. T.Tanigaki et al [4-4] indicated that there is broad IR absorption peak at 20μm in cubic ZnO particle and two absorptions at 18μm and 23μm in ZnO hexagonal particle since the hexagonal particle is a uniaxial crystal. Our experiments revealed similar results.

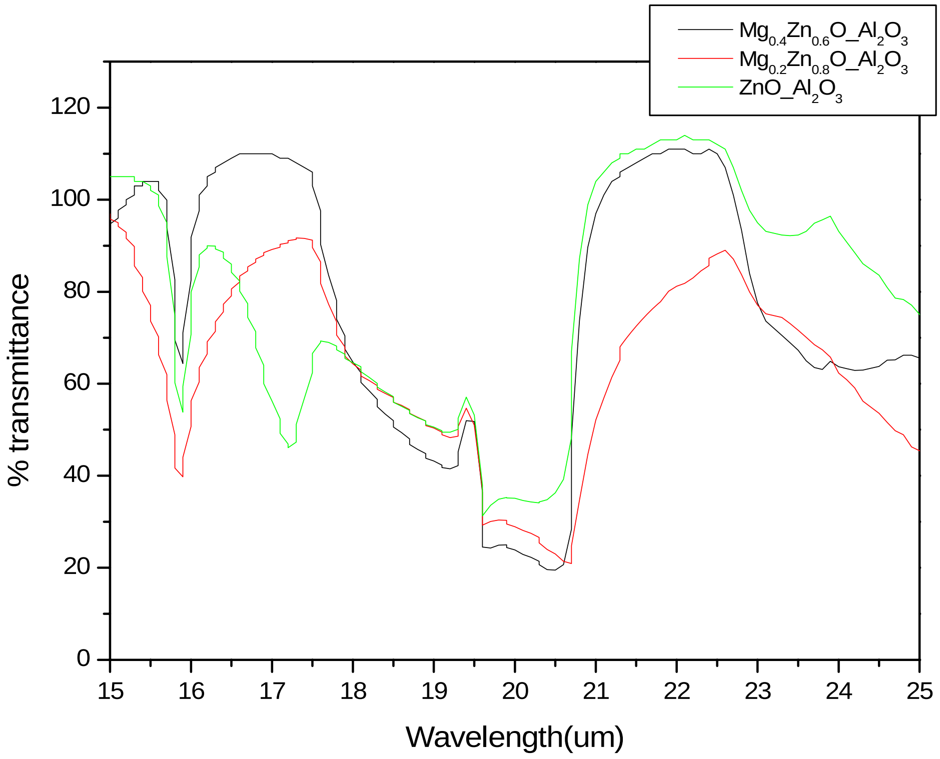

Figure 4.35 FTIR spectra of $Mg_xZn_{1-x}O$ films on Al_2O_3 substrate.

CHAPTER 5

FABRICATION AND CHARACTERIZATION OF p-$Li_{0.15}Ni_{0.85}O$/n-Nb-STO, p-$Li_{0.15}Ni_{0.85}O$/n-ZnO and p-$Li_{0.15}Ni_{0.85}O$/n-In-$Mg_xZn_{1-x}O$ JUNCTIONS

5.1 Introduction

Transparent conducting oxides (TCOs) are widely used as metallic electrodes for various display devices and solar cells [5-1]. However, there is little application based on its compound semiconductor property. Most active functions in semiconductors come from the characteristic properties of p-n junctions. TCO semiconductors are much preferable for the fabrication of p-n junction used as UV-detectors because they are transparent in visible and near UV-light region. Besides, they are environmental friendly as well as thermally and chemically stable [5-2].

At the present moment p-type conducting c-MZO is not ready (work under another project). All oxide transparent p-n junctions in this work will base on p-type $Li_{0.15}Ni_{0.85}O$ (LNO). NiO is a well-known transparent p-type semiconductor with a band gap of about 3.7eV. It has a rock salt cubic structure and a weak absorption band due to d-d transition of $3d^8$ electron configuration in the visible region [5-3, 5-4]. Li^+ doping could significantly boost p-type conductivity [5-5]. ZnO is a typical n-type TCO and a potential alternative to replace indium tin oxide (ITO). It is also a wide bandgap photonic material analogous to GaN. It has a hexagonal wurtzite-type structure with a direct band gap of 3.3eV and an excitonic binding energy of ~60meV, much larger than the ~25meV of GaN [5-6, 5-7].

In this project, p-$Li_{0.15}Ni_{0.85}O$/n-Nb-STO, p-$Li_{0.15}Ni_{0.85}O$/n-ZnO and p-$Li_{0.15}Ni_{0.85}O$/n-In-$Mg_xZn_{1-x}O$ heterostructures have been fabricated by PLD on sapphire and MgO substrates with Pt contacts on the LNO films. The combined use of TCOs to form a p-n junction represents a promising approach to realize low-cost and optically transparent junctions. Indeed, our present investigation has shown that such heteroepitaxial junctions are promising possibilities for inexpensive and transparent electronics for a wide variety of applications.

5.1.1 Working mechanism of all-oxide p-n junction [5-8]

The working principle of all-oxide p-n junction is similar to that of conventional semiconductor junction. A characteristic property of a p-n junction is that the electric current can pass through it much more readily in one direction than in the other. The p-type semiconductor and n-type semiconductor possess different Fermi levels. When these two materials are brought together, electrons diffuse from the n-region into the p-region because of the relatively high concentration in n-type material; at the same time holes tend to diffuse from the p-region into the n-region. This process continues until the Fermi levels line up. The diffusion electrons and holes recombine in the transition region. As a result, the n-region acquires a net positive charge and p-region acquires a net negative charge in the transition region, and then a potential gradient is created. This transition region is a space-charged region, for fewer mobile carriers exist in this region.

Three situations can occur:

1. No bias. Electron-hole pairs are created spontaneously by thermal excitation in the valence band of the p-region. Some of the electrons have enough energy to jump the gap to the conduction band and then migrate to the n-region. There they lose energy in collisions. At the same time, some electrons in the n-region are sufficiently energetic to climb the energy hill and enter the p-region, where they recombine with holes there. At thermal equilibrium the two processes occur at the same low rate, so there is no net current.

2. Forward bias. In this situation, an external voltage, V_e, is applied with the p end of the diode positive and the n end negative. The energy difference across the junction is now less by V_e than that of no bias situation, which increases the recombination current since the electrons have a smaller energy hill to climb. Under these circumstances, new holes are created continuously by the removal of electrons at the positive terminal while new electrons are added at the negative terminal. The holes migrate to the n-region and the electrons to the p-region under the influence of the applied potential. The holes and electrons meet in the vicinity of the p-n junction and recombine there.

3. Reverse bias. Under a reverse biased condition, the potential barrier is enlarged. The proportion of diffusion current is largely reduced and can be neglected. This is called the saturation current.

5.1.2 Ohmic contact

All semiconductor devices need contacts in which the electrons can easily flow in both directions. They are called ohmic contacts because their current-voltage characteristic obeys ohm’s law. It allows the injection of a current into and out of the semiconductor without suffering a sizable power loss.

5.1.3 Literature review on all-oxide p-n junction

Recent work that directly made use of the semiconducting properties of oxides is found in all-perovskite ferroelectric field effect transistor(FeFET), in which the semiconducting channel of the transistor is provided by a perovskite oxide instead of Si[5-9, 5-10, 5-11]. Atsushi Kudo et.al. [5-12, 5-13] have also grown polycrystalline n-ZnO/p-$SrCu_2O_2$ semiconducting heterostructures in an attempt to obtain an UV light-emitting diode. Yukio Watanabe [5-14] has found diode characteristics in ferroelectric/n-type and p-type oxide semiconductors junctions in his studies of carrier transport in ferroelectric. A most direct effort to fabricate an all oxide p-n junction was reported by M.Sugiuga et. al. [5-15, 5-16] in 1999. They have succeeded in fabricating p-i-n diodes with good rectifying properties by growing p-$La_{0.85}Sr_{0.15}MnO_3$/i-$SrTiO_3$/n-$La_{0.05}Sr_{0.95}TiO_3$ heterostructure on (100) $SrTiO_3$ substrate. Nakasaka and his groupmates [5-17] also successfully fabricated a p-i-n junction with the combination of p-$La_{0.95}Sr_{0.05}MnO_3$/i-$BaTiO_3$/n-$La_{0.01}Sr_{0.99}TiO_3$ in 2001.

In 2002, an all-perovskite oxide p-n junction consisting of $La_{0.9}Ba_{0.1}MnO_3$ (LBMO) and $Sr_{0.99}La_{0.01}TiO_3$ (SLTO) was fabricated by Zhang et.al. [5-18]. This bi-layer junction maintained a good rectifying behavior at both room temperature and low temperature without inserting an insulating layer. Another good rectifying bi-layer junction was fabricated in 2003 by Tiwari et.al. [5-19] using p-$La_{0.7}Sr_{0.3}MnO_3$ and n-ZnO layers. Later on, a nearly temerature independent rectifying characteristic was revealed in a p-n junction consisting of oxygen deficient $La_{0.67}Ca_{0.33}MnO_{3-\varphi}$ and Nb-doped $SrTiO_3$ by Hu et.al. in 2003[5-20]. Some distinct properties that affect the junction performance have been determined in later research. The colossal magnetoresistance (MR) effect and photovoltaic effect on the all-oxide junction performance were investigated by Tanaka et.al. [5-21] and Sun et.al. from 2002 to 2004[5-22, 5-23].

However, the work of all-oxide p-n junction is still at its infancy. In our study, several kinds of p-n junctions are investigated.

5.2 Fabrication of p-type and n-type thin films and p-n junctions

5.2.1 Deposition of p-type $Li_{0.15}Ni_{0.85}O$ on LAO substrates

NiO is a p-type conducting transition-metal oxide. Undoped NiO has very high resistivity. However, doping of divalent elements introduces extra positive charge carriers and hence increases the conductivity substantially. Lithium is chosen as the dopant in our study. With 15at% doping level of lithium, the insulating NiO film transforms to a conducting oxide material with a resistivity of about 1.4Ω-cm.

5.2.1.1 Fabrication and structural characteristics of $Li_{0.15}Ni_{0.85}O$ target

Standard solid state reaction was used to fabricate the $Li_{0.15}Ni_{0.85}O$ target. The condition for preparing the target was discussed and listed in Table 3.2. We use Li_2CO_3 and NiO as the starting materials. The weight amount of Li_2CO_3 and NiO are 0.831g and 9.524g respectively as shown in Table 3.1. The desired amount of powders were mixed with ethanol and ball milled for at least 10 hrs, then the mixture was dried in furnace and ground to fine powder by mortar. Calcinations at 1100°C and 1200°C were carried out to get rid of the carbon component and to initiate the chemical reaction. The calcinated powder was compressed by an oil-compressor at a pressure of 3.5 Ton into circular pellets of 2.5cm in diameter and 3 mm thick. Final sintering at 1400°C was then carried out to obtain the desired ceramic target. All the calcination and sintering process were performed in air and lasted for 10 hours at the desired temperature.

A structural characteristic of the as-prepared LNO laser ablation target was studied by XRD. Figure 5.1 shows the θ-2θ scan of the target. The reflection peaks were indexed according to the data defined by the database (ICDD International Centre for Diffraction Data). It is seen that the target is a single-phase compound. Lattice constant of the LNO target is calculated with 2θ values and hkl indices to be 4.14Å.

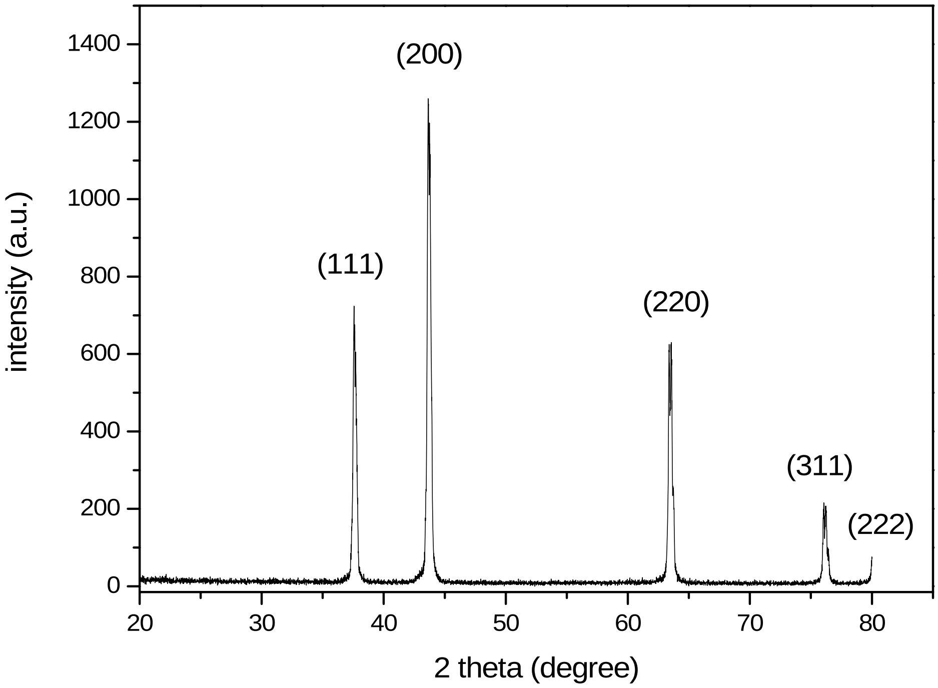

Figure 5.1 XRD θ-2θ scan of the $Li_{0.15}Ni_{0.85}O$ target.

5.2.1.2 Deposition and XRD structural characteristics of $Li_{0.15}Ni_{0.85}O$ film on LAO substrates

A 200nm thick $Li_{0.15}Ni_{0.85}O$ film was grown by PLD on LAO substrate using the homemade $Li_{0.15}Ni_{0.85}O$ target. The ablation light source was a Lambda Physik "Complex 205" KrF excimer laser (λ=248nm, repetition rate=10Hz, laser pulse energy=250mJ, fluence=5Jcm^{-2}). The deposition was carried out at a substrate temperature of 500°C and ambient oxygen pressure of 100mtorr. For growing of most oxide films, such as LSMO, YBCO and PZT, it is necessary to maintain an oxidizing environment during the deposition process in order to help form and stabilize the desired crystal phase. It is no exception for growing LNO. The relatively low deposition temperature of LNO, however is necessary to avoid excessive lithium evaporation. The as-grown LNO films were in situ annealed for 20min at 500°C and then allowed to cool down to room temperature.

The structural characteristic of $Li_{0.15}Ni_{0.85}O$ film has been studied and shown in Figure 5.2. θ-2θ scan shows strong peaks from the (h00) family planes of LNO and LAO. This clearly indicates a single phase and oriented LNO (100) film growth. The diffraction planes of LNO (200) and (400) are represented by two sharp peaks at 43.50° and 95.33°, respectively. Although the LNO (200) diffraction occurs at the same angle as that of LAO (200) CuKβ reflection, the strong LNO (400) reflection peak and the omega scan of LNO (200) plane suggests without doubt the existence of the LNO (200) reflection peak. The out-of-plane lattice constant of LNO is calculated to be about

4.16Å. LAO has a lattice constant of 3.79Å. Therefore there is a 9.7% lattice mismatch between LNO and LAO.

Figure 5.3 shows the rocking curves of LNO (200) and (400) peaks. The FWHM of these two planes are 0.98° and 0.85°, respectively. The orientation of LNO film is good even though there is a relatively large lattice mismatch between LNO film and the substrates.

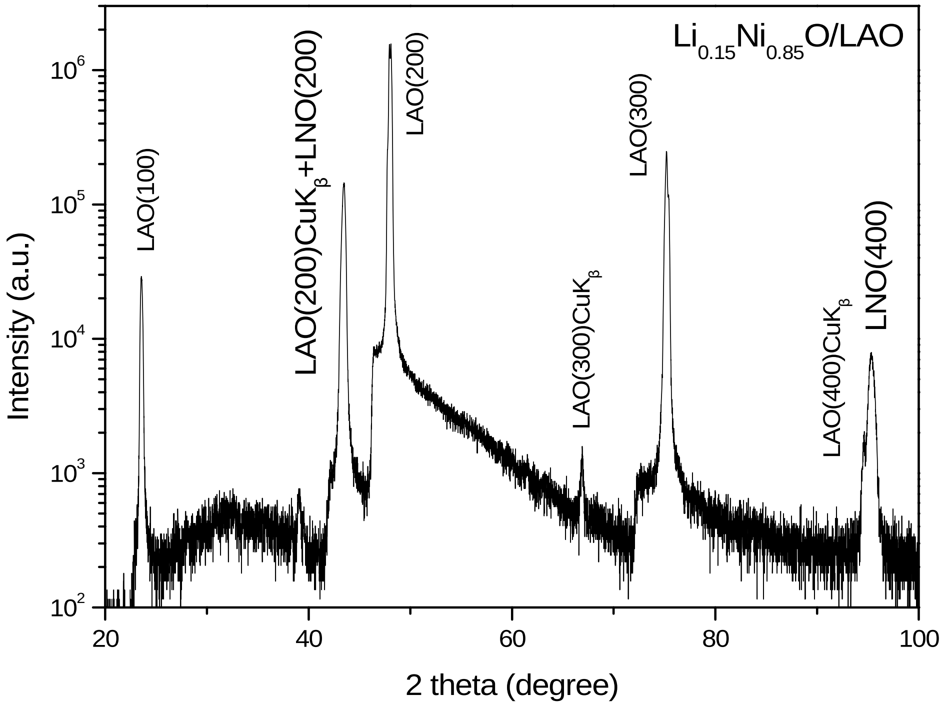

Figure 5.2 X-ray 2 theta diffraction pattern of the $Li_{0.15}Ni_{0.85}O$/LAO(100) film (pressure: 100mtorr; temperature: 500°C).

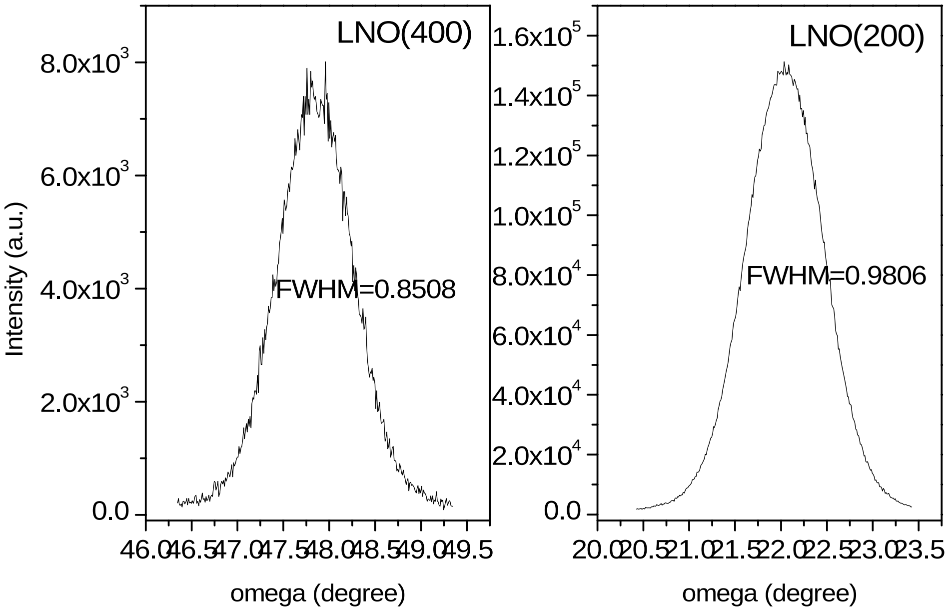

Figure 5.3 Rocking curves on the LNO (200) and (400) diffraction planes.

The (220) ϕ-scan profiles of the LNO film and LAO substrate are shown in Figure 5.4. The four-fold symmetric diffractions in the 360° ϕ-scans confirm the cubic structure of the film and substrate. Cube-on-cube epitaxial growth is verified by the matched ϕ angle reflections among the two scans.

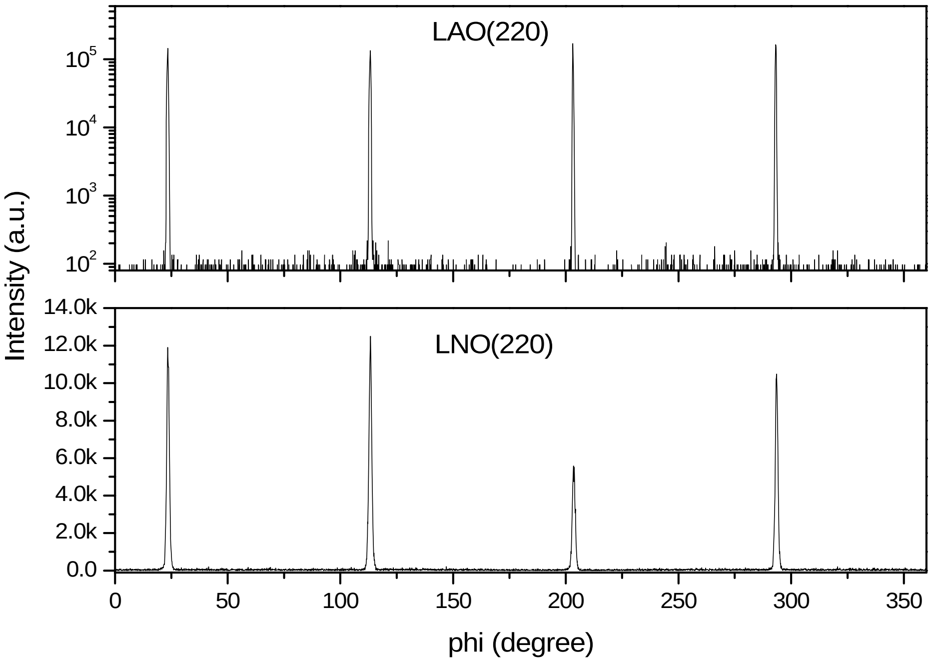

Figure 5.4 The XRD 360^0-ϕ scans on the LNO (220) and LAO (220) reflections.

5.2.1.3 Surface morphology of the single $Li_{0.15}Ni_{0.85}O$ film on LAO substrates

The surface morphology of LNO film was investigated by SEM. It has been mentioned that the generation of particulates is one of the major problem in PLD process. Presence of particulates on the deposited films could create additional paths for leakage current and lead to short circuit of the junction diode. Any particulates at the interface will disrupt the abrupt depletion boundary. Hence, the particulates will cause serious degradation on the junction performance and will destroy the rectify profiles of the junction. Figure 5.5 shows the surface morphology of a typical PLD deposited LNO film. Some particulates are observed. Nevertheless a very smooth surface without cracks and voids is obtained. Therefore, elimination of the particulates as much as possible seems to be necessary for obtaining efficient pn junctions. In our research group, we adopted a shadow mask in the PLD deposition process for growing the subsequent LNO thin film. A 1cm^2 square strainless steel mask is placed between the target and substrate in the vacuum chamber so that during the film deposition the macroparticles ejected from the target could be blocked off by the mask. On the other hand, small clusters and atomic/molecular species will drift and bend around the mask in accordance to the hydrodynamic flow of the plasma stream. Therefore the amount of the particulates on the film is reduced substantially. However the drawback of this shadow mask technique is a reduced deposition rate to about 1/3 of the original and perhaps a slight degradation of the crystallinity of the as-grown films. An appropriately longer deposition time is used at the present case for growth of films of needed thickness.

The SEM image of the surface of LNO film deposited by using the shadow mask is shown in the following section 5.3.2.2 in Figure 5.23(a). Comparing Figure 5.5 with Figure 5.23(a), the number of particulates is much reduced with this effective method.

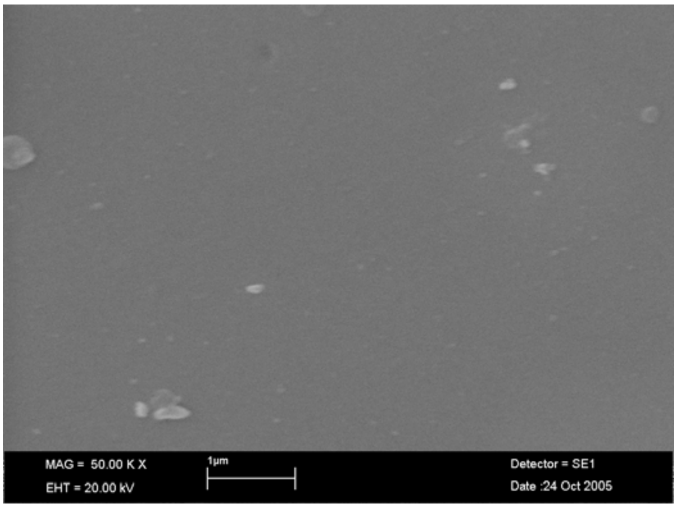

Figure 5.5 Scanning electron micrograph of surface of the $Li_{0.15}Ni_{0.85}O$ film on LAO substrate.

5.2.1.4 Electrical properties of $Li_{0.15}Ni_{0.85}O$ film

Figure 5.6 indicates the resistivity against temperature relationship of LNO film grown at 500°C and 100mTorr of ambient oxygen. The R-T plot of the LNO film is measured at temperatures from 300K-500K. Although the temperature range is small, a typical thermally excited charge carrier conduction is evident. The deposition temperature may alter the crystallinity quality and hence the conductivity of the film. From the figure, we could conclude that the resistivity of LNO decreases exponentially with the temperature, which suggesting a semiconducting like film. This is confirmed by the linear relationship in the logarithmic plot of resistivity against inverse temperature which is shown in the inset profile. The absolute resistivity is about 0.5Ωcm at room temperature. Therefore, we use this semiconducting LNO film as our p-type material to fabricate several kinds of all-oxide p-n junctions, which will be presented in late sections.

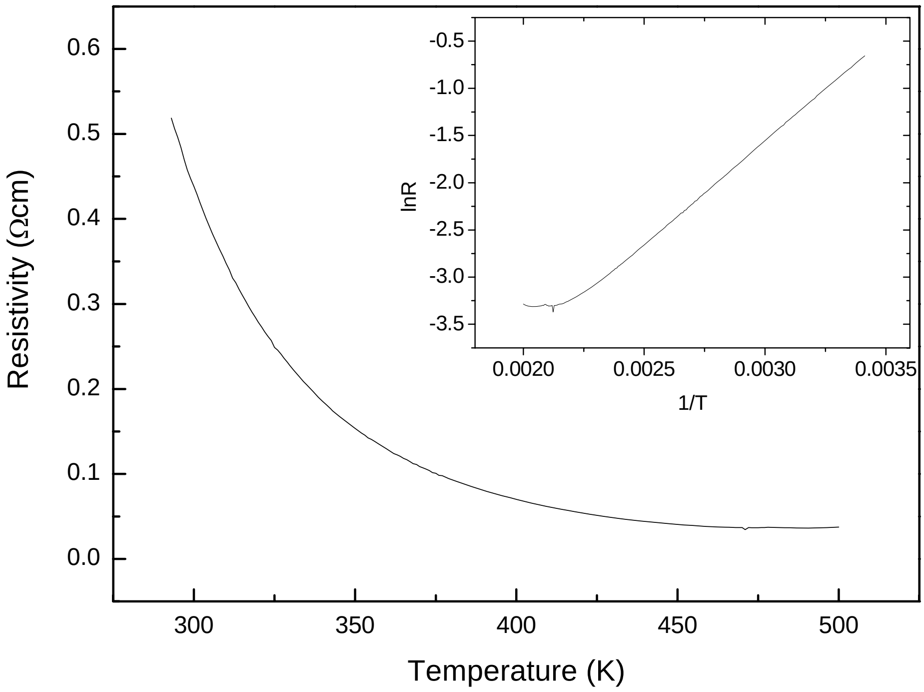

Figure 5.6 The resistivity against temperature relationship of LNO film. The inset shows the linear relationship in the logarithmic plot of resistivity against inverse temperature.

5.2.2 Deposition of n-type ZnO film on MgO (111) and Al_2O_3 (0001) substrates

ZnO based material is selected as a n-type semiconductor because it has many advantages: firstly, it is suitable for low temperature deposition, which helps to avoid chemical reaction of ZnO with p-type materials and damage of p-type materials during deposition. The second advantage is that the concentration of electron carriers is easily controlled by oxygen partial pressure during the deposition. This is necessary in order to match the carrier concentration with that of positive holes in p-type materials.

The ZnO target fabrication process, film deposition process, their related structure and electrical properties have been described previously in chapter 4.

5.2.3 Deposition of n-type In-$Mg_{0.5}Zn_{0.5}O$ films on LAO and MgO (100) substrates

Doping with other elements, such as Al and In, could decrease the resistivity of $Mg_xZn_{1-x}O$ system and change its energy bandgap. Al doped ZnO has been advanced into commercial TCO and is being used widely. K.Matsubara et. al. [5-24] successfully deposited Al-doped $Mg_xZn_{1-x}O$ transparent conducting films by PLD on glass substrates. They managed to obtain a low resistivity of $\rho \leq 1\times10^{-3}\Omega$cm and an average visible transmittance of higher than 90% in these films. However, Al doping tends to destabilize the cubic structure of our $Mg_xZn_{1-x}O$ system. In our project, we choose In as the doping element for our cubic $Mg_xZn_{1-x}O$ film in order to achieve n-type semiconduction. In_2O_3 is of cubic structure and it may help to retain cubic structure in In-doped $Mg_{0.5}Zn_{0.5}O$ films.

5.2.3.1 Fabrication and structural characteristics of In-$Mg_{0.5}Zn_{0.5}O$ target

Films deposited using two targets of different In contents were examined: 2.3at.% and 8at.%. In doped $Mg_{0.5}Zn_{0.5}O$ targets were prepared by mixing stoichiometric ratio of ZnO, MgO and In_2O_3 powders. The mixed powder was ground, pressed into a pellet, and sintered at 1350°C in air. Detailed experiment procedures and the list of required chemicals and weight data are discussed in chapter 3.

Structural characteristics of the as-prepared laser ablation targets were studied by XRD. Figure 5.7 depicts the θ-2θ scan profiles of the 8at.% In-doped $Mg_{0.5}Zn_{0.5}O$ target and the undoped $Mg_{0.5}Zn_{0.5}O$ target. As has been discussed in chapter 3, the $Mg_{0.5}Zn_{0.5}O$ target is a single phase compound. The hkl indices of the reflection peaks are labeled according to the ICDD international diffraction database. After adding In_2O_3 into the $Mg_{0.5}Zn_{0.5}O$ target, the system transforms to mixed phase compound. Besides the reflections that come from the single phase $Mg_{0.5}Zn_{0.5}O$ compound, other reflections from the cubic In_2O_3 phase also appeared.

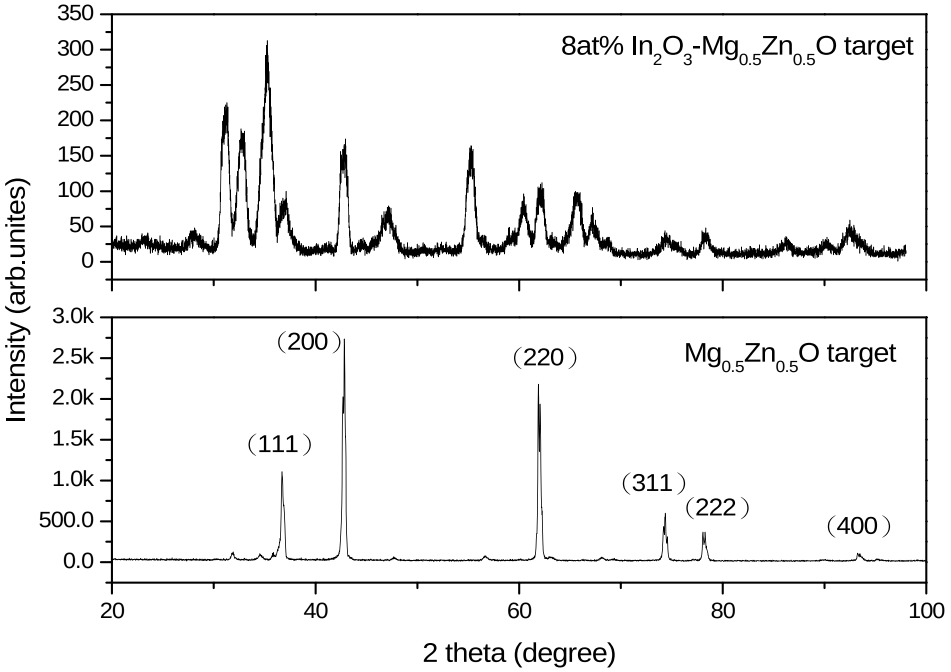

Figure 5.7 XRD patterns of the air-sintered targets from the mixture of stoichiometrical 8at.% In-doped $Mg_{0.5}Zn_{0.5}O$ and undoped $Mg_{0.5}Zn_{0.5}O$ compositions.

5.2.3.2 Deposition and structural characteristics of In-$Mg_{0.5}Zn_{0.5}O$ films grown on LAO and MgO (100) substrates

The In_2O_3 doped $Mg_{0.5}Zn_{0.5}O$ films were grown on LAO and MgO(100) substrates using the homemade target with a deposition temperature at 650°C and under a base vacuum of $\sim 3\times10^{-5}$ Torr obtained by a diffusion pump. The deposition conditions and vacuum chamber are same as those of the preparing undoped $Mg_xZn_{1-x}O$ films. The target was ablated by the KrF excimer laser (wavelength λ=248nm, Lambda Physik, Complex 205, pulse frequency=10Hz, fluence=~5Jcm^{-2}, laser pulse energy=250mJ) for 30min and subsequently the deposited films were annealed in situ for 20 minutes while keeping the deposition conditions. Then the films were naturally cooled to room temperature at the base pressure. The resulted film thickness is 300-400nm.

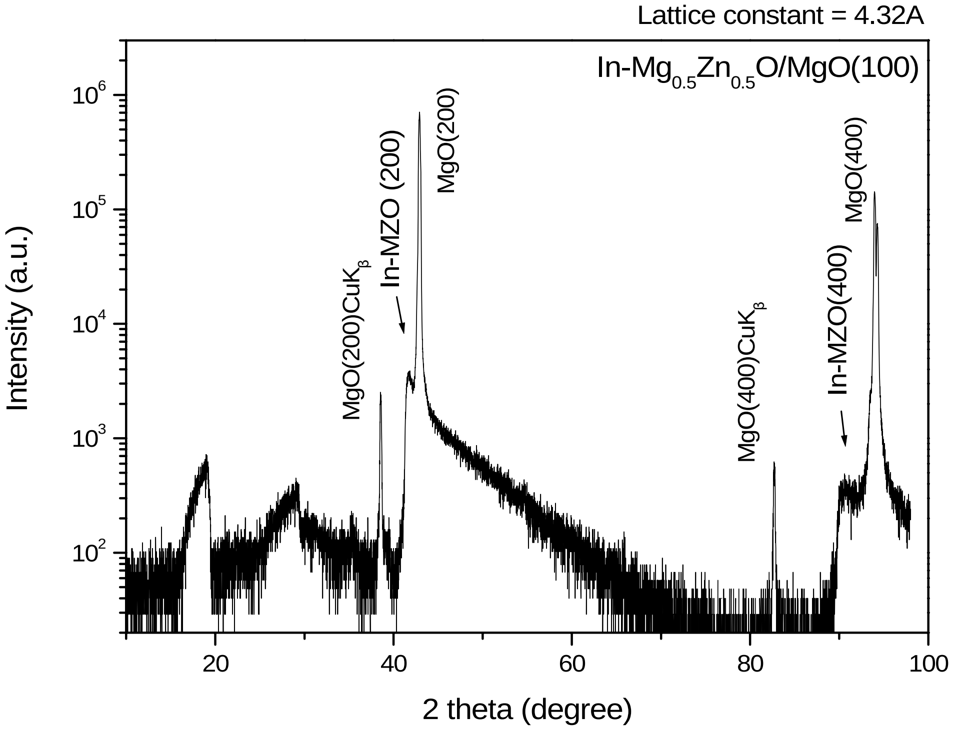

Figure 5.8 XRD 2 theta scan of 8at.% In-doped $Mg_{0.5}Zn_{0.5}O$/MgO(100) film (pressure: 3x10^{-5} torr; temperature: 650°C).

The structural characteristic of In-$Mg_{0.5}Zn_{0.5}O$ film has been studied. XRD diffraction peaks from the (h00) family planes of the In-$Mg_{0.5}Zn_{0.5}O$ film and MgO substrate are shown in Figure 5.8. Single phase and highly oriented In-MZO(100) growth film is evident. The diffraction planes of In-MZO (200) and (400) are clearly separated from the MgO(200) and (400) planes. This phenomenon is different from the undoped MZO films deposited on MgO substrate, in which the c-MZO(h00) diffraction planes overlaps with MgO(h00) planes because of the similar lattice constants of MZO (4.23Å) film and MgO (4.24Å) substrate. The out-of-plane lattice constant of In-MZO is calculated to be about 4.32Å, and there is a 1.9% lattice mismatch between In-MZO and MgO substrate. The enlarged crystal structure of In-MZO is primarily due to the addition of large In ions into MZO.

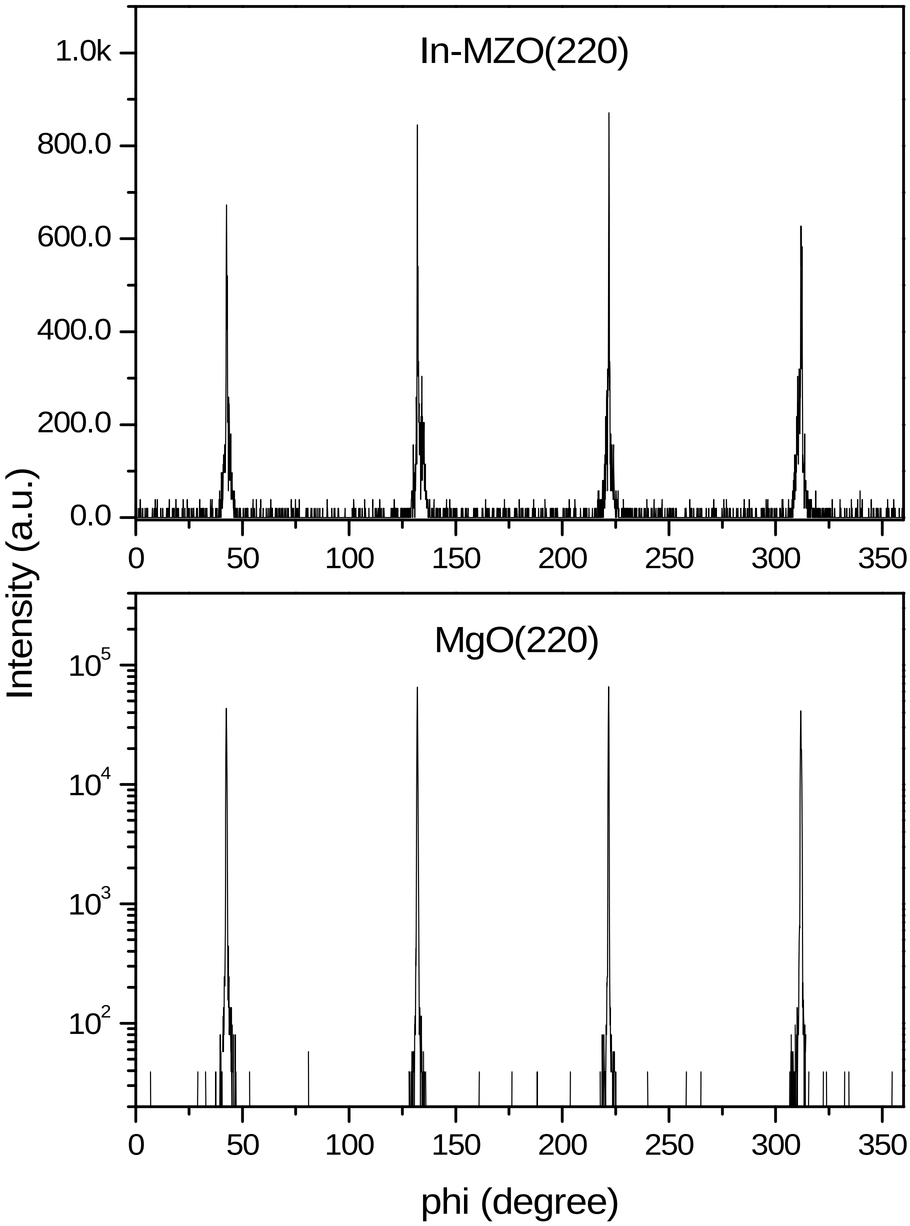

Figure 5.9 360^0-ϕ scans on the 8at.% In-doped $Mg_{0.5}Zn_{0.5}O(220)$ and MgO(220) reflections.

The 360^0-ϕ scans on the 8at.% In-doped $Mg_{0.5}Zn_{0.5}O(220)$ and MgO(220) reflections are shown in Figure 5.9. Cube-on-cube hetero-epitaxial growth of In-MZO film on MgO substrate is confirmed by the presence of four-fold symmetric diffractions and matched ϕ angle reflections among the two scans.

5.2.3.3 Electrical properties of In-$Mg_{0.5}Zn_{0.5}O$ film

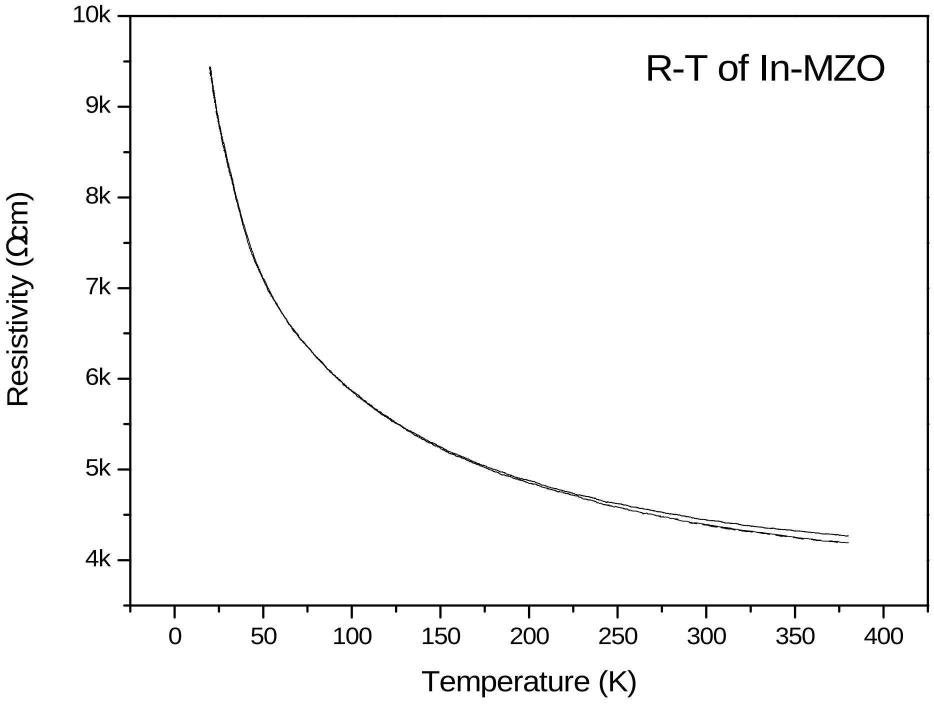

Figure 5.10 The resistivity against temperature relationship of 8at.% In-doped $Mg_{0.5}Zn_{0.5}O$ film.

A simple two point probe method is used for the R-T measurement of In-MZO film grown at substrate temperature of 650°C and under an ambient pressure of

3×10^{-5}Torr. The profile is indicated in Figure 5.10. In our study, undoped $Mg_xZn_{1-x}O$ films possess large resistivity and could not be used as n-type materials in the fabrication of p-n junctions. Indium doping decreases the resistivity of $Mg_xZn_{1-x}O$ films quite substantially. The R-T relation not only displays the temperature dependence of the absolute resistivity but also yields useful information on the conduction mechanism, that is, the metallic-like conduction or the semiconducting-like conduction. The In-MZO film exhibits resistivity of about several kΩcm from 20K to 380K. The resistivity decreases with temperature, suggesting a semiconducting-like conduction mechanism. In later sections, p-n junctions with the use of this In-MZO n-type semiconducting film will be described.

5.3 Fabrication and characterization of p-n junctions

5.3.1 Fabrication and characterization of LNO on Nb-1wt.% doped $SrTiO_3$ substrates

5.3.1.1 Introduction

Commercial Nb-1wt.% doped $SrTiO_3$ (NSTO) single crystal substrate is a conducting n-type material. Hence an all oxide p-n junction could be obtained by simply growing a p-type oxide material on the top of NSTO substrate. We first tried to deposit epitaxial LNO thin film on single crystal NSTO substrate to fabricate an all oxide p-n junction. The LNO film is patterned by a 2-dimensional arrays of

2mm×0.5mm mask by PLD technique on NSTO. The deposition process is performed under a substrate temperature of only 500°C to avoid excessive lithium evaporation. An ambient oxygen pressure of about 100mTorr was used. The laser ablation and film deposition processes lasted for 20min. The as-deposited LNO film was then in situ post-annealed for 10min at the same deposition condition to enhance crystallinity. It was then allowed to cool down to room temperature. Pt electrodes were grown on both the LNO film and NSTO substrate to form good ohmic contact. The schematic side view of these p-n junctions is shown in Figure 5.11.

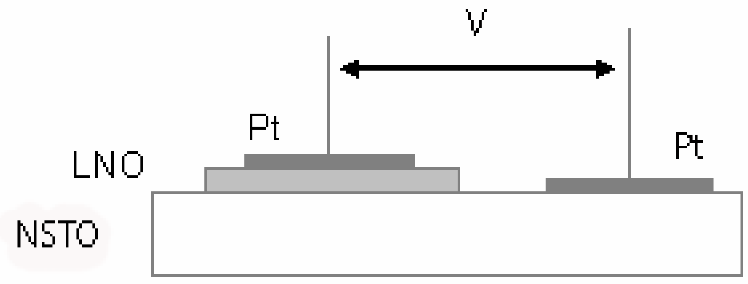

Figure 5.11 Schematic side view of the p-$Li_{0.15}Ni_{0.85}O$/n-NSTO heterojunction diode.

5.3.1.2 XRD structural characteristics

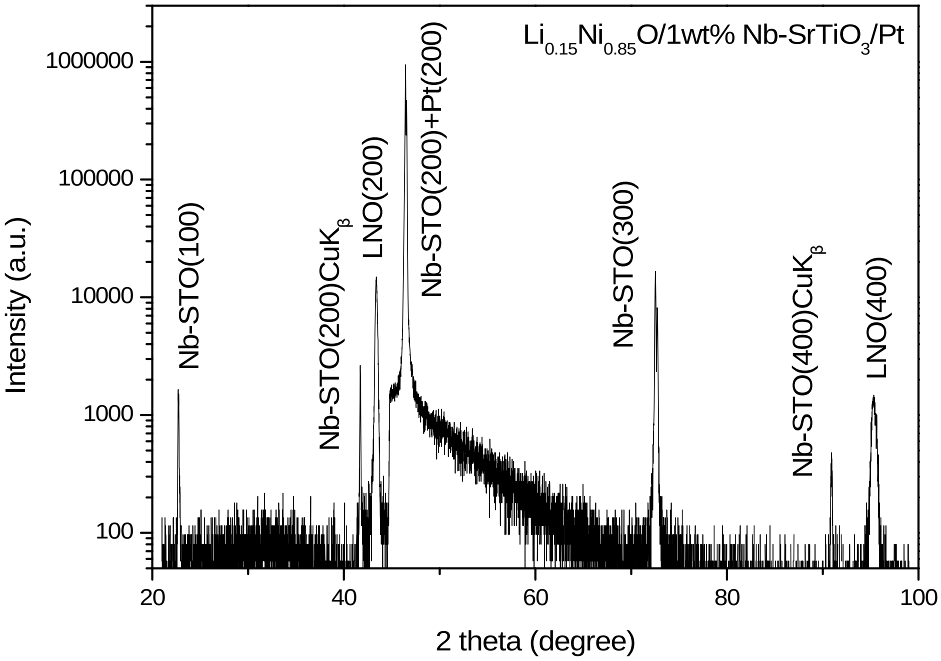

Figure 5.12 XRD 2 theta scan of $Li_{0.15}Ni_{0.85}O$ film grown on single crystal Nb-1wt.% doped $SrTiO_3$ (100) substrate.

The XRD θ-2θ patterns of the $Li_{0.15}Ni_{0.85}O$ film grown on NSTO(100) substrate by PLD is shown in Figure 5.12. Reflection planes of single phase and oriented LNO, NSTO and Pt are observed. It is noted that only the diffraction peaks from the (h00) family of the planes are observed. The diffraction from planes of LNO (200) and (400) show up as two sharp peaks at 43.38° and 95.30°, respectively. These data correspond to a cubic LNO lattice constant of about 4.17Å. the structural properties of the LNO film thus obtained are almost the same as those of the LNO film grown on LAO substrate shown in Figure 5.2. The NSTO(200) plane diffraction occurs at the same angle as the Pt(200) reflection. The out-of-plane lattice constant of NSTO substrate and Pt electrode is calculated to be about 3.90Å. The lattice mismatch between LNO and NSTO is about 6.9%.

The FWHM of the rocking curves of LNO/NSTO film (200) and (400) plane diffractions are 0.69° and 0.63°, respectively. They are shown in Figure 5.13. Such narrow diffraction profiles suggest an excellent crystal grain orientation.

The epitaxial relationship between the LNO film and NSTO substrate was examined by XRD ϕ-scan, which not only gives the in-plane parameter of the sample but also the structural relation between the film and substrate. The ϕ-scans of LNO(220) and NSTO(220) reflection peaks are shown in Figure 5.14. Four characteristic peaks of LNO(220) plane are very sharp and their ϕ angles match with the peaks of NSTO(220) reflections. Cube-on-cube epitaxial growth is verified by the matched ϕ angle reflections among these scans.

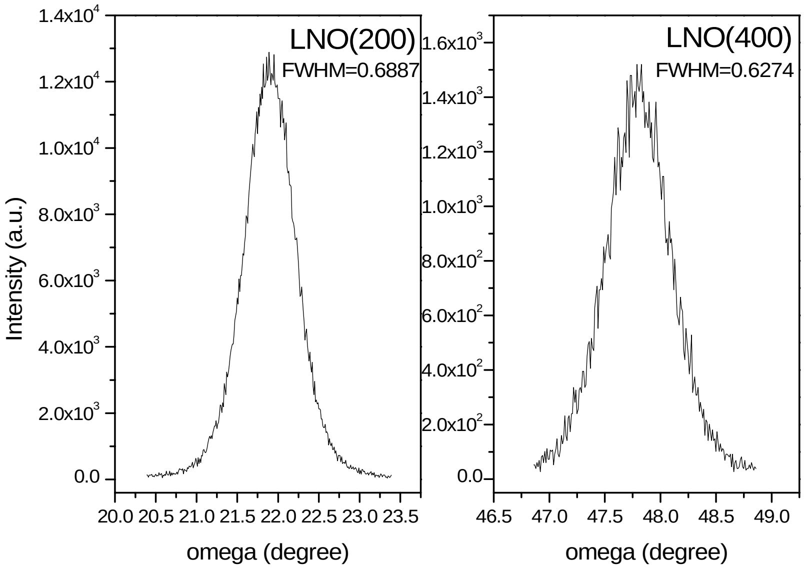

Figure 5.13 The rocking curves on the LNO(200) and (400) diffraction planes grown on NSTO(100) substrate.

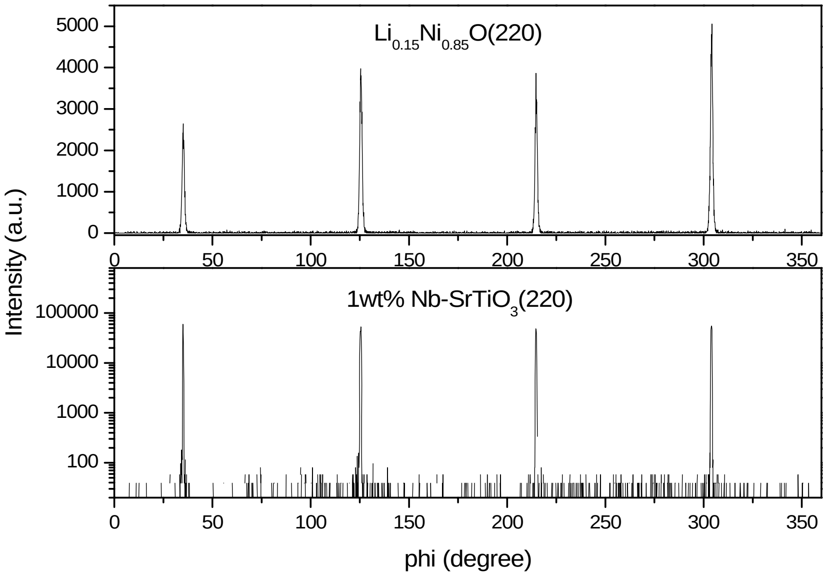

Figure 5.14 360^0-ϕ scans on LNO(220) and NSTO(220) reflections.

5.3.1.3 I-V characterization

Pt electrode is utilized as our conducting buffer layer to the external circuits in the oxide film or junction electrical measurements. The I-V characteristic of the Pt/$Li_{0.15}Ni_{0.85}O$/Pt junction has been tested and is shown in Figure 5.15. Linear relationship traversing the origin confirms good ohmic contact of the junction. The resistance is calculated to be about 42.6kΩ. Ohmic contact of the junction ensures that the rectifying effect from the subsequent I-V characteristic curves come from the all oxide-oxide junction only but not from the Pt-oxide junction.

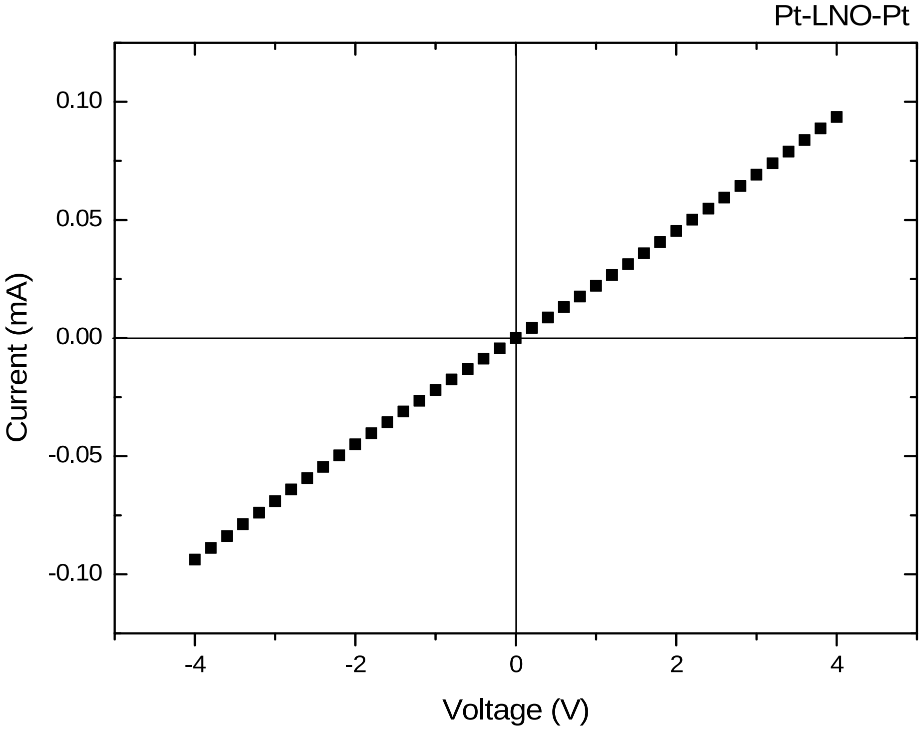

Figure 5.15 I-V characteristic of Pt/$Li_{0.15}Ni_{0.85}O$/Pt junction.

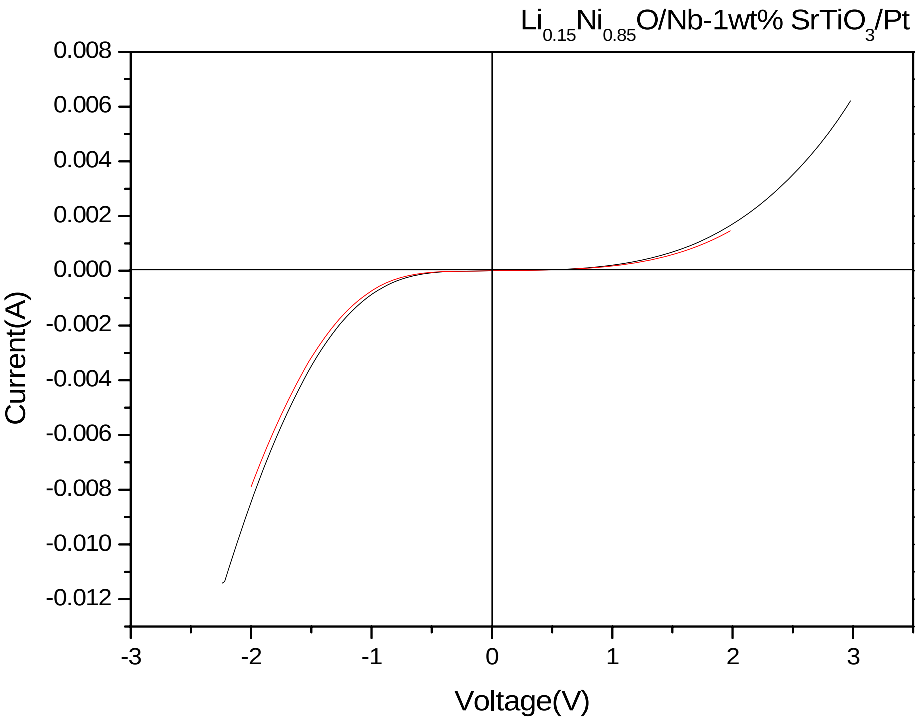

Figure 5.16 Typical I-V characteristics of the p-$Li_{0.15}Ni_{0.85}O$/n-Nb-$SrTiO_3$ heterojunction diode at room temperature.

Figure 5.16 shows the I-V characteristic of the p-$Li_{0.15}Ni_{0.85}O$/n-Nb-$SrTiO_3$ heterojunction. A typical diode rectifying profile is obtained. In the forward biased region, the turn-on voltage of the junction is about 0.8V. However, the junction exhibits a large leakage current under the reverse bias. It indicates a narrow depletion layer between the p-type LNO and n-type Nb-STO layers. The created depletion layer is expected to be very narrow and hence the tunneling current is very large because the p-LNO film and n-Nb-STO substrate are highly conducting semiconductors. The resistance of Nb-STO substrate is tested to be about several Ω and the profile is not shown here. Hence, the minority charge carrier could tunnel through the depletion layer easily under the reverse biased condition.

Figure 5.16 presents two I-V characteristics of two junctions with different conducting path distance along the substrate, giving two different series resistance values in the measurements. The profiles appear almost the same except a slight difference due to the varying measurement distance and hence the different resistance of the two junctions. The unequal series resistance of the p-LNO and n-Nb-STO oxide layers is held responsible. By measuring different distance, the two junctions have their own Nb-STO resistances but same LNO resistances because of the junction's arrangement. The turn-on voltages and the slopes of the linear region of the two curves appear to be more or less the same because of the same thickness of the depletion layer. Hence, we could conclude that the change in n-type substrate resistance could give a little effect on the series resistance and rectifying profile of the junction.

In order to solve the problem of a narrow depletion layer formed between the p-LNO and n-Nb-STO oxide layers and to remedy the large leakage current, other groups and our group have tried to introduce a thin $SrTiO_3$(STO) insulating layer between these two layers to form a PIN hetero-structure. The STO layer could help broadening the transition region and hence lowering the transmission probability. The forward biased diffusion current however will be reduced by inserting this STO insulator. This STO layer of 250nm thick is sandwiched between the p-type and n-type layers. The I-V characteristic of the LNO/STO/Nb-STO junction is shown in Figure 5.17. It is obvious that the large leakage current is much reduced compared with that shown in Figure 5.16. At the same time, a larger turn-on voltage of about 1.1V is obtained.

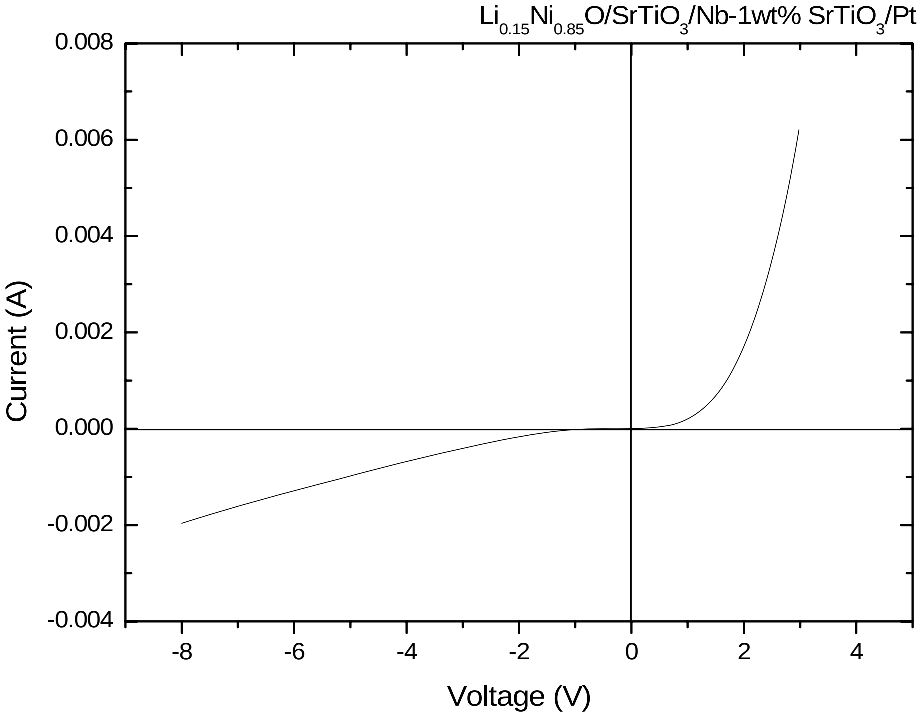

Figure 5.17 I-V characteristics of the $Li_{0.15}Ni_{0.85}O/SrTiO_3/Nb-SrTiO_3$ heterojunction diode at room temperature.

5.3.2 Fabrication and characterization of p-$Li_{0.15}Ni_{0.85}O$/n-ZnO junctions on Al_2O_3 (0001) and MgO(111) substrates

5.3.2.1 Introduction

We have fabricated the all-transparent-oxide p-n junction based on the p-type Li-doped NiO and n-type ZnO films on sapphire and MgO(111) substrates with Pt contacts on the LNO and ZnO films. This involves a combined use of TCOs to form a p-n junction and represents a promising approach for realizing low-cost and optically transparent junctions.

For the ZnO film deposition, the chamber was evacuated by a cryopump to a base pressure of 4×10^{-5}torr. The growth temperature was kept at 650°C, which has been mentioned in chapter 3. After deposition the film was annealed and then naturally cooled to room temperature at the base pressure. Then the LNO film was deposited on the ZnO film through a patterned mask to form arrays of 0.5mm×0.5mm square patches. The substrate temperature was fixed at 500°C and the chamber was filled with pure oxygen gas to a pressure of 100mtorr. The LNO film was in-situ annealed for 20min at 500°C and then allowed to cool down to room temperature. Pt electrodes were grown on both the ZnO and LNO films to form good ohmic contact. The schematic side view of these p-n junctions is shown in Figure 5.18.

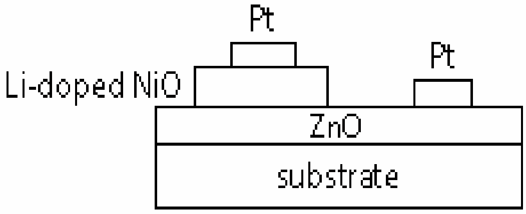

Figure 5.18 Schematic side view of the p-$Li_{0.15}$ Ni $_{0.85}$O/n-ZnO heterojunction diode.

5.3.2.2 XRD studies of structural characteristics and SEM surface morphology of p-$Li_{0.15}Ni_{0.85}O$/n-ZnO junctions on Al_2O_3 (0001) substrates

Despite the different crystal structures of ZnO(Wurtzite, hexagonal) and LNO(Rock salt, Cubic), a high-quality LNO epitaxial layer could be grown on a single-crystalline ZnO due to the similar oxygen atomic configurations(sixfold symmetry) of (0002)ZnO and (111) LNO (domain matched epitaxy)[5-25]. Al_2O_3 (0001) and MgO(111) substrates were chosen as the junction template to fabricate hexagonal epitaxy ZnO films. Lattice constants and mismatch data have been calculated and listed in Table 2.2.

The crystalline quality and mutual orientations of the bi-layer heterojunction LNO/ZnO were analyzed by XRD technique with a four-circle diffractometer (Philips X'pert). The transmission measurement of the films was carried out on a UV–VIS series spectrometer. The junction morphology was investigated by SEM. The rectifying property of these junction diodes was measured at room temperature.

Figure 5.19 presents the intense XRD diffraction peaks of ZnO(0002), LNO(111), Pt(111) and Al_2O_3 (0006) substrate of the out-of-plane pattern (synchronous scan of 2 θ and ω in the horizontal plane), which indicated that all the films were single phase and highly oriented on the Al_2O_3 (0001) substrate. The diffraction from the ZnO(0002) and (0004) planes are represented by the peaks at 33.87° and 72.08°, similar with the profile in Figure 4.25. The LNO(111) and (222) phase diffractions are fortuitously occurred at the same angle with the Al_2O_3 (0006) λ_β and (00012) λ_β reflections. Pt(111) and (222) diffraction planes are also indexed in the figure. It must be pointed out that Ni(111) peak is also appeared. This is due to some of the lithium evaporation under 500°C deposition temperature and excessive Ni atom was remained and deposited during the process. Ni(111) is also epitaxy grown on the bottom film and substrate.

Even though the different crystal structures and lattice mismatch between these films and substrate, the orientations of ZnO, LNO and Pt films remain good. The FWHM of the ZnO(0002) and (0004) planes, LNO(111) and (222) planes, Pt(111) and (222) planes and Ni(111) plane are shown in Figure 5.20 and Figure 5.21. All of the data are below 1° except that the Pt(111) plane possess a FWHM of 1.04°, suggesting excellent crystal grain orientations.

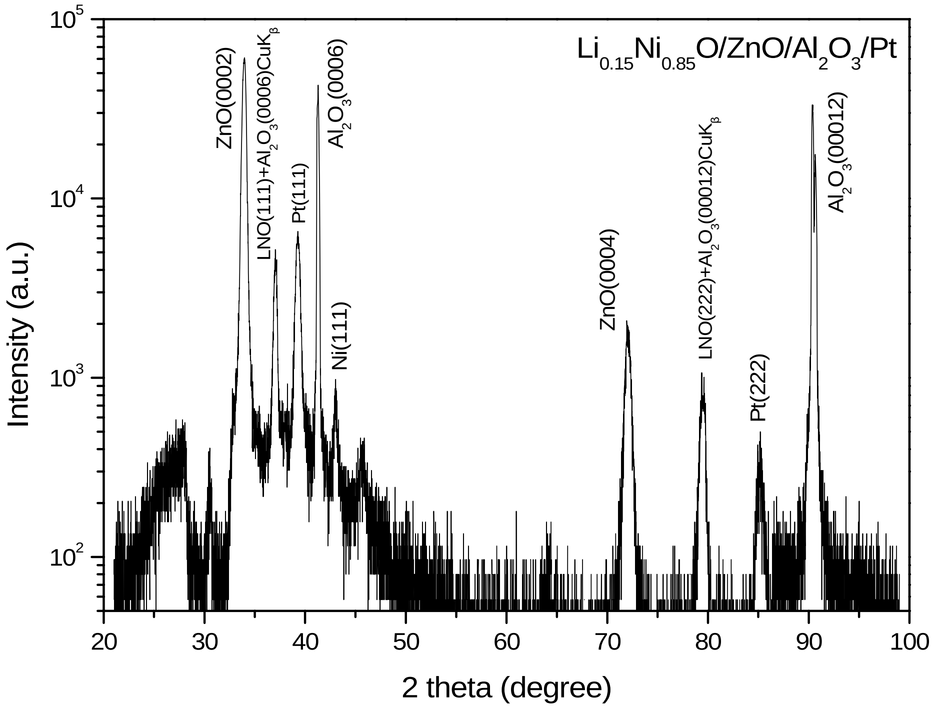

Figure 5.19 XRD 2 theta scan of p-$Li_{0.15}Ni_{0.85}O$/n-ZnO/Pt pn-heterojunction grown on Al_2O_3 (0001) substrate.

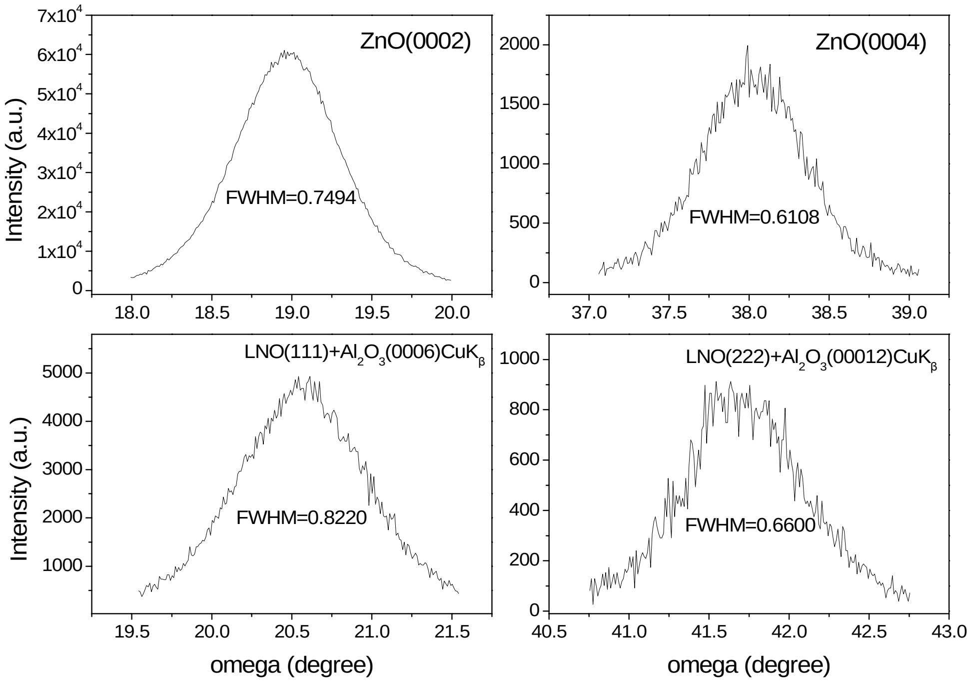

Figure 5.20 The rocking curves on the ZnO(0002), ZnO(0004), LNO(111) and LNO(222) diffraction planes of the p-$Li_{0.15}Ni_{0.85}O$/n-ZnO/Pt pn-heterojunction grown on Al_2O_3 (0001) substrate.

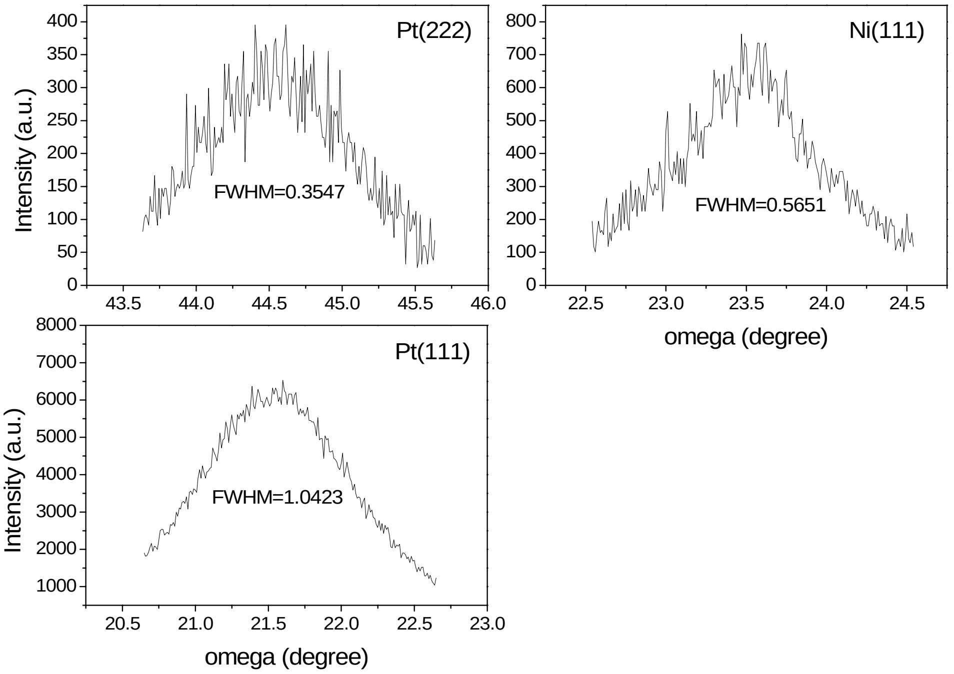

Figure 5.21 The rocking curves on the Pt(111), Pt(222) and Ni(111) diffraction planes of the p-$Li_{0.15}Ni_{0.85}O$/n-ZnO/Pt pn-heterojunction grown on Al_2O_3 (0001) substrate.

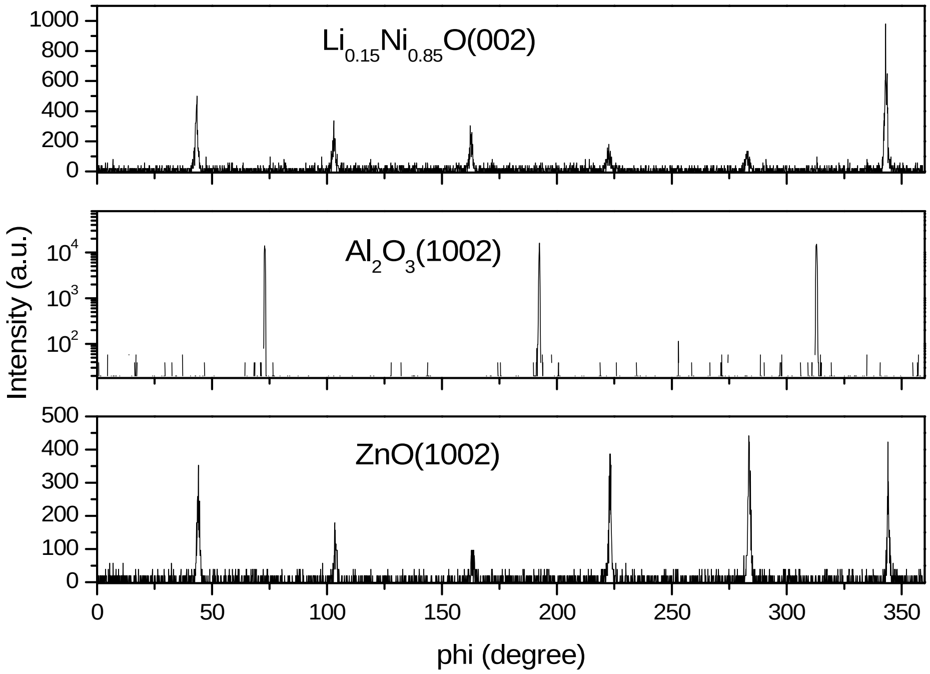

Figure 5.22 The XRD 360^0-ϕ scans on the LNO(002), ZnO(1002) and Al_2O_3(1002) reflections of the p-$Li_{0.15}Ni_{0.85}O$/n-ZnO/Pt pn-heterojunction grown on Al_2O_3 (0001) substrate.

Figure 5.22 shows the 360^0-ϕ scan profiles of the LNO layer, ZnO layer and the bottom Al_2O_3 substrate. The six-fold symmetric diffractions of ZnO(1002), three-fold symmetry in the diffraction profiles of Al_2O_3 (1002) and a 30° rotation between some planes of ZnO and Al_2O_3 confirm the epitaxy growth of ZnO film on sapphire with preferred c-axis orientation. Six characteristic peaks of LNO(002) plane are also appeared and the ϕ angles match with the peaks of ZnO(1002) reflections. Cubic epitaxial growth of LNO film on hexagonal ZnO film is also verified by the matched ϕ angle reflections among the scans. The epitaxial relationships between the three layer are concluded to be (111)LNO||(0001)ZnO||(0001)Al_2O_3 (out-of-plane) and (002)LNO||(1002)ZnO||(1002)Al_2O_3 (in-plane).

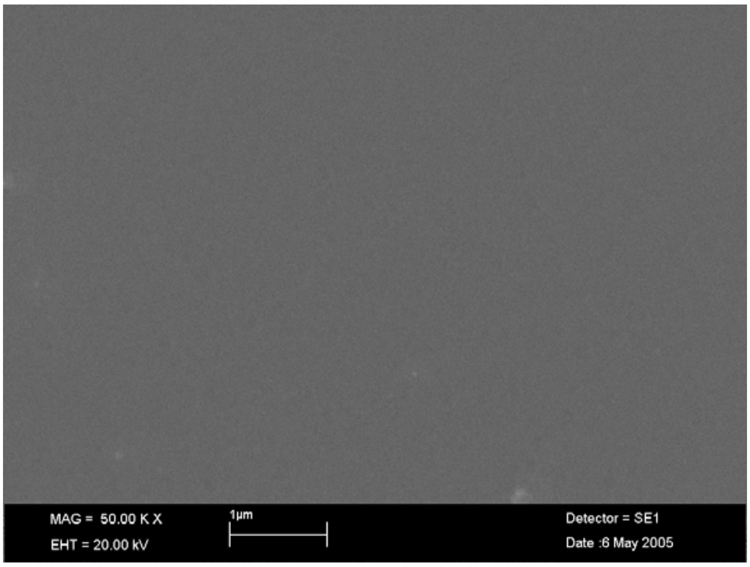

(a)

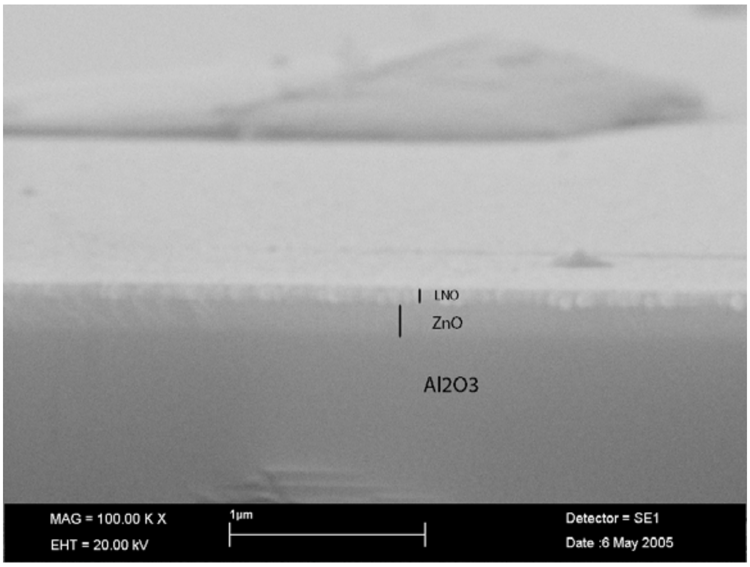

(b)

Figure 5.23 Scanning electron micrographs of (a) surface morphology of the p-LNO/n-ZnO heterojunction diode; (b) cross section of the p-n junction diode.

The surface morphology of the as-deposited junction diode is shown in Figure 5.23 (a). Smooth, featureless and crack-free layers are observed. Because the top layer of LNO was deposited by using the shadow mask technique, no obvious particulates were observed. The cross-section morphology (Figure 5.23(b)) reveals sharp junction boundary and layer thickness of about 200-300nm.

5.3.2.3 XRD studies of structural characteristics of p-$Li_{0.15}Ni_{0.85}O$/n-ZnO junctions on MgO(111) substrates

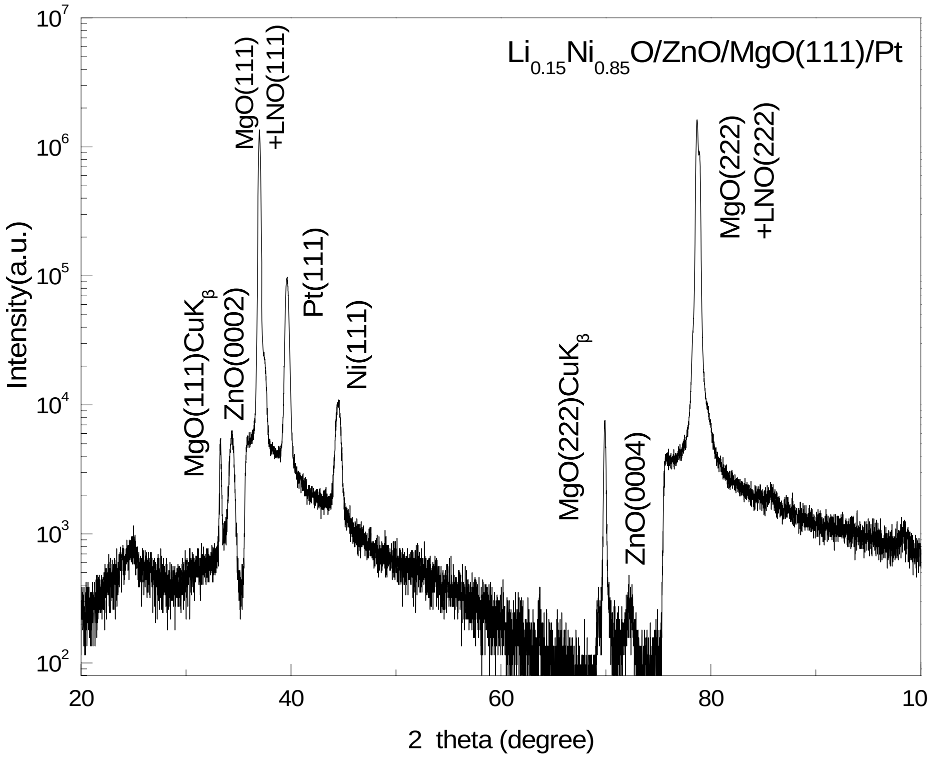

Figure 5.24 XRD 2 theta scan of p-$Li_{0.15}Ni_{0.85}O$/n-ZnO/Pt pn-heterojunction grown on MgO(111) substrate.

The p-$Li_{0.15}Ni_{0.85}O$/n-ZnO/Pt pn-heterojunction has also been fabricated on the MgO(111) substrate. The structural characteristic of this junction have also been inspected and described in Figure 5.24. Similar with the junction deposited on Al_2O_3 (0001) substrate, which is shown in Figure 5.19, intense XRD diffraction peaks of ZnO(0002), LNO(111), Pt(111), Ni(111) films and MgO(111) substrate of the out-of-plane pattern are observed, indicating all the films were single phase and highly oriented on the substrate. The diffraction from the ZnO(0002), ZnO(0004), LNO(111), LNO(222), Pt(111) and Ni(111) planes are represented by the peaks at the angles same with those of the planes deposited on Al_2O_3 (0001) substrate. The LNO(111) and (222) phase diffractions are fortuitously occurred at the same angle with the MgO(111) and (222) reflections. However the FWHM of LNO(111) and MgO(111) plane is 1.85°, which is much too large for single of MgO(111). The results thus confirm the existence of LNO(111) reflection plane. Furthermore, the FWHM of ZnO(0002), (0004) planes and Pt(111) plane are 1.8°, 1.64° and 1.25°, respectively. Indeed, ZnO, LNO and Pt films possess good crystal grain orientations in spite of the different crystal structures and lattice mismatch between these films and MgO substrate.

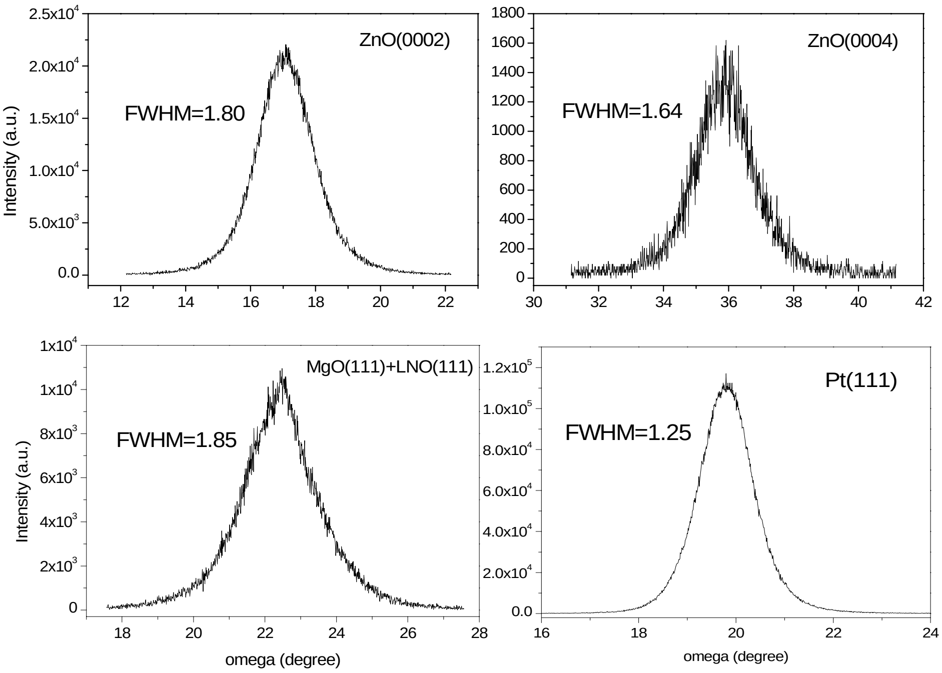

Figure 5.25 The rocking curves on the ZnO(0002), ZnO(0004), LNO(111) and Pt(111) diffraction planes of the p-$Li_{0.15}Ni_{0.85}O$/n-ZnO/Pt pn-heterojunction grown on MgO(111) substrate.

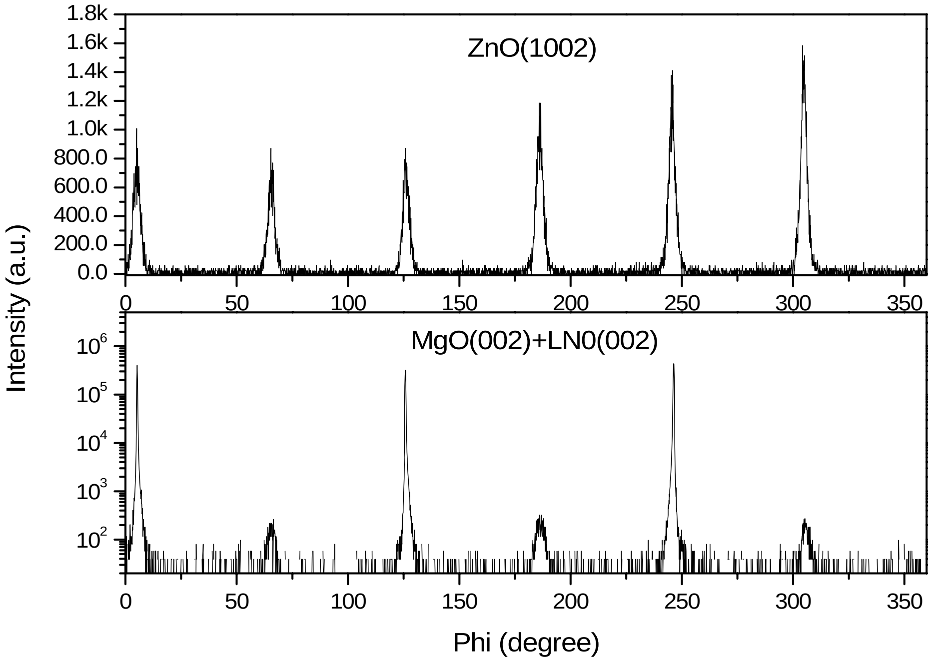

Figure 5.26 The XRD 360^0-ϕ scans on the LNO(002), ZnO(1002) and MgO(002) reflections of the p-Li$_{0.15}$Ni$_{0.85}$O/n-ZnO/Pt pn-heterojunction grown on MgO(111) substrate.

The 360^0-ϕ scan profiles of the LNO, ZnO films and the MgO substrate are shown in Figure 5.26. LNO(002) and MgO(002) planes are combined together because they possess same diffraction angles. In fact, three sharp symmetric peaks come from MgO(002) diffraction plane, while six symmetric peaks separated by 60° including three peaks covered by the intensive MgO(002) peaks are caused by the LNO(002) plane. The six-fold symmetric diffractions of ZnO(1002) and three-fold symmetry in the diffraction profiles of MgO(002) confirm the epitaxy growth of ZnO film on

MgO(111) with preferred c-axis orientation. The ϕ angles of six-fold symmetric diffractions of LNO(002) plane match with the peaks of ZnO(1002) reflections, which verifies the cubic epitaxial growth of LNO film on hexagonal ZnO film. The epitaxial relationships between the three layer are concluded to be (111)LNO||(0001)ZnO||(111)MgO (out-of-plane) and (002)LNO||(1002)ZnO||(002)MgO(in-plane).

5.3.2.4 Transmittance spectra of p-$Li_{0.15}Ni_{0.85}O$/n-ZnO junction

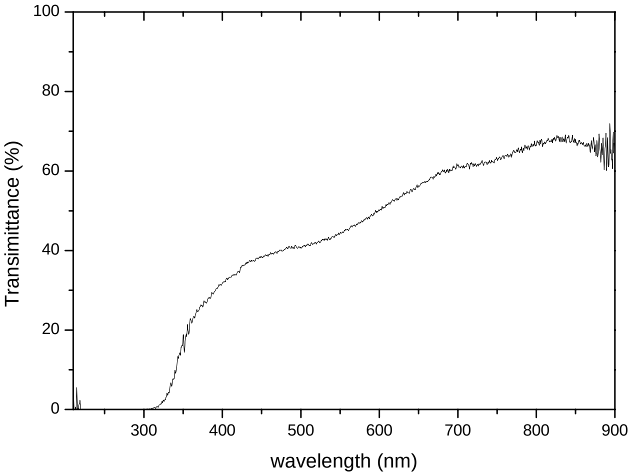

Figure 5.27 Optical transmittance spectrum of $Li_{0.15}Ni_{0.85}O$ film.

Figure 5.27 shows the optical transmittance spectrum of the p-type $Li_{0.15}Ni_{0.85}O$ film. The film keeps at about 60% transmittance in the infrared and visible region. The band gap energy is evaluated to be 3.57eV. P-$Li_{0.15}Ni_{0.85}O$/n-ZnO junction possesses a slightly lower transmission. The spectrum is not shown here. Optical transmittance spectrum and good I-V rectifying characteristics are obtained in this p-$Li_{0.15}Ni_{0.85}O$/n-ZnO/Pt heterojunction. Absorption occurs in the UV region, which suggesting this junction formed by transparent LNO and ZnO can be used as UV detectors and a possibility for inexpensive, transparent electronics in a wide variety of applications.

5.3.2.5 I-V characterization

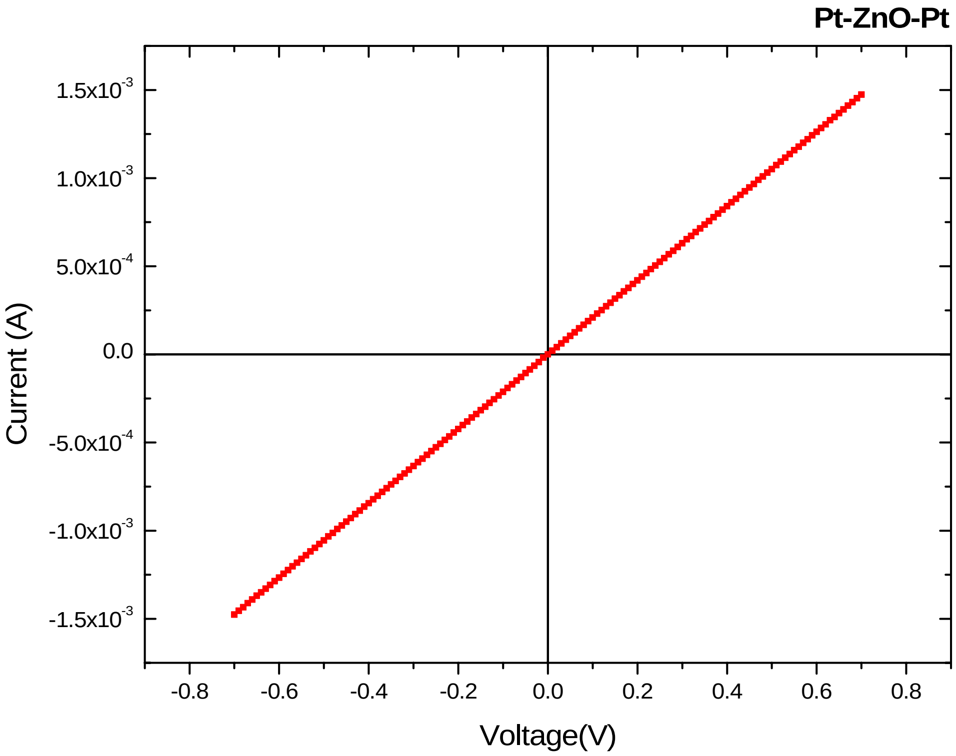

Figure 5.28 I-V characteristic of Pt/ZnO/Pt junction.

The I-V characteristic of the Pt/ZnO/Pt junction is shown in Figure 5.28. Good ohmic contact between ZnO and Pt layers is obtained. The resistance of our ZnO film is calculated to be about 470Ω. Ohmic contact of the junction ensures that the rectifying effect of the subsequent I-V characteristic curves comes from the p-$Li_{0.15}Ni_{0.85}O$/n-ZnO junction only but not from the Pt/ZnO/Pt junction.

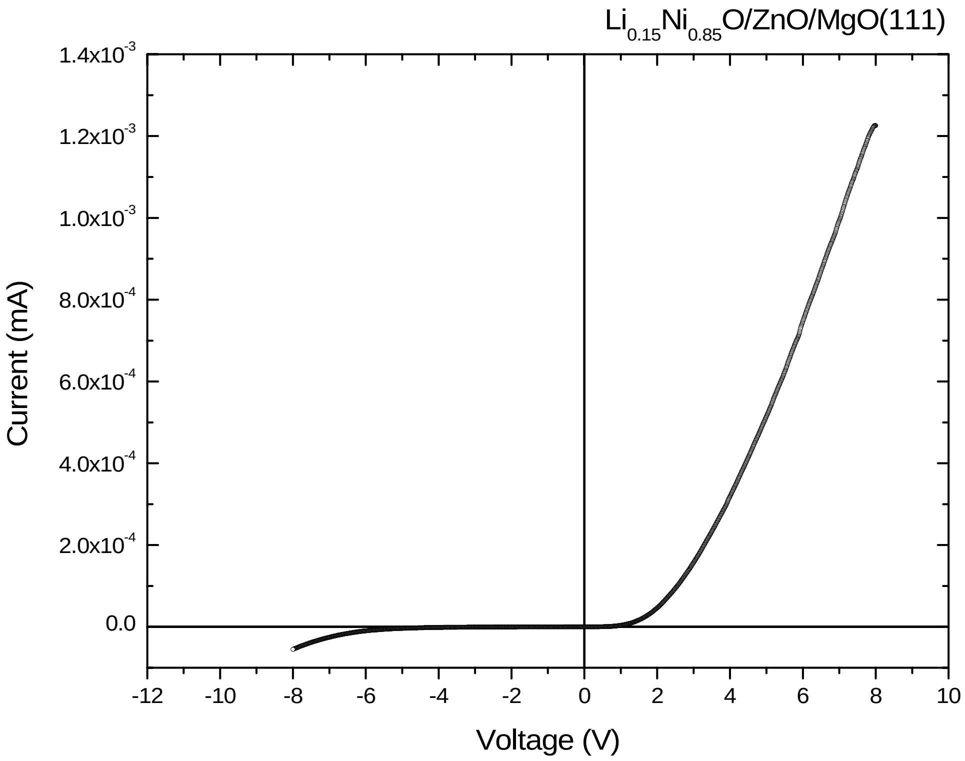

Figure 5.29 Typical I-V characteristics of the p-$Li_{0.15}Ni_{0.85}O$/n-ZnO heterojunction diode at room temperature.

Room temperature I-V characteristic curve of the junction is displayed in Figure 5.29. The heterojunction exhibits a good rectifying profile, showing a small leakage current and a large forward-based current. The turn-on voltage of this junction is about 1.0V.

5.3.3 Fabrication and characterization of p-$Li_{0.15}Ni_{0.85}O$/n-In-$Mg_{0.5}Zn_{0.5}O$ junctions on LAO(100) and MgO(100) substrates

5.3.3.1 Introduction

We have also fabricated the all-transparent-oxide p-n junctions based on the p-type Li-doped NiO and n-type In-$Mg_{0.5}Zn_{0.5}O$ films on LAO and MgO(100) substrates. The deposition conditions including substrate temperature and ambient oxygen pressure were discussed in previous sections. The laser fluence was kept to be about ~5Jcm^{-2}. This p-$Li_{0.15}Ni_{0.85}O$/n-In-$Mg_{0.5}Zn_{0.5}O$/Pt junction was patterned in the same way as the p-$Li_{0.15}Ni_{0.85}O$/n-ZnO/Pt junction. In-$Mg_{0.5}Zn_{0.5}O$ film was first deposited on LAO(100) or MgO(100) single crystal substrates. It was then followed by a layer of LNO deposited as a pattern of 2mm×0.5mm array via transmission through a stainless steel shadow mask. Platinum spots of 200μm diameter were deposited on top of both the LNO and In-MZO films. A sufficiently high substrate temperature could improve the electrode adhesion and create ohmic contact between the oxide films and the Pt electrode. Therefore Pt spot electrodes were deposited at substrate temperature of 300°C and ambient pressure of several mTorr. Figure 5.30 is the schematic side view of the p-$Li_{0.15}Ni_{0.85}O$/n-In-$Mg_{0.5}Zn_{0.5}O$/Pt junction on LAO and MgO substrates.

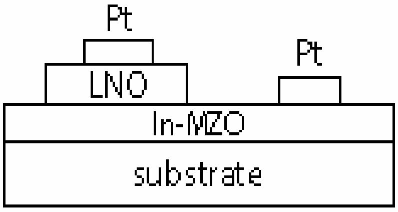

Figure 5.30 The schematic diagram of the p-$Li_{0.15}Ni_{0.85}O$/n-In-$Mg_{0.5}Zn_{0.5}O$/Pt junction.

5.3.3.2 XRD structural characteristics

The structural characteristics of single layer LNO and In-$Mg_{0.5}Zn_{0.5}O$ films were presented in the previous sections. In this section, we focus on the study of the bi-layer heterojunction. The XRD θ-2θ scan, ω scan and ϕ scan of the p-$Li_{0.15}Ni_{0.85}O$/n-In-$Mg_{0.5}Zn_{0.5}O$/Pt junction grown on LAO and MgO substrates have been obtained.

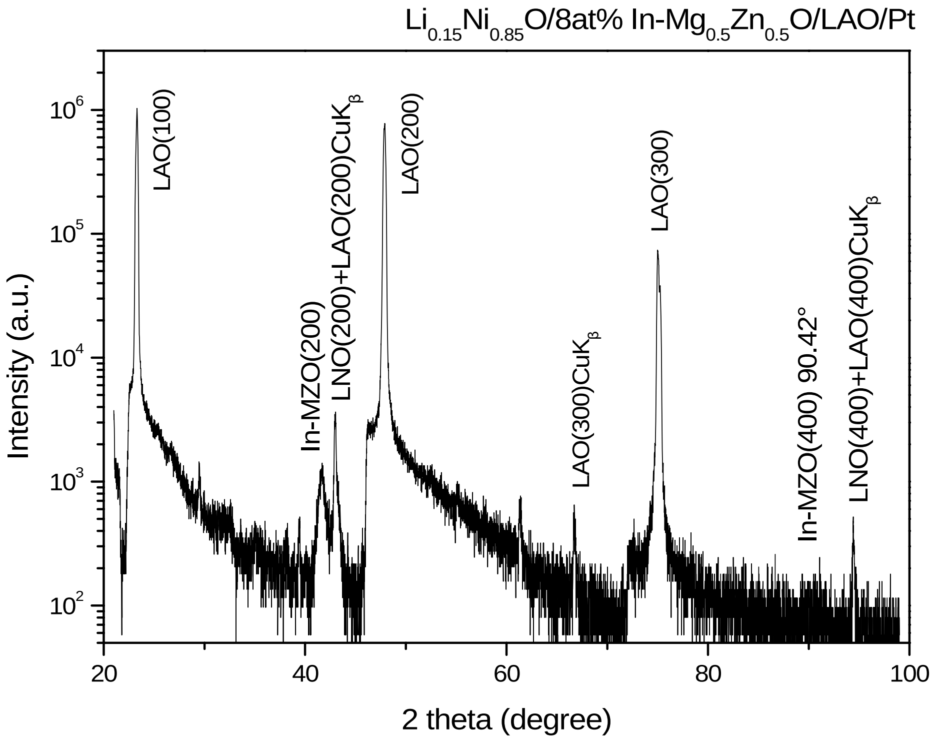

Figure 5.31 XRD 2 theta scan of p-$Li_{0.15}Ni_{0.85}O$/n-In-$Mg_{0.5}Zn_{0.5}O$/Pt pn-heterojunction grown on LAO(100) substrate.

Figure 5.31 shows the 2 theta pattern of LNO/In-MZO on LAO substrate. Cubic In-MZO(200) and LNO(200) diffraction peaks are found at the angles of 41.57° and 42.96°. The LNO(200) reflection coincides with the LAO substrate(200) CuK_β diffraction peak since the lattice constants of LNO and LAO are 4.16Å and 3.79Å, respectively. In this profile, the reflection peaks of LNO(400) and In-MZO(400) are too weak to be resolved. There are no XRD peaks other than those identified with (h00) families of LNO, In-MZO and LAO. This is a good indication that both of the layers are of single phase and c-axis oriented grown on LAO substrate.

The rocking curves of In-$Mg_{0.5}Zn_{0.5}O(200)$ and $Li_{0.15}Ni_{0.85}O(200)$ films are shown in Figure 5.32. The FWHM of In-$Mg_{0.5}Zn_{0.5}O$ is 1.674°, suggesting growth of reasonable well oriented In-MZO film. However, the LNO(200) peak is completely masked by the LAO(200) λ_β peak which shows a FWHM of 0.189°.

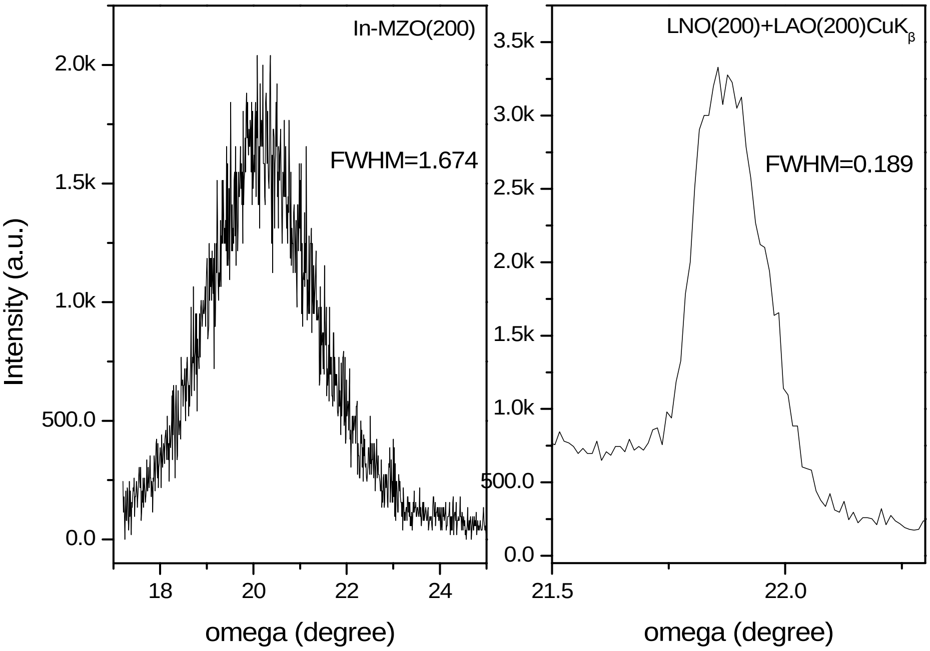

Figure 5.32 The rocking curves on the In-$Mg_{0.5}Zn_{0.5}O(200)$ and LNO(200) diffraction planes of the p-$Li_{0.15}Ni_{0.85}O$/n-In-$Mg_{0.5}Zn_{0.5}O$/Pt pn-heterojunction grown on LAO(100) substrate.

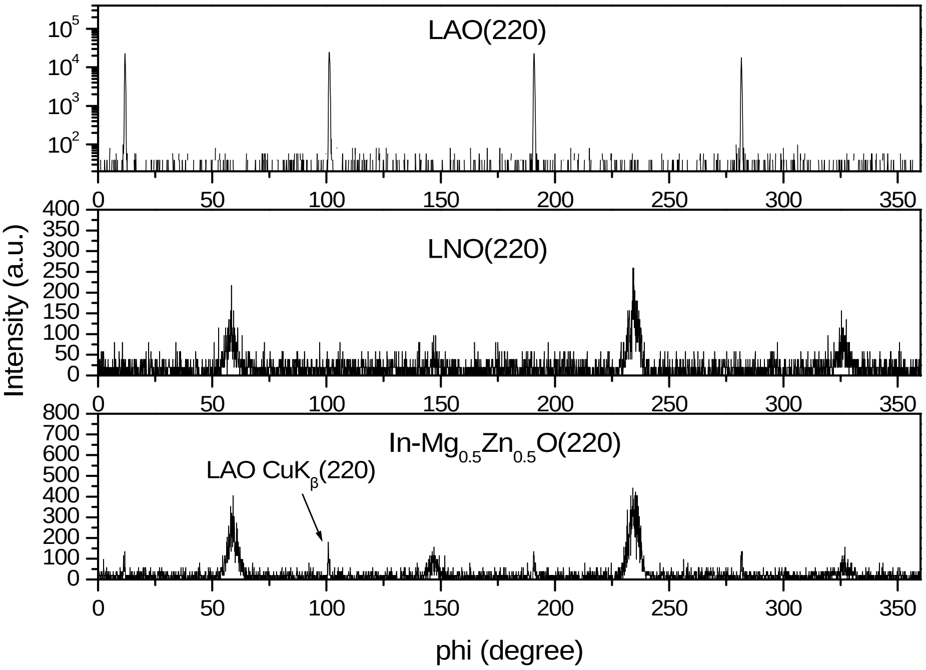

Figure 5.33 The XRD 360^0-ϕ scans on the $Li_{0.15}Ni_{0.85}O(220)$, In-$Mg_{0.5}Zn_{0.5}O(220)$ and LAO(220) reflections of the p-$Li_{0.15}Ni_{0.85}O$/n-In-$Mg_{0.5}Zn_{0.5}O$/Pt pn-heterojunction grown on LAO(100) substrate.

The epitaxial relationship between the films and substrate are shown in Figure 5.33. The three patterns are the XRD 360^0-ϕ scans of the $Li_{0.15}Ni_{0.85}O(220)$ plane, the In-$Mg_{0.5}Zn_{0.5}O(220)$ plane and the LAO(220) plane. The four-fold symmetry confirms the cubic structure of the films and substrate. It is noticed that there is a 45° rotation between the basal planes of In-MZO and LAO diffraction peaks. This result agrees with that of oriented film growth presented in previous section 4.2.1. In-MZO and LNO diffraction peaks appear at the same ϕ angles, indicating that LNO film is cube-on-cube epitaxially grown on In-MZO film. The epitaxial relationships between the deposited films and the LAO substrate is (100)LNO||(100)In-MZO||(100)LAO (out-of-plane) and (011)LNO||(011)In-MZO ||(010)LAO (in-plane).

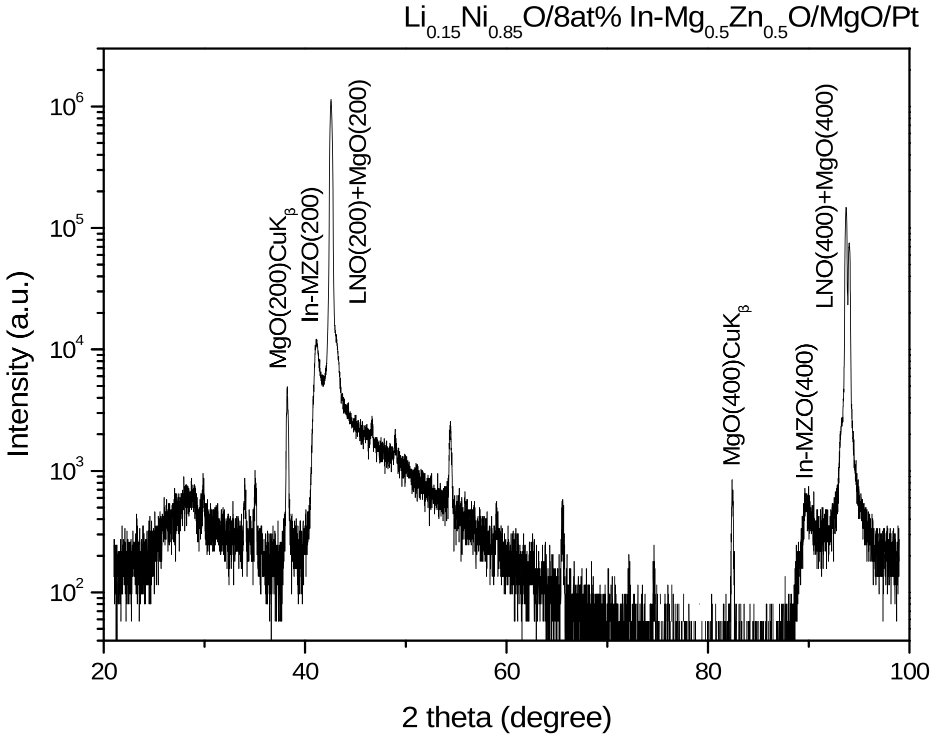

Figure 5.34 XRD 2 theta scan of p-$Li_{0.15}Ni_{0.85}O$/n-In-$Mg_{0.5}Zn_{0.5}O$/Pt pn-heterojunction grown on MgO(100) substrate.

Apart from the p-$Li_{0.15}Ni_{0.85}O$/n-In-$Mg_{0.5}Zn_{0.5}O$/Pt junction deposited on LAO substrate, we have also analyzed same material for the junction deposited on the MgO substrate. The XRD 2-theta profile shows a similar pattern as that of junction grown on LAO substrate. Cubic In-MZO(h00) and LNO(h00) and MgO(h00) families of peaks are found in Figure 5.34, indicating single phase bi-layer with good film orientation on

MgO. In-MZO(200) and (400) diffraction peaks are found at the angles of 41.17° and 90.00°. LNO(h00) plane diffractions overlap with the MgO substrate (h00) peaks due to similar lattice constants between LNO (4.16Å) and MgO (4.24Å).

We note that the rocking curves of the In-MZO (200) and (400) planes have the FWHM of 0.9302° and 0.3296°. The figure is not shown here. The LNO(200) and (400) plane diffractions are overwhelmed by the MgO peaks, hence the rocking curves actually denote the FWHM values of MgO(200) and (400) only.

The 360° ϕ-scans of this p-n junction are shown on Figure 5.35. Four-fold symmetry and same ϕ angles of the diffraction peaks confirm the bi-layer films are cube-on-cube epitaxially grown on MgO substrate. The epitaxial relationships between the deposited films and the substrate is concluded to be (100)LNO||(100)In-MZO||(100)MgO (out-of-plane) and (011)LNO||(011)In-MZO ||(011)MgO (in-plane).

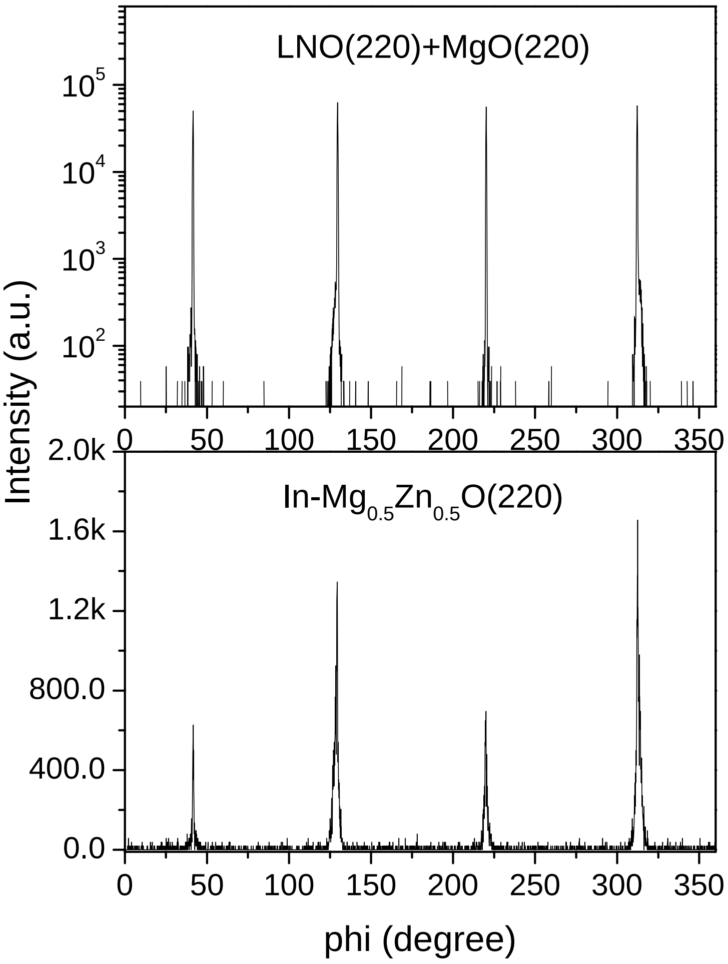

Figure 5.35 The XRD 360^0-ϕ scans on the $Li_{0.15}Ni_{0.85}O$(220), In-$Mg_{0.5}Zn_{0.5}O$(220) and MgO(220) reflections of the p-$Li_{0.15}Ni_{0.85}O$/n-In-$Mg_{0.5}Zn_{0.5}O$/Pt pn-heterojunction grown on MgO(100) substrate.

5.3.3.3 I-V characterization

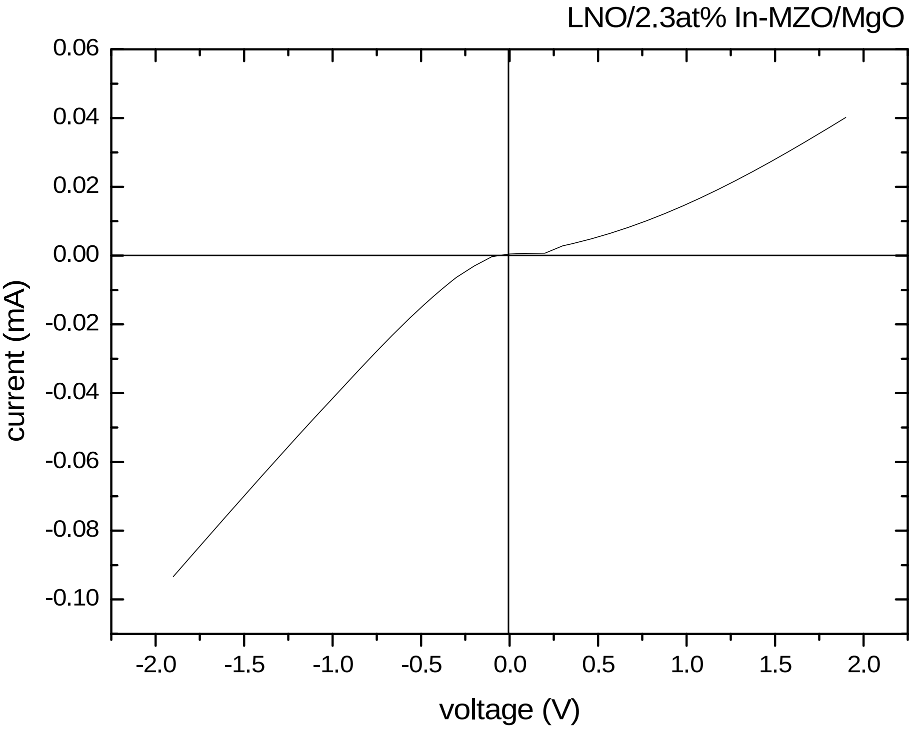

Figure 5.36 I-V characteristics of the p-$Li_{0.15}Ni_{0.85}O$/n-2.3at.% In-$Mg_{0.5}Zn_{0.5}O$ heterojunction diode at room temperature.

Figure 5.36 presents the I-V characteristics of LNO/2.3at.% In doped $Mg_{0.5}Zn_{0.5}O$ junction on MgO (100) substrate. A rather unsatisfactory diode rectifying profile is obtained. The turn-on voltage of the junction is about 0.3V in the forward biased region. A large leakage current under reverse bias is also presented.

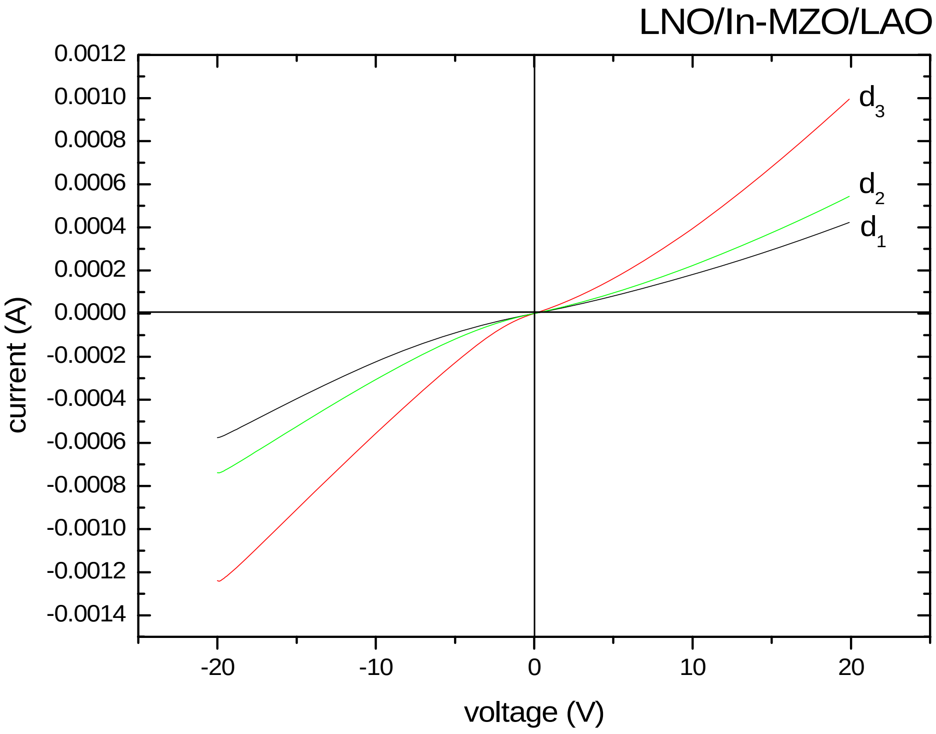

Figure 5.37 I-V characteristics of the p-$Li_{0.15}Ni_{0.85}O$/n-8at.% In-$Mg_{0.5}Zn_{0.5}O$ heterojunction diode at room temperature.

The I-V characteristics of the $Li_{0.15}Ni_{0.85}O$/8at.% In doped $Mg_{0.5}Zn_{0.5}O$ diode deposited on LAO substrate is shown in Figure 5.37 with different measuring circuit distance along the substrate. Asymmetry profiles are observed but they are not so good as the LNO/2.3at.% In doped $Mg_{0.5}Zn_{0.5}O$ junction grown on MgO(100) substrate and other p- $Li_{0.15}Ni_{0.85}O$ based heterojunction diodes. Further work should be focused on improving the I-V curves. In our experimental measurement the n-type layer is at the bottom. The Pt electrode lead can be placed close to the junction. Therefore the n-type layer resistance could give rise to circuit's series resistance and rectifying profile of the junction. Different amount of In_2O_3 doping to increase the carrier concentration in In-MZO films should be tried. In addition, STO insulator layer could also be deposited between p-layer and n-layer to amend the phenomenon of large leakage current.

In the profile shown in Figure 5.37, the measuring distance $d_1>d_2>d_3$. Therefore, different series resistances due to d introduce load lines, which influence the slope of the I-V profiles. Indeed the slope of the I-V curve in the linear region decreases with increasing measuring distance d.

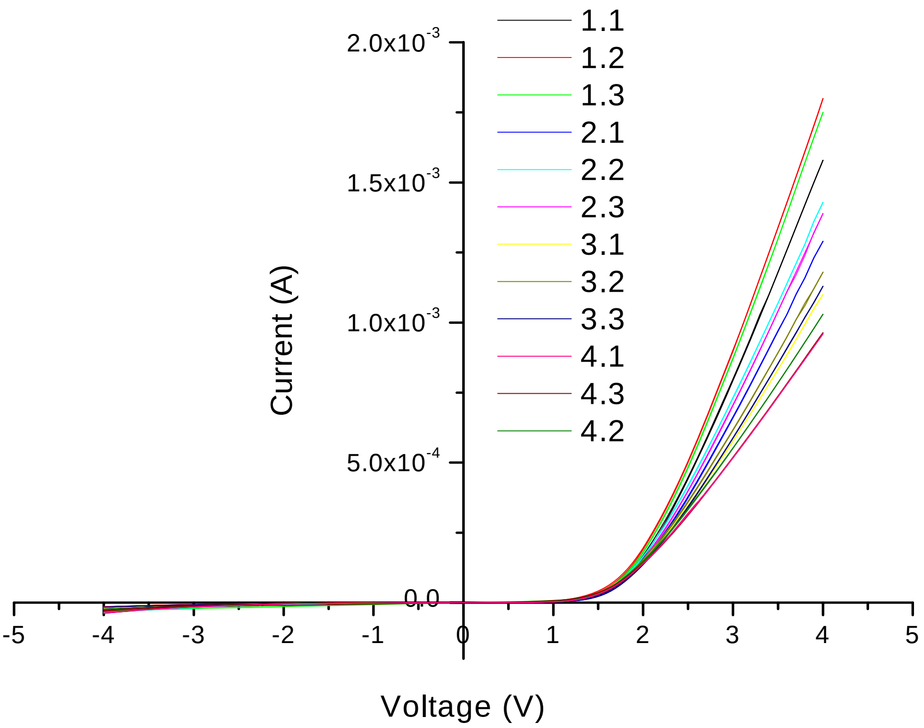

Figure 5.38 I-V characteristics of the p-$Li_{0.15}Ni_{0.85}O$/n-10at.% In-$Mg_{0.5}Zn_{0.5}O$ heterojunction diode at room temperature with different measuring spots.

Finally, we add more amount of In_2O_3 up to 10at.%. Rather good I-V profiles are demonstrated in the p-$Li_{0.15}Ni_{0.85}O$/n-10at.% In-$Mg_{0.5}Zn_{0.5}O$ heterojunction diode at room temperature, which are shown in Figure 5.38. Small leakage current and large forward-based current are obtained. Different spots on the junction are measured. The I-V characteristics under different temperatures are also explored. The profiles are good up to 380K, which are shown in Figure 5.39. This proves that this diode could be operated under high temperature.

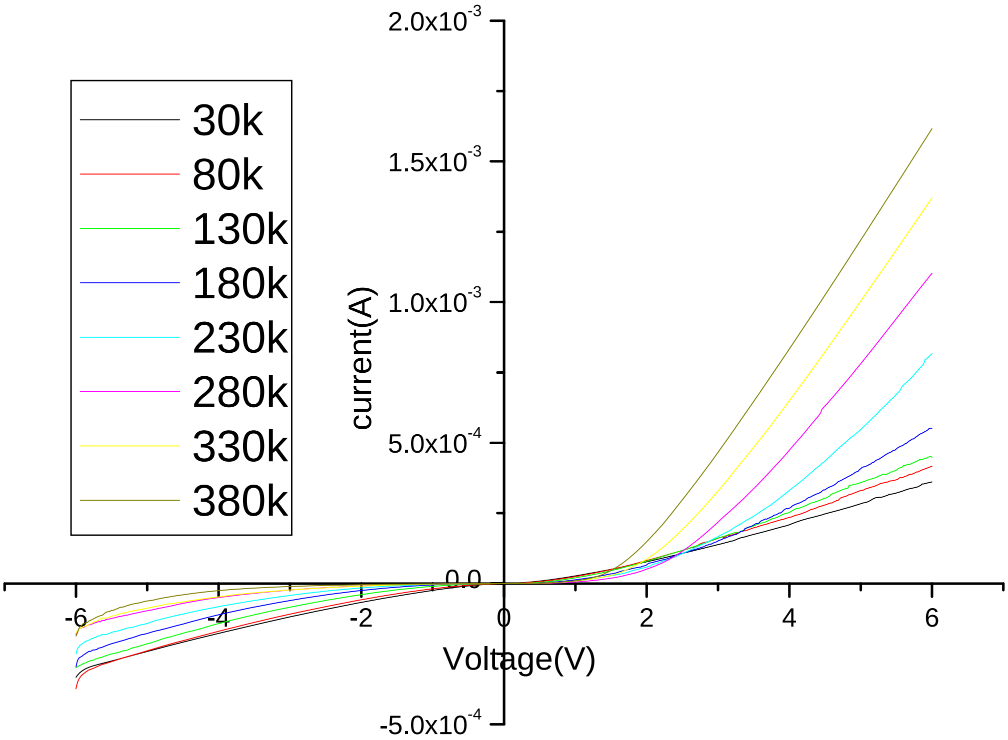

Figure 5.39 I-V characteristics of the p-$Li_{0.15}Ni_{0.85}O$/n-10at.% In-$Mg_{0.5}Zn_{0.5}O$ heterojunction diode under different temperatures.

CHAPTER 6

CONCLUSION AND FURTHER WORK

6.1 Conclusion

$Mg_xZn_{1-x}O$ mixed oxide ceramic targets with x from 0% to 100% were fabricated by standard solid-state reaction from high purity powders of constituent oxides. They were used in our Pulsed Laser Deposition (PLD) experiments to produce all-oxide p-n junctions. The air-sintered $Mg_{0.9}Zn_{0.1}O$, $Mg_{0.7}Zn_{0.3}O$ and $Mg_{0.5}Zn_{0.5}O$ targets are single-phase compounds, which possess similar XRD patterns with major diffraction peaks well matched with those listed in the ICDD database. Lattice constants of the targets are calculated to be 0.4213nm, 0.4227nm, 0.4231nm for $Mg_{0.9}Zn_{0.1}O$ target, $Mg_{0.7}Zn_{0.3}O$ target and $Mg_{0.5}Zn_{0.5}O$ target, respectively. The lattice constant increases with ZnO composition, in general agreement with the Vegard's law. $Mg_{0.2}Zn_{0.8}O$ target exhibits similar pattern as that of ZnO target indicating also a single phase structure. The $Mg_{0.4}Zn_{0.6}O$ target is however a mixed-phase compound. Apart from reflections that could be indexed according to the hexagonal ZnO phase, some reflections from the cubic MgO phase are also present. EDX tests on the composition of $Mg_xZn_{1-x}O$ targets exhibit a ±10% maximum deviation from the nominal values.

All the $Mg_xZn_{1-x}O$ thin films were deposited successfully by PLD technique on LAO(100), MgO(100), MgO(111) and Al_2O_3(0001) substrates using the as-fabricated targets. The advantages of PLD method over other deposition techniques such as molecular beam epitaxy and metallorganic vapor phase epitaxy include simplicity, unique capability of transferring any source materials to the surface of a substrate and its pulsed nature, which affords high controllability of the deposition film thickness. All these beneficial features of PLD were fully utilized in our current work to fabricate complex oxide thin films and heterostructures. Processing parameters such as the substrate temperature, the ambient oxygen pressure, the target-substrate distance and the laser fluence were optimized in the film deposition process in order to obtain good crystallinity and surface morphology of the PLD-produced films. Excellent single crystal quality epitaxy grown $Mg_xZn_{1-x}O$ films with x ranging from 0 to 1 were obtained.

Epitaxial cubic $Mg_xZn_{1-x}O$ films ($0.95 > x > 0.6$) grown on single crystal LAO(100) substrates have been realized by PLD. XRD and AFM studies indicate that the as-grown MZO films have excellent structural and surface properties. The cross-section morphology reveals layer thickness of about 250nm. Cube-on-cube growth with heteroepitaxial relationship of $(100)_{c\text{-}MgxZn1\text{-}xO}||(100)_{LAO}$ (out-of-plane) and $(011)_{c\text{-}MgxZn1\text{-}xO}||(010)_{LAO}$ (in-plane) have been obtained. The lattice parameters a of $Mg_xZn_{1-x}O$ films increase almost linearly with increasing ZnO composition. All c-MZO films show excellent optical transmittance with band edge situated well in the UV. High resolution TEM micrograph of the c-MZO and LAO interface confirms that domain matching is in the form of 2 diagonal units of c-MZO to 3 units of LAO is indeed the case. We have successfully demonstrated the trapping c-MZO with high Zn content with lattice matched cubic substrates. High quality epitaxial c-MZO(100) films can be achieved and they are potentially useful for developing various UV photonic and spintronic devices.

$Mg_xZn_{1-x}O$ (0.95 > x > 0.6) films were also deposited on cubic MgO(100) substrates to form cubic MZO with high Zn content. Since MgO(100) substrate could provide a better matched lattice constant for $Mg_xZn_{1-x}O$ alloy thin films than that from LAO(100) substrate, excellent epitaxial crystal MZO films grown on MgO(100) were achieved. Bright-field TEM micrographs of the cross section of the $Mg_{0.6}Zn_{0.4}O$/MgO sample and the selective area electron diffraction (SAED) pattern confirmed the perfectly matched epitaxial relationship (100)c-MZO//(100)MgO, [010]c-MZO//[010]MgO. Crystal grains were alloy-like grown with same texture of MgO substrate. The results also revealed that LAO and MgO substrates could equally well assist growth of c-$Mg_xZn_{1-x}O$ films.

For films grown on MgO(111) substrates, cubic $Mg_xZn_{1-x}O$ (0.6 > x > 0.2) (111) and (222) diffraction planes were indexed. However, for the ZnO/MgO(111) film, preferred ZnO(0002) and (0004) orientations were observed because the surface energy of (0002) planes is the lowest in the ZnO crystal. Grains with the lower surface energy tend to become larger as the films grow. Three-fold symmetry diffraction peaks of substrate and six-fold symmetry diffraction profiles of ZnO film indicated that the ZnO layer was heteroepitaxially grown on the MgO(111) substrate with epitaxial relationships of (0001)ZnO||(111)MgO (out-of-plane) and (1002)ZnO||(002)MgO (in-plane).

$Mg_xZn_{1-x}O$ alloy thin films have also been successfully grown on Al_2O_3(0001) substrates by PLD. $Mg_{0.2}Zn_{0.8}O/Al_2O_3$(0001) film possesses same single phase hexagonal structure as that of the ZnO/Al_2O_3(0001) film, which grows with preferred c-axis orientation. In this work, an epitaxial relationship of (0001)MZO||(0001)Al_2O_3 (out-of-plane) and (1002)MZO||(1002)Al_2O_3(in-plane) was obtained. However, for the $Mg_{0.4}Zn_{0.6}O/Al_2O_3$ film, reflections from cubic $Mg_{0.4}Zn_{0.6}O$(111) and $Mg_{0.4}Zn_{0.6}O$(222) diffraction planes were detected. This is due to the fact that $Mg_{0.4}Zn_{0.6}O$ target is mixed phase and cubic MgO dominates the structure formation in $Mg_{0.4}Zn_{0.6}O$ film.

Indium doped $Mg_{0.5}Zn_{0.5}O$ targets were prepared. Films produced by using these targets show enhanced semiconductivity while keeping the original cubic structure. Cube-on-cube epitaxial growth of In-MZO film on MgO substrate was obtained. The epitaxial In-MZO semiconducting films were then used as the n-type oxides in fabricating p-n junctions in our project.

All-oxide heterostructures of p-$Li_{0.15}Ni_{0.85}O$/n-Nb-STO, p-$Li_{0.15}Ni_{0.85}O$/n-ZnO and p-$Li_{0.15}Ni_{0.85}O$/n-In-$Mg_{0.5}Zn_{0.5}O$ have been fabricated by PLD. They all exhibit highly asymmetric electrical rectification, suggesting promising material possibilities for low-cost and optically transparent diode devices for a wide range of applications.

15at.% Li-doping NiO film is a p-type transparent conducting oxide material with resistivity of about 1.4Ω-cm and band gap of 3.7eV. The $Li_{0.15}Ni_{0.85}O$ film was deposited on single crystal conducting n-type NSTO substrate to fabricate an all oxide p-n junction. Cube-on-cube epitaxial growth is realized. A typical diode rectifying profile is obtained with a turn-on voltage of about 0.8V. Unfortunately under the reverse bias the junction exhibits a large leakage current which primarily comes from large tunneling current of a narrow depletion layer. An efficient way to suppress the leakage current is to insert a thin STO insulating layer between these two diode layers. It has been shown that the large leakage current is substantially reduced. Unfortunately the forward bias current is also reduced and the turn-on voltage is raised to 1.1V.

We have fabricated transparent all-oxide p-n junctions based on the p-type LNO and n-type ZnO films grown on sapphire and MgO(111) substrates with Pt contacts. The similar oxygen atomic configurations (six-fold symmetry) of (0002)ZnO and (111) LNO ensures a high-quality LNO epitaxial layer grown on the single-crystalline ZnO film in spite of the different crystal structures of wurtzite ZnO and rock salt LNO. The heteroepitaxial relationships are (111)LNO||(0001)ZnO||(0001)Al_2O_3 (out-of-plane), (002)LNO||(1002)ZnO||(1002)Al_2O_3 (in-plane), (111)LNO||(0001)ZnO||(111)MgO (out-of-plane) and (002)LNO||(1002)ZnO||(002)MgO (in-plane). Junction morphology was investigated by SEM. The diode surface is observed to be smooth, featureless and crack-free. No obvious particulates appear by using the shadow mask technique during the deposition process. The cross-section morphology reveals sharp junction boundary and layer thickness of about 200-300nm. Optical transmittance of the bi-layer p-$Li_{0.15}Ni_{0.85}O$/n-ZnO is over 80% in the visible region. The heterojunction exhibits a good electrical rectifying profile under room temperature. It has a small leakage current and a large forward-based current, and the turn-on voltage is about 1.0V.

Another all-transparent-oxide p-n junction based on the p-type LiNiO and n-type In-$Mg_{0.5}Zn_{0.5}O$ films on LAO and MgO(100) substrates has also been fabricated. The bi-layers show excellent epitaxial relationship of (100)LNO||(100)In-MZO||(100)LAO (out-of-plane), (011)LNO||(011)In-MZO ||(010)LAO (in-plane), (100)LNO||(100)In-MZO||(100)MgO (out-of-plane) and (011)LNO||(011)In-MZO||(011)MgO (in-plane). A 45° rotation between the four basal planes of In-MZO and LAO shows up in the diffraction peaks in the XRD 360^0-ϕ scans. This result agrees with that presented in undoped MZO films grown on LAO. For the junction of LNO/2.3at.% In-$Mg_{0.5}Zn_{0.5}O$, a rectifying characteristic is obtained. However the leakage current is large and the turn-on voltage is about 0.3V. For the junction of LNO/8at.% In-$Mg_{0.5}Zn_{0.5}O$, the I-V characteristics are poor although an asymmetry profile is observed.

6.2 Suggestions for future work

Realization of metastable rocksalt cubic ZnO (c-ZnO) phase under normal ambient condition is crucial and could open up a broad range of technological applications as heterojunctions for photodetection, photovoltaic devices and efficient blue/UV laser diode. We have demonstrated that cubic $Mg_xZn_{1-x}O$ films with x>0.57 can be stabilized and epitaxially grown on cubic substrates. Future attempts will be directed towards continuous increase of the Zn content further on one hand, and achieving a direct verification on the existence of c-ZnO on the other. Since there are very little reports on the studies of c-ZnO, the later objective will be rather difficult. A precision absorption spectroscopy and photoluminescence spectroscopy are needed to accurately determine the bandgap energy and the direct/indirect nature of the bandgap. Micro-Raman spectroscopy may also be useful to study the energy band structures of c-ZnO. A direct comparison of c-ZnO and wurtzite ZnO will be very informative and insightful.

In order to enhance their potential for device application, $Mg_xZn_{1-x}O$ films can be deposited on TiN buffered Si(100) substrates. TiN has a cubic structure with a=4.2Å. It can be grown epitaxially on Si via domain matching. At about 650°C, TiN is normally not oxidized under 10^{-5} torr of partial pressure of oxygen. Fabrication of $Mg_xZn_{1-x}O$/TiN/Si(100) heterostructure could help to form integrated tunable UV and blue photodetectors.

Electrical and optical properties of $Mg_xZn_{1-x}O$ films and In doped $Mg_xZn_{1-x}O$ films should be studied further because changing the resistance of n-type In-$Mg_xZn_{1-x}O$ films could obviously affect the rectifying performance of the junctions. Different amount of In_2O_3 doping to change the carrier concentration and conductivity in In-MZO films should be attempted. Then different arrangements of p-LNO/n-x.% In-MZO junctions with the aim of matching p- and n-type conductivity, and of improving the I-V rectifying performance should be studied further. For example, STO insulator layers should be deposited between p-layer and n-layer to amend the phenomenon of large leakage current.

The successful fabrication of all-oxide p-n junction is the first step to utilize conducting and semiconducting oxides in the electronic world. The potential for high temperature operation of these all-oxide junctions is definitely advantageous. In these aspect, p-type and n-type conducting oxides are needed. We have fabricated a few p-n oxide hetero-junctions based on n-type In-MZO and other p-type oxides. For homo-junction, we need to develop p-type MZO. It has been shown that p-type doping of wurtzite MZO is very difficult. The use of cubic MZO perhaps can offer an easy route for efficient p-type MZO doping. This indeed will be an interesting and useful topic for future work.

P-type $La_{0.7}Sr_{0.3}MnO_3$(LSMO) film could be combined with n-type In-MZO film to fabricate magnetoresistive oxide hetero-p-n junctions since LSMO is a well known giant magnetoresistive material. Its T_c at above room temperature is particularly useful for device applications. Ferromagnetic properties with a high curie temperature was predicted in the diluted magnetic semiconductors(DMS) based on doping ZnO with 3d transition metals(TM) such as NiO, CoO or MnO. By putting the ferromagnetic $TM_xZn_{1-x}O$ films together with the LSMO films, the proposed heterostructure would be a useful spintronic junction. Apart from LSMO, other p-type cubic DMS oxides, such as Mn doped Cu_2O, can also be considered. We believe that the present research could serve as a good foundation for many future R&D on oxide spintronic junctions.

REFERENCES

[1-1] Research project proposal: Fabrication and characterization of all oxide p-n junction diodes.

[1-2] V. E. Henrich and P. A. Cox, The surface science of metal oxides (Cambridge University Press, Cambridge CB2 1RP, 1994).

[1-3] A. F. Wells, Structural Inorganic Chemistry, 5th edn (Oxford University Press, Oxford, 1984).

[1-4] Peter Y. Yu and Manuel Cardona, Fundamentals of Semiconductors: Physics and Materials Properties, second Updated Edition (Springer-Verlag Berlin Heidelberg New York, 1999).

[1-5] Lev I. Berger, Semiconductor materials (CRC Press, Boca Raton, Florida, 1997).

[1-6] Shyh Wang, Fundamentals of semiconductor theory and device physics (Prentice-Hall, New Jersey, 1989).

[1-7] E. Fred Schubert, Doping in Ⅲ-Ⅴ semiconductors (Cambridge University Press, Cambridge CB2 1RP, 1993).

[1-8] Aicha Elshabini-Riad & Fred D. Barlow Ⅲ, Thin Film Technology Handbook (McGraw-Hill, New York, 1997).

[1-9] J. E. Greene, Multicomponent and multilayered thin films for advanced microtechnologies (O. Auciello and J. Engemann, eds.), NATO/ASI Series E 234, Kluwer Academic Publishers, The Netherlands (1993)39.

[1-10] G. A. Forman, J. A. Nieznanski and J. Rose, “Die for MCMs: IC Preparation for Testing, Analysis, and Assembly,” Proceedings of the IEEE Multichip Module Conf, pp. 32-35, March 1992.

[1-11] T. E. Figal, “Below A Minute Burn-In,” U. S. Patent 5,030,905, July 9, 1991.

[1-12] D.C.Look, Materials Science and Engineering B, Vol. **80**, 383 (2001).

[1-13] H.Ohta, K.Kawamura, M.Orita, N.Sarukura, M.Hirano, H.Hosono, Materials Research Society Symposia Proceedings **623**, 283 (2000).

[1-14] A.Tsukazaki, A.Ohtomo, T.Onuma, M.Ohtani, T.Makino, M.Sumiya, K.Ohtani, S.F.Chichibu, S.Fuke, Y.Segawa, H.Ohno, H.Koinuma and M.Kawasaki, Nature Materials **4**, 42 (2005).

[1-15] J. B. Webb, D. F. Williams, R. Adsett, Journal of the canadian ceramic society **52**, 33-36 (1983).

[1-16] J.Narayan, K.Dovidenko, A.K.Sharma, S.Oktyabrasky, J.Appl.Phys. **84**, 2597 (1998).

[1-17] A.Ohtomo, M.Kawasaki, Y.Sakurai, I.Ohkubo, R.Shiroki, Y.Yoshida, T.Yasuda, Y.Segawa, H.Koinuma, Mater. Sci. Eng. B. **56**, 263 (1998).

[1-18] Ya. I. Alivov, E.V.Kalinina, A.E.Cherenkov, D.C.Look, B.M.Ataev, A.K.Omaev, M.V.Chukichev and D.M.Bagnall, Appl. Phys. Lett. 83, 4719 (2003); Material Research Society, Symposium Proceedings **798**, 41 (2003).

[1-19] Nuri W.Emanetoglu, Jun Zhu, Ying Chen, Jian Zhong, Yimin Chen and Yicheng Lu, Appl. Phys. Lett. **85**, 3702 (2004).

[1-20] W.Yang, S.S.Hullavarad, B.Nagaraj, I.Takeuchi, R.P.Sharma, T.Venkatesan, R.D.Vispute and H.Shen, Appl. Phys. Lett. **82**, 3424 (2003).

[1-21] W.Yang, R.D.Vispute, S.Choopun, R.P.Sharma, T.Venkatesan and H. Shen, Appl. Phys. Lett. **78**, 2787 (2001).

[1-22] S.J.Pearton, W.H.Heo, M.Ivill, D.P.Norton and T.Steiner, Semicond. Sci. Technol. **19**, R59 (2004).

[1-23] Darshan C.Kundaliya, S.B.Ogale, S.E.Lofland, S.Dhar, C.J.Metting, S.R.Shinde, Z.Ma, B.Varughese, K.V.Ramanjuchary, L.Salamanca-Rida and T.Venkatesan, Nature Materials **3**, 709 (2004).

[1-24] Lee Eun-Cheol and K.J.Chang, Physical Review B **69**, 85205 (2004).

[1-25] Min Sik Park and B.I.Min, Physical Review B **68**, 224436 (2003).

[1-26] P.Sharma, A.Mansingh and K.Sreenivas, Appl. Phys. Lett. **80**, 553 (2002).

[1-27] Agisilaos A. Iliadis, Soumya Krishnamoorthy, Wei Yang, Supab Choopun, R.D.Vispute and T.Venkatesan, Proc. SPIE Int. Soc. Opt. Eng. **4650**, 67 (2002).

[1-28] Elvira M.C.Fortunato, Pedro M.C.Barquinha, Ana C.M.B.G.Pimentel, Alexandra M.F.Goncalves, Antonio J.S.Marques, Rodrigo F.P.Martins and Luis M.N.Pereira, Appl. Phys. Lett. **85**, 2541 (2004).

[1-29] J.Newey, Compound Semiconductor **8**, 2 (2002).

[1-30] T.Minami, MRS Bulletin **25**, 38 (2000).

[1-31] Toshihiro Miyata, Tadatsugu Minami, Hirotoshi Sato and Shinzo Takata Jpn. J. Appl. Phys. **31**, 932 (1992).

[1-32] A.Ohtomo, M.Kawasaki, T.Koida, K.Masubuchi, H.Koinuma, Y.Sakurai, Y.Yoshida, T.Yasuda, Y.Segawa, Appl. Phys. Lett. **72**, 2466 (1998).

[1-33] A.K.Sharma, J.Narayan, J.F.Muth, C.W.Teng, C.Jin, A.Kvit, R.M.Kolbas, and O.W.Holland, Appl. Phys. Lett. **75**, 3327 (1999).

[1-34] I. Takeuchi, W.Yang, K.-S.Chang, M.A.Aronova, T.Venkatesan, R.D.Vispute, and L.A.Bendersky, J.Appl. Phys. **94**, 7336 (2003).

[1-35] Toshihiro Miyata, Shingo Suzuki, Makoto Ishii, Tadatsugu Minami, Thin Solid Films **411**, 76 (2002).

[1-36] T.Makino, Y.Segawa, M.Kawasaki, A.Ohtomo, R.Shiroki, K.Tamura, T.Yasuda, and H. Koinuma, Appl. Phys. Lett. **78**, 1237 (2001).

[1-37] M.Levinshtein, S.Rumyantsev, M.Shur, Handbook series on semiconductor parameters, Singapore; New Jersey: World Scientific, Vol. 1 (1996).

[1-38] J.Narayan, A.K.Sharma, A.Kvit, C.Jin, J.F.Muth and O.W.Holland, Solid State Comm. **121**, 9 (2002).

[1-39] E.M.Levin, C.R.Robbins and H.F.McMurdie, Phase Diagrams for Ceramists, The American Ceramic Society, Columbus, Ohio (1964).

[1-40] Park W.I, Yi Gyu-Chul and Jang H M 2001 Appl. Phys. Lett. **79**, 2022 (2001).

[1-41] C.W.Teng, J.F.Muth, U. Ozgur, M.J.Bergmann, H.O.Everitt, A.K.Sharma, C.Jin and J. Narayan, Appl. Phys. Lett. **76**, 979 (2000).

[1-42] S.Choopun, R.D.Vispute, W.Yang, R.P.Sharma and T.Venkatesan, Appl. Phys. Lett. **80**, 1529 (2002).

[1-43] A. Namiki, T. Kawai, K. Ichige, Surf. Sci. **166**, 129 (1986).

[1-44] R.K. Singh, SPIE 2045, 10.

[1-45] M. Hanabusa, Mater. Res. Soc. Symp. Proc. **285**, 447 (1993).

[1-46] T. J. Goodwin, V. J. Leppert, S. H. Risbud, I. M. Kennedy, and H. W. H. Lee, Appl. Phys. Lett. **70**, 3122 (1997).

[1-47] S. Metev, K. Meteva, Appl. Surf. Sci. **43**, 402 (1989).

[1-48] T. H. Maiman, Nature **187**, 493 (1960).

[1-49] J. F. Ready, Appl. Phys. Lett. **3**, 11 (1963).

[1-50] G. A. Askar'yan, A. M. Pokhorov, G. F.Chantutiya and G. P. Shipulo, Sov. Phys. JETP **17**, 6 (1963).

[1-51] R. G. Meyerand and A. F. Haughty, Phys. Rev. Lett. **9**, 403 (1963).

[1-52] H. M. Smith and A. F. Turner, Appl. Opt. **4**, 147(1965).

[1-53] D. Dijkkamp, T. Venkatesan, X. D. Wu, S. A. Shaheen, N. Jisrawi, Y. H. Min-Lee, W. L. Mclean and M. Croft, Appl. Phys. Lett. **51**, 619 (1987).

[1-54] D. K. Fork, K. Nashmoto and T. H. Geballe, Appl. Phys. Lett. **60**, 1621 (1992).

[1-55] R. Ramesh, Thin film ferroelectric materials and devices, Kluwer academic publishers, Boston (1997).

[1-56] G. M. Norton, P. G. Kotula and C. B. Carter, J. Appl. Phys. **70**, 2871 (1991).

[1-57] J. Narayan, P. Tiwari, X. Chen, J. Singh, R. Chowdhury and T. Zheleva, Appl. Phys. Lett. **61**, 1290 (1992).

[1-58] R. F. Curl and R. E. Smalley, Sci. Am. October, 54 (1991).

[1-59] J. T. Cheung, I. Gergis, M. James and R. E. DeWames, Appl. Phys. Lett. **60**, 3180 (1992).

[1-60] J. A. Greer and H. J. Van Hook, Mater. Res. Soc. Symp. Proc. **191**, 171 (1990).

[1-61] D. M. Mattox, Film deposition using accelerated Ins, Rec. SC-DR-281-63, Sandia Corp (1963).

[1-62] L. Lynds, B. R. Weinberger, D. M. Potrepka, G. G. Pterson and M. P. Lindsay, Physica. C **159**, 61 (1989).

[1-63] C. Girault, D. Damiani, J. Aubreton and A. Catherinot, Appl. Phys. Lett. **55**, 182 (1989).

[2-1] V. Ruckenbauer, F. F. Hau, S. G. Lu, K. M. Yeung, C. L. Mak and K. H. Wong, Appl. Phys. A. **78**, 1049 (2004).

[2-2] W. L. Sin, Structural and electrical properties of MnO films grown by pulsed laser deposition, MPhil thesis, 2004.

[2-3] W. M. Yu, Heteroepitaxial growth of high k dielectric thin films by pulsed laser deposition, MPhil thesis, 2004.

[2-4] L. Zhuang, Fabrication and characterization of all oxide p-n junction, Report for confirmation of Ph.D registration, 2004.

[2-5] L. Reimer, Scanning electron microscopy : physics of image formation and microanalysis, second edition, Berlin : Springer, 1998.

[2-6] J. A. Gadsden**,** Infrared spectra of minerals and related inorganic compounds, London : Butterworths, 1975.

[2-7] Thomas A. Carlson, X-ray photoelectron spectroscopy, Dowden, Hutchinson & Ross, 1978.

[2-8] C. Y. Lam, Semiconducting properties of oxide thin films prepared by pulsed laser deposition, MPhil thesis, 2005.

[4-1] W.L.Park, G.-C. Yi, H.M.Jang, Appl. Phys. Lett. **79**, 2022 (2001).

[4-2] Y.Jin, B.Zhang, S.Yang, Solid State Commun. **119**, 409 (2001).

[4-3] J.H.Kang, Y.R.Park, K.J.Kim, Solid State Commun. **115**, 127 (2000).

[4-4] T. Tanigaki, S. Kimura, N. Tamura, C. Kaito, Jpn. J. Appl. Phys. **41**, 5529 (2002).

[4-5] A. Ohtomo, M. Kawasaki, Y. Sakurai, I. Ohkubo, R. Shiroki, Y. Yoshida, T. Yasuda, Y. Segawa, H. Koinuma, Mater. Sci. Eng. B **56**, 263 (1998).

[4-6] A. Ohtomo, M. Kawasaki, T. Koida, K. Masubuchi, H. Koinuma, Y. Sakurai, Y. Yoshida, T. Yasuda, Y. Segawa, Appl. Phys. Lett. **72**, 2466 (1998).

[4-7] K.Matsubara, H.Tampo, H.Shibata, A.Yamada, P.Fons, K.Iwata and S.Niki, Appl. Phys. Lett. **85**, 1374 (2004).

[4-8] F.K.Shan, B.C.Shin, S.W.Jang and Y.S. Yu, Journal of the European Ceramic Society, **24**, 1015 (2004).

[5-1] K.L.Chopra, S.Major and D.K.Pandya, Thin Solid Films, **102**, 1 (1983).

[5-2] H. Ohta, M. Kamiya, T. Kamiya, M. Hirano and H. Hosono, Thin Solid Films **445**, 317 (2003).

[5-3] R.J.Powell, W.E.Spicer, Phys. Rev. B **2**, 2182 (1970).

[5-4] G. A. Sawatzky, J.W.Allen, Phys. Rev. Lett. **53**, 2339 (1984).

[5-5] A. Fujimori, F. Minami, Phys. Rev. B **30**, 957 (1984).

[5-6] J.Narayan, K.Dovidenko, A.K.Sharma, S.Oktyabrasky, J.Appl.Phys. **84**, 2597 (1998).

[5-7] A.Ohtomo, M.Kawasaki, Y.Sakurai, I.Ohkubo, R.Shiroki, Y.Yoshida, T.Yasuda, Y.Segawa, H.Koinuma, Mater. Sci. Eng. B. **56**, 263 (1998).

[5-8] A. Beiser, Concepts of modern physics, fifth edition, McGraw-Hill, 1995.

[5-9] Y. Watanabe, Appl. Phys. Lett. **66**, 1770 (1995).

[5-10] S. Mathews, R. Ramesh, T. Venkatesan and J. Benedetto, Science **276**, 238 (1997).

[5-11] K. S. So, K. H. Wong and W. B. Wu, Materials Research Society Symposium Proceedings 623 (2000).

[5-12] Atsushi Kudo, Hiroshi Yanagi, Kazushige Ueda, Hideo Hosono, Hiroshi Kawazoe and Yoshihiko Yano, Appl. Phys. Lett. **75**, 2851 (1999).

[5-13] Hiromichi Ohta, Ken-ichi Kawamura, Masahiro Orita, Masahiro Hirano, Nobuhiko Sarukura and Hideo Hosono, Appl. Phys. Lett. **77**, 475 (2000).

[5-14] Yukio Watanabe, Phys. Rev. B **59**, 11257 (1999).

[5-15] Masanori Sugiura, Kazuyuki Uragou, Minoru Tachiki and Takeshi Kabayashi, J. Appl. Phys. **90**, 187 (2001).

[5-16] Masanori Sugiura, Kazuyuki Uragou, Makoto Noda, Minoru Tachiki and Takeshi Kabayashi, Jpn. J. Appl. Phys. **38**, 2675 (1999).

[5-17] T. Nakasaka, K. Urago, M. Sugiura and T. Kobayashi, Jpn. J. Appl. Phys. **40**, L518 (2001).

[5-18] J. Zhang, H. Tanaka and T. Kawai, Appl. Phys. Lett. **80**, 4378 (2002).

[5-19] A. Tiwari, C. Jin, D. Kumar and J. Narayan, Appl. Phys. Lett. **83**, 1773 (2003).

[5-20] F. X. Hu, J. Gao, J. R. Sun and B. G. Shen, Appl. Phys. Lett. **83**, 1869 (2003).

[5-21] H. Tanaka, J. Zhang and T. Kawai, Phys. Rev. Lett. **88**, 027204 (2002).

[5-22] J. R. Sun, C. M. Xiong, B. G. Shen, P. Y. Wang and Y. X. Weng, Appl. Phys. Lett. **84**, 2611 (2004).

[5-23] J. R. Sun, C. M. Xiong, T. Y. Zhao, S. Y. Zhang, Y. F. Chen and B. G. Shen, Appl. Phys. Lett. **84**, 1528 (2004).

[5-24] K.Matsubara, H.Tampo, H.Shibata, A.Yamada, P.Fons, K.Iwata and S.Niki, Appl. Phys. Lett. **85**, 1374 (2004).

[5-25] J. Narayan, P. Tiwari, X. Chen, J. Singh, R. Chowdhury and T. Zheleva, Appl. Phys. Lett. **61**, 1290 (1992).

LIST OF PUBLICATIONS

1. <u>ZHUANG, L.</u> and WONG, K. H. Structure and surface studies of $Mg_xZn_{1-x}O$ films grown by pulsed laser deposition. Acta Metallurgica Sinica. Vol.18, no.3, pp.237-241 (2005)

2. <u>ZHUANG, L.</u> and WONG, K. H. Fabrication of transparent p-n junction composed of heteroepitaxially grown p-$Li_{0.15}Ni_{0.85}O$ and n-ZnO films for UV-detector applications. Applied Physics A. Accepted

3. <u>ZHUANG, L.</u>, WONG, K. H. and PANG, G. K. H. Realization of heteroepitaxial growth of wide bandgap cubic $Mg_xZn_{1-x}O$ alloy films on $LaAlO_3$ by pulsed laser deposition. Submitted to Scripta Materialia

4. <u>ZHUANG, L.</u> and WONG, K. H. Microstructure and optical properties of $Mg_xZn_{1-x}O$ thin films with different composition grown by means of pulsed laser deposition. Submitted to Thin Solid Films

5. LAU, C. H., <u>ZHUANG, L.</u> and WONG, K. H. In-doped transparent and conducting cubic magnesium zinc oxide thin films grown by pulsed laser deposition. Physica Status Solidi B. Accepted

6. <u>ZHUANG, L.</u> and WONG, K. H. Structure studies of $Mg_xZn_{1-x}O$ alloy films grown by pulsed laser deposition. Proceedings, Frontiers of Surface and Interface Science and Engineering 2004 conference (FSISE 2004), Guangzhou, pp. 33-34, 14-16 May 2004

7. ZHUANG, L. and WONG, K. H. Fabrication of transparent p-n junction composed of p-LNO and n-ZnO films. Proceedings, Conference on Lasers and Electro-Optics/Europe 2005 (CLEO/Europe 2005), Munich, pp. 136, 12-17 June 2005